Electromagnetic and Hard probes of Strongly Interacting Matter

By

Somnath De

Enrollment No. PHYS04200904005

Variable Energy Cyclotron Centre, Kolkata

A thesis submitted to

The Board of Studies in Physical Sciences

In partial fulfillment of requirements For the Degree of

DOCTOR OF PHILOSOPHY

of

HOMI BHABHA NATIONAL INSTITUTE

March, 2014

Homi Bhabha National Institute

Recommendations of the Viva Voce Board

As members of the Viva Voce Board, we certify that we have read the dissertation prepared by **Somnath De** entitled **Electromagnetic and Hard Probes of Strongly Interacting Matter** and recommend that it may be accepted as fulfilling the dissertation requirement for the Degree of Doctor of Philosophy.

....Date:

Chairman- Prof. R. K. Bhandari 28/3/2014

....Date: 28.3.2014

Guide / Convener- Prof. D. K. Srivastava D. K. Srivastava

....Date: 28/3/2014

Member 1- Prof. Jan-e Alam Jane Alam

....Date:

Member 2- Prof. M. G. Mustafa 28/03/2014

....Date:

Member 3 (External Examiner)- Prof. Basanta Nandi 28/03/2014

Final approval and acceptance of this dissertation is contingent upon the candidate's submission of the final copies of the dissertation to HBNI.

I hereby certify that I have read this dissertation prepared under my direction and recommend that it may be accepted as fulfilling the dissertation requirement.

D. K. Srivastava

Date: 28/3/2014.

Place: VECC, Kolkata

STATEMENT BY AUTHOR

Somnath De

Somnath De

DECLARATION

I, hereby declare that the investigation presented in the thesis has been carried out by me. The work is original and has not been submitted earlier as a whole or in part for a degree/diploma at this or any other Institution/University.

Somnath De

Somnath De

Dedicated

to

My Beloved Family Members

Acknowledgements

Pursuing a career in basic research was a passionate dream of mine since the college days. Thus I have joined the Variable Energy Cyclotron Centre as a doctoral student in 2008. After one year of rigorous course work, I started working under Dr. Dinesh Kumar Srivastava for the doctoral dissertation. The endeavour would not been possible without his continuous involvement and encouragement during these years. I have learned a lot from the discussions especially we used to have in the evening hours. His analysing capability and perfectionism in work always inspired me. I am indebted to him for his careful guidance through all these years.

A significant part of the thesis has been done in collaboration with Prof. Rainer J. Fries of Texas A & M University. I am grateful to him for providing the opportunity to visit Texas A & M and work in collaboration with him. I have greatly benefited from my stay at Texas and the correspondences with him after my return.

I wish to express sincere gratitude to all the teachers who had taught me during the course work and sincerely thank our Dean Academic (Physics) Dr. Jan-e Alam for a smooth processing of all academic matters.

I specially thank Dr. Rupa Chatterjee and Dr. Umme Jamil for their care and support in the earlier days of my Ph.D. career. I thank Dr. Santosh Das, Dr. Payal Mohanty, Dr. Victor Roy, and Dr. Sabyasachi Ghosh for all their help and motivations during the Ph.D. period. I am also thankful to all my juniors at VECC for their graceful behaviour and useful suggestions during this time. Special thanks to my colleagues of room no.113; Abhishek, Sukanya and Amal for their favour at different time. A lot of thanks to my batch-mates; Sudipan, Nihar, Younus, Arnab and Manish for being cooperative all the time and bearing with me.

Lastly I would like say that it would never been possible to achieve this goal without the constant encouragement and blessing of my parents, sincere support of my wife, enthusiasm from my brother and the source of all inspiration my little daughter.

SYNOPSIS

The collisions of heavy nuclei at relativistic energies have been generated a great deal of interest, both theoretically and experimentally, since the past few decades. The primary goal of such collisions in the laboratories is to liberate the partons (quarks and gluons) inside the colorless hadron and study the in-medium behaviour of quantum chromodynamics (QCD); the gauge theory of strong interactions. At very high energies the collision between the two Lorentz contracted nuclei is almost transparent and multiple parton-parton scattering and annihilation takes place during their passage. This will lead to creation of a hot and dense matter in which the basic degrees of freedom is partonic rather than hadronic.

It may eventually achieve a local thermal equilibrium if the collision rate of the constituent partons is greater than the expansion rate of the system. This exotic state of matter is known as quark-gluon plasma (QGP); is presumed to exist when the universe was few micro-seconds ($\sim 10^{-6}$ sec) old. The plasma expands and consequently cools and below a certain critical temperature (or energy density) the partons are confined to form hadrons. The lattice QCD simulations, believed to derive QCD properties from the first principle, suggest the transition temperature is near 160 MeV. However the mechanism and order of the quark-hadron phase transition still remains to be challenging problem in high energy nuclear physics. The existence of QGP can be conjectured through the phenomena of i) Jet-quenching ii) Elliptic flow of hadrons and thermal photons iii) Quark number scaling of elliptic flow of hadrons iv) Electromagnetic radiations v) Dissociation of quarkonium states (e.g., J/Ψ, Upsilon) vi) Suppression of heavy mesons etc.

The Relativistic Heavy Ion Collider (RHIC) at Brookhaven National Laboratory and the Large Hadron Collider (LHC) at CERN are the two major heavy ion research facilities currently in operation. The experiments have provided a clear proof of formation of QGP in the collisions of heavy nuclei (e.g. Au or Pb) by ascertaining all the proposed signatures mentioned above. In addition, the observations at RHIC and the LHC experiment have put several constraints on the existing theoretical models of relativistic heavy ion collisions. There exists a number of unresolved issues like; the observed elliptic flow coefficient (v_2) of direct photons at RHIC follows the shape but registers 50% more flow compared to the theoretical prediction.

The present thesis contains a detailed phenomenological analysis of QGP properties through the direct photon intensity interferometry, quenching of large momentum jets and identification of jet-tagged back-scattering photons for Au-Au collisions at the RHIC and Pb-Pb collisions at the LHC energies. The elaboration of each topic is provided below.

Two important theoretical tools used in the present study are Relativistic Hydrodynamics and Perturbative Quantum Chromodynamics (pQCD). The matter created in relativistic heavy ion collisions is assumed to be thermalized at the proper time τ_0(<1 fm/c) after the collision. From this point onwards, Relativistic Hydrodynamics (ideal or viscous) has been used to describe the bulk evolution of the matter until the system loses collectivity due to large mean free path of the constituent particles. In the present work, an ideal relativistic hydrodynamic model has been used with the assumption of longitudinal boost invariance and azimuthally symmetric transverse expansion.

The other tool, pQCD has it's unique importance in describing the production of particles at large momentum in elementary hadron-hadron collisions. The prefix 'Perturbative' is used to signify that the strong interaction coupling (α_s) can be expanded in a perturbation series when the momentum scale (Q) of the associated process is much larger than the typical QCD scale; Λ_{QCD}. Therefore inclusion of Feynman diagrams of higher order in α_s improves the accuracy, while calculating elastic or inelastic parton-parton scattering cross section involving large momentum transfer. The corrections up to Next-to Leading order (NLO) in α_s have been included in the present work.

An Equation Of State (EOS) of hot hadronic matter, consists of all baryons having mass (m) up to 2 GeV and mesons up to 1.5 GeV, has been constructed. The observation of rapid growth of hadronic states near the transition temperature, lead Hagedorn to propose an exponentially increasing hadronic mass spectrum. The current study includes those Hagedorn resonances in the mass region 2$< m <$ 12 GeV. Different thermodynamic quantities like; entropy density, pressure are calculated for the hadronic mixture in the grand canonical ensemble formalism at zero baryonic chemical potential. The derived quantities have also corrected by taking into account the finite volume of hadrons. It has been found that the thermodynamic quantities for volume corrected hadron+Hagedorn gas closely follow their counterparts derived from lattice QCD in the temperature range T< 200 MeV. Next it is matched either with the Bag model EOS or the lattice EOS of quark matter at T= 165 MeV. The Bag model EOS (HHB) admits a first order phase transition with critical temperature 165 MeV whereas the lattice EOS (HHL) exhibits a sharp cross-over for the temperature range, 180 < T< 190 MeV.

The relevant hydrodynamic equations are solved for the two equations of state with identical initial condition for the Au-Au collisions (200A GeV) at the RHIC and Pb-Pb collisions at the LHC (5.5A TeV) energies. It has come out that the thermal particle (pion, kaon, proton) and thermal photon transverse momentum spectra are minimally sensitive to the difference of the two EOS. However interesting differences have been found in the time evolution of average temperature and radial flow of the system. Earlier studies of heavy ion collisions have revealed that the direct photon intensity interferometry is a good probe of history of evolution of the system. Thus the two photon intensity correlation function is calculated for the two equations of state at the average momentum value of the pair 1.7 GeV at RHIC and 1.2 GeV at the LHC energies. The 'normal'coordinates used for this study are the 'outward', 'sideward'and 'longitudinal'momentum differences. The outward and longitudinal correlation function is seen to discriminate between the two EOS.

The energy and system size dependence of jet quenching has been investigated by analyzing the nuclear modification factor of neutral pion production for Au-Au, Cu-Cu collisions at the RHIC (200A GeV) and charged hadron production for Pb-Pb collisions at the LHC (2.76A TeV) energies. NLO pQCD is used for the initial production and then the light partons are assumed to lose energy via gluon bremsstrahlung while traversing through the QGP. The quark-gluon medium is considered as an assembly of static scattering centers at some fixed temperature (or energy density). Inspired of the formalism by Baier et al., three different regimes of parton energy loss are considered in this work. The Bethe-Heitler (BH) regime of incoherent gluon radiations, the LPM regime of partial coherent gluon radiations and the Complete coherence regime where the whole medium behaves like a single scattering center. The energy loss per collision,

ε, is taken proportional to the energy (E) of the fast parton, $\sqrt{E}$ or constant for the BH, LPM and Complete coherence regimes of energy loss respectively. The effect of parton energy loss and nuclear shadowing are included by modifying the vacuum parton fragmentation function. The fluctuation in the number of collisions of the test parton is accounted through the Poisson distribution of scattering centers. The average path length $\langle L \rangle$ of the parton inside the medium is evaluated using optical Glauber model and assuming uniform density of the colliding nuclei. The parameter ε is tuned systematically to get an accurate description of the nuclear modification factor ($\mathrm{R_{AA}}$) of hadron production, from most central to mid-peripheral collisions at the RHIC and LHC energies mentioned earlier.

It has been found that the BH mechanism is operating at the low transverse momentum region; $p_T < 5$ GeV at RHIC and $(5 < p_T < 8)$ GeV at LHC. The LPM mechanism is seen to describe the data well in the intermediate p_T regime, (5–10) GeV at RHIC and (6–15) GeV at LHC. Finally the large momentum part of nuclear modification factor, $p_T > 8$ GeV at RHIC and $p_T > 10$ GeV at LHC, is best explained by the Complete coherence regime of energy loss for all centralities of collision. In addition, an empirical determination of parton energy loss per unit length (dE/dz) in QGP has been carried out. It is found that dE/dz grows linearly with the path length $\langle L \rangle$ at the RHIC and LHC energies for the partons having $p_T >$ 8–10 GeV which contradicts the Ads/CFT based prediction. The magnitude of energy loss per unit length of the parton, also increases by a factor of 2–3 from RHIC to LHC energy.

In non-central collisions, the azimuthal variation in the path length of the probe parton causes an azimuthal anisotropy in the transverse momenta spectra of final state hadrons. Such momentum anisotropy study has been performed at the RHIC and LHC energy, using the energy loss parameter obtained from the earlier $\mathrm{R_{AA}}$ analysis. It has been shown that the predicted azimuthal momentum anisotropy coefficient (v_2) of neutral pions is about 2 times larger than the data for most central collisions (0-10%) and a little better in agreement for mid-peripheral collisions (40-50%) at the RHIC energy. Similar result has been found for the charged hadron momentum anisotropy at the LHC energy. Finally the nuclear modification factor and azimuthal momentum anisotropy of high energy prompt photons at RHIC energy are also calculated. Photons originating from QCD Compton scattering and annihilation, do not suffer energy loss. Only the photons originated from the collinear fragmentation of final state parton are affected by the energy loss before fragmentation, hence contributes to the azimuthal momentum anisotropy. Once again the energy loss parameters from the neutral pion R_{AA} analysis are used. It has been found that the v_2 of direct photons at RHIC is well reproduced by LPM and Complete coherence regime of energy loss in the region of $p_T > 6$ GeV.

According to the mechanism of production, direct photons are classified as i) hard prompt photon ii) pre-equilibrium photon iii) jet-medium backscattering photon and iv) thermal photon. However only the inclusive yield of direct photons have been measured in experiment and isolation of a particular contribution is considerably challenging task.

The jet-medium photons are produced due to scattering of large momentum jets with thermal medium partons in QGP. Hydrodynamic simulations have shown that the source to be dominating in the range of momenta; $2 < p_T < 4$ GeV at RHIC energy. It has been proposed that jet-medium photons exhibit negative azimuthal momentum anisotropy (v_2). However the experimental results are not quite conclusive so far.

In order to identify this source, the production of back-scattering photons opposite to large momentum trigger jets have been studied in the present work. The use of large momentum jets as trigger has two fold advantage: first; the fast partons of the medium often have back-to back correlation with large p_T jets and second; only the hard prompt photons have similar correlation with the jets which eliminates the contribution of pre-equilibrium and thermal photon sources. Due to finite resolution of jet energy measurement in experiment, a finite window in jet energy is chosen rather than a sharp value. The hard prompt photons (direct + fragmentation contribution) are calculated in a narrow angular region (± 15 degrees) on the away-side of trigger jets of momentum 30–35 GeV at RHIC and 60–65 GeV at LHC. They are treated as 'background 'for the jet-medium photons.

The Leading Order (LO) parton spectrum on the away-side has also been estimated in the same kinematical condition. The partons are allowed to propagate through a longitudinally expanding fireball and lose energy before the backscattering occurs to create photons. The energy loss parameter is estimated from the R_{AA} of hadron production at the RHIC and the LHC energy.

At LO, a strong correlation is observed between the trigger jet momentum and back-scattered photon momentum without parton energy loss. Switching on energy loss the back-scattered photon peak is seen to be shifted towards low momentum. The back-scattered photons with energy loss are treated as ‘signal’. At NLO, the perfect balance between the trigger jet and away-side jet momentum has been lost. In this work, the signal has been evaluated up to LO accuracy whereas the background has been estimated at LO and NLO both. The experimental observable, R_{AA}, has been defined as the ratio of invariant yield of background photons in pp collisions over the sum of invariant yield of signal and background photons in AA collisions. An enhancement in R_{AA} is clearly seen just below the trigger jet window both at the RHIC and the LHC energy, affirms the existence of backscattering process in QGP. With the NLO background, the signal weakens but survives. The height of the peak is found to reflect the temperature of the medium when the back-scattering had occurred whereas the width of the peak is sensitive to the parton energy loss. The effect of trigger jet energy loss has been investigated and found to smear out the potential signal.

List of Figures

Contents

Chapter 1

Introduction

1.1 Why do heavy ion collisions ?

The prodigious research in basic sciences over the past few centuries has been succeeded to conclude that all static and dynamic physical processes happened in the universe on the length scale ranging from few Fermi ($\sim 10^{-15}$m) to few parsec ($\sim 10^{16}$m) are governed by four basic interactions; strong, electromagnetic, weak and gravitational. These interactions are found enough to account from the synthesis of atomic nuclei to the formation of galaxies. The strong interaction is responsible for the bound structure of nucleons and nuclei. The shape and size of atoms, molecules, solids, and liquids are determined by electromagnetic interaction. The weak interaction determines the stability and composition of atomic nuclei and the gravitational interaction controls the dynamics of all rigid bodies on macroscopic length scale.

The gravitational and electromagnetic were known to be the only fundamental interactions until the celebrated alpha scattering experiment by Lord Rutherford in 1911 which revealed the inner structure of atoms. This pioneering experiment lead scientists to use high energy particle beams to explore deep inside the nucleus (and nucleon). The first evidence of inner constituents of nucleon came from the deep-inelastic lepton-proton scattering experiments [1]. They are named as quarks by Murray Gell-Mann which carry fractional electric charges. At the same time Richard Feynman introduced the concept of parton model which showed that a substantial fraction of proton's momentum is carried by charge neutral partons. These are called gluons, the mediator of strong interaction that holds the quarks together. Thus the theory of strong interaction developed in early

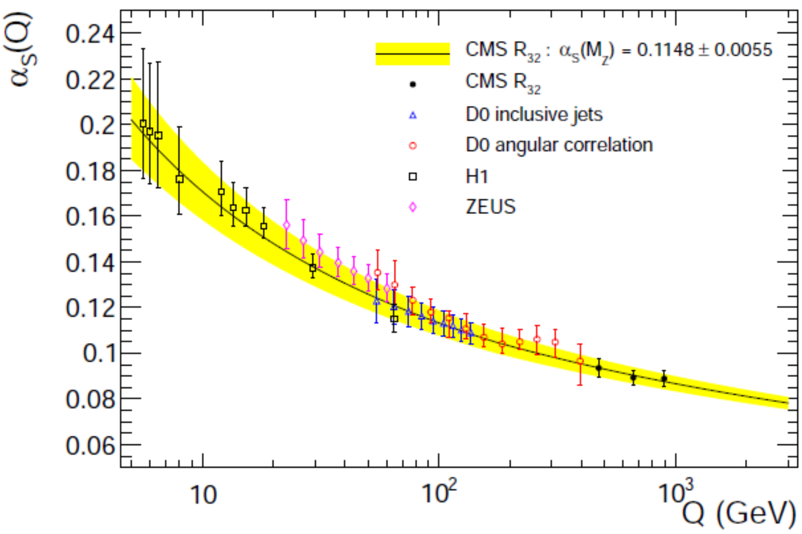

Figure 1.1: Recent measurements of strong coupling α_s as a function of momentum scale Q at the Large Hadron Collider experiment (Source: Eur. Phys. J. C **73** (2013) 2604).

1970's to describe the interaction between quarks and gluons is called Quantum chromodynamics (QCD). Yoichiro Nambu proposed an additional quantum number of QCD called *Color*; which has been confirmed later in the measurements of cross-section for electron-positron annihilation to hadrons [2].

The two renowned properties of QCD are *Asymptotic freedom* and *Infrared Slavery* or *Confinement*. They can be naively explained through the variation of strong interaction coupling constant ($\alpha_s(Q)$) with the momentum transfer scale Q (see Fig. 1.1). In the large momentum transfer limit; the effective coupling between the quarks becomes small and the interaction between them is so weak that they behave as free particles. This property is known as *asymptotic freedom* which is well described by perturbative techniques of QCD. However in the small momentum transfer limit; the effective coupling rises to very large value and the quarks are strongly bonded. The numerical simulations of QCD suggest the static quark-anti-quark potential at long distances varies as $\sim Kr$, which is responsible for the *confinement* property. The unsolved mysteries of high energy physics like the generation of mass and spin of hadrons lies in this domain of QCD.

Following the idea of *asymptotic freedom*, Collins and Perry in 1975 [3] suggested that at very high densities (or temperatures) a deconfined state of quarks and gluons can be

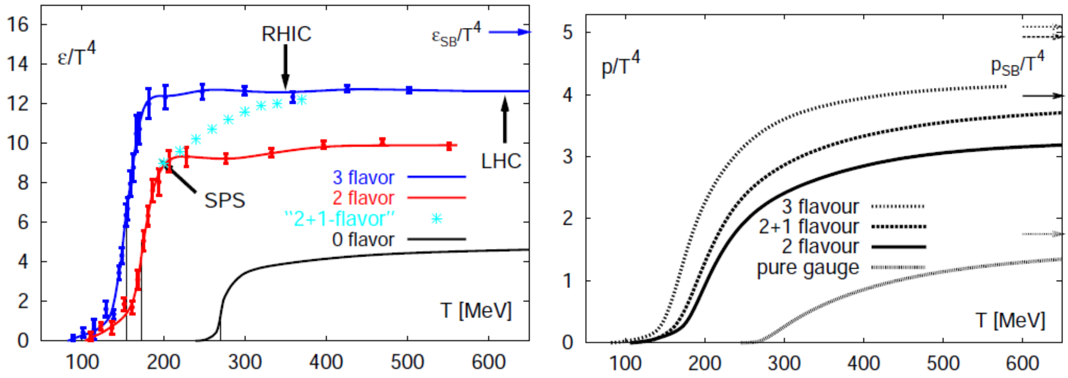

Figure 1.2: The scaled energy density (ε/T^4) (Left) and pressure (p/T^4) (Right) as a function of temperature from lattice QCD [6] simulations for various quark flavors. Note that the variation of pressure is continuous near T_c where the energy density changes abruptly.

achieved. At densities about 2-3 times the normal nuclear matter density, the hadrons tend to overlap and the individual quarks inside them lose their identity. The long range interactions are screened in this deconfined matter due to many body effects. Such an exotic state of matter has been argued to exist at the core of neutron star and few micro-seconds after the cosmological Big-Bang when the temperature of our newborn universe is about 10^{12}K [4]. This novel state of matter later referred as the Quark-Gluon Plasma (QGP) [5]. It was suggested that the celestial conditions of formation of QGP can be achieved in laboratory in the collisions of heavy nuclei at relativistic energies. Thus heavy ion program has started for the search of QGP at different laboratories worldwide motivated by the following questions: (i) testing the behaviour of QCD at high temperature (T) and baryon density (or baryo-chemical potential μ_B), (ii) exploring the QCD phase diagram in (T-μ_B) plane and the order of phase transition, (iii) investigating the mechanism of *confinement* of quarks in hadrons.

The numerical scheme developed to calculate the QCD properties at finite temperature (or density) on a discrete space-time lattice is known as lattice QCD. These computations show a rapid rise in energy density (ε/T^4) when the matter reaches a critical temperature $T_c \sim 160$ MeV [6]. This indicates the basic degrees of freedom of matter has been changed from hadrons to partons. The hadronic matter below T_c has roughly three degrees of freedom, corresponding to three iso-spin states of pions. Above T_c, the matter consists of 2-3 active flavors of quark (and anti-quark) and gluons. Thus

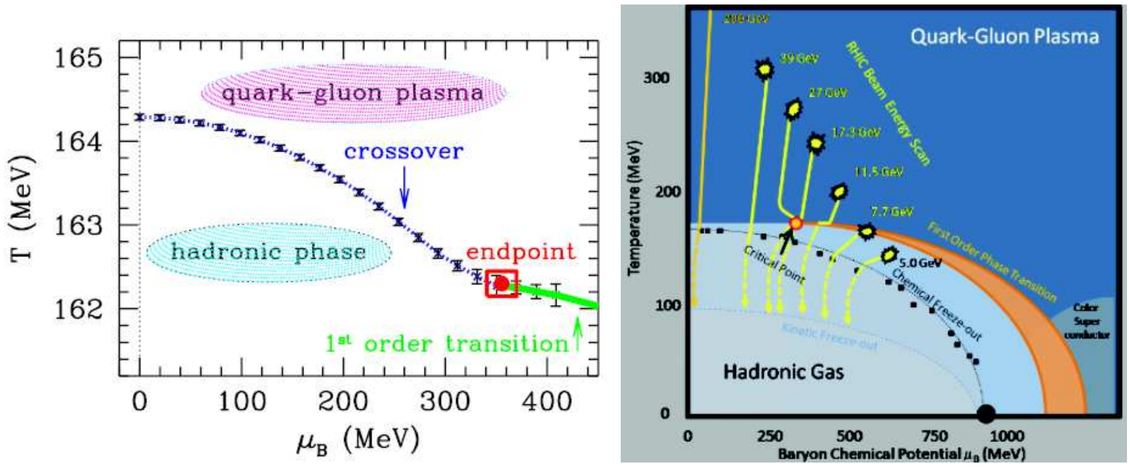

Figure 1.3: (Right) Lattice prediction of QCD phase diagram and location of critical point on T-μ_B plane in physical units [7].(Left) Schematic diagram of RHIC beam energy scan program for the search of QCD critical point [8].

the total degrees of freedom in QGP phase becomes 40-50. It is clearly visible from Fig. 1.2 that the energy density increases as we include more number of flavor.

Another distinctive suggestion from lattice QCD is that the QGP phase may admit two types of transition to the hadronic phase; one at high baryon density (μ_B) and the other at high temperature. The phase transition at high μ_B is considered a first-order transition whereas at high temperatures it is a cross-over transition, in a strict thermodynamical sense. In addition, the theory predicts a *critical end point* where the first-order phase boundary ends and the cross-over region starts (See Fig. 1.3). However the exact location of *critical end point* is not precisely determined till now. This motivates the Beam Energy Scan Program where the entire (T-μ_B) plane can be mapped in experiment by varying the center of mass energy ($\sqrt{s}$) of the colliding nucleon pair. The project is currently operated by RHIC at the Brookhaven National Laboratory (BNL). The STAR collaboration of RHIC is measuring the higher moments of fluctuation of conserved quantities (like; net charge, net baryon etc.) on event-by-event basis. These quantities are related to the thermodynamic susceptibilites which are estimated in lattice QCD [8].

Experimental facilities

Heavy ion collisions at moderate energies (1-2 GeV/nucleon) were first performed at BEVALAC in Lawrence Berkeley National Laboratory. However the attained energy density was not enough to produce QGP phase. Next developments included of Alternating Gradient Synchrotron (AGS) experiment at BNL and Super Proton Synchrotron (SPS) experiment at CERN. Both of them collided different species of nuclei at various energies ($\sqrt{s} \approx$ 4-17 AGeV) in fixed target mode. The notable heavy ion runs at AGS and SPS are Au+Au 11.6 AGeV and Pb+Pb 158 AGeV respectively. The vast amount of data collected at SPS already indicates the onset of QGP phase [9]. Based on the data of SPS and theoretical predictions, heavy ion community proposed to build a collider machine where we have about a factor of 10 rise in $\sqrt{s}$. Thus the Relativistic Heavy Ion Collider (RHIC) experiment constructed at BNL, achieved Au+Au collisions at $\sqrt{s}=$ 200 AGeV. Results from the RHIC experiment for the first time has given a clear evidence of formation of deconfined quark-gluon matter through the observation of various proposed signatures [10]. Currently RHIC is involved in low energy heavy ion runs ($\sqrt{s}=$ 7.7-63 AGeV) for the search of QCD critical point. Going beyond RHIC energies, CERN has commissioned the Large Hadron Collider (LHC) which is believed to be the largest man-made machine on the earth. The LHC is designed to collide heavy ion beams up to energy $\sqrt{s}=$ 5.5 ATeV. The results from the first heavy ion runs (Pb+Pb at 2.76 ATeV) in November, 2010 have drawn considerable attention of the community [11].

The RHIC and LHC experiments are motivated to study the QGP properties at low μ_B and high temperatures. In future the Compressed Baryonic Matter (CBM) experiment at FAIR/GSI laboratory is being designed to investigate the QCD phase diagram at high μ_B and moderate temperature, which is complementary to the study of nuclear matter at the RHIC and LHC experiments. This experiment will be fixed target ($\sqrt{s}=$ 10-45 GeV/nucleon) but with higher beam luminosity compared to AGS or SPS. This will facilitate observation of strange and charm particles in addition.

1.2 Space-time picture of heavy ion collision

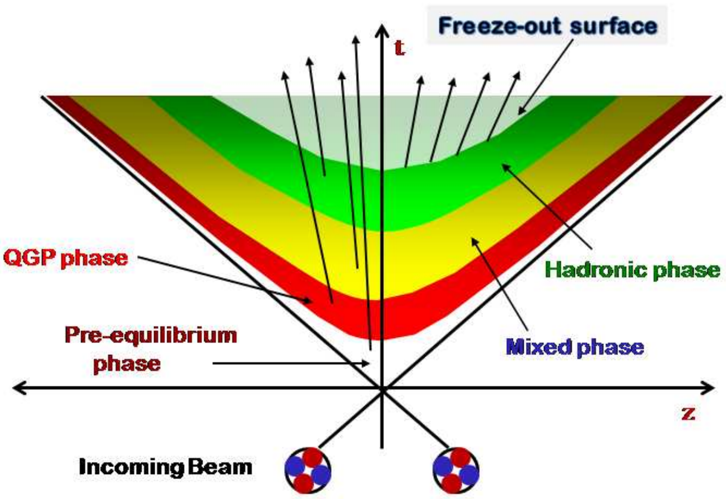

Figure 1.4: Evolution of matter created in relativistic heavy ion collisions in 2D Minkowski space. The arrows indicate the emission of hadrons after the kinetic freeze-out whereas photons (real and virtual) are emitted from all stages of evolution.

The theoretical study motivated space-time diagram of relativistic heavy ion collision is depicted in Fig. 1.4. We shall explain briefly the dynamics of each stages of evolution separated by isentropic contours of relativistic proper time τ.

1. Before the collision, two nuclei approach each other at relativistic speed. The longitudinal dimensions are then Lorentz contracted in the center of mass frame. All the physical phenomenon will be confined within the world lines traced by the two nuclei. The initial state is described by the Glauber model of nuclear collisions which is based on independent nucleon-nucleon scattering picture [13]. The production of energy density (or entropy density) depends on number density of *wounded nucleons* and number of *binary collisions*. The model is quite successful in explaining observed momentum spectra and elliptic flow of particles but fails in case of two particle correlations and higher order flow harmonics [12]. The modern description includes the Color-Glass description of the colliding nuclei [14] which assumes that at very high energies the nucleus is dominated by weakly coupled gluon matter. The initial energy density is determined from the classical evolution of gluonic field equations.

2. At the proper time $\tau = 0$ (i.e. the collision point), the two nuclei strike each other and the partons inside them start interacting. The parton-parton inelastic scattering and fusion may lead to an equilibrated partonic matter if the scattering rate is larger than the expansion rate of the system. This is called the pre-equilibrium phase. The scatterings often involve large momentum transfer ($Q \sim 10$ GeV), which are responsible for creation of hard jets. The cross-section of these hard processes are calculated using perturbative QCD. Observation of these hard jets (hadron, direct photon or heavy quark) in experiment helps us to gain knowledge about pre-equilibrium dynamics.

3. An obvious consequence of the partonic interactions is that the system rapidly approaches *thermal equilibrium* at some proper τ_0 after the initial impact. The liberated partons of the incident nuclei form a strongly coupled fluid like matter; called the Quark-Gluon Plasma. The average energy density at the onset of QGP phase for Au+Au collisions at RHIC is about 20 GeV/fm^3, of course strongly depends on the equilibration time τ_0. The matter subsequently expands and cools, controlled by the laws of ideal or viscous relativistic hydrodynamics and the equation of state (EOS). The phenomenological input to the hydrodynamic simulation is the initial thermalization time τ_0 which is widely taken as <1 fm/c [15]. Experimental data indicates the matter produced at RHIC and LHC exhibits nearly perfect fluid behaviour with only a very small viscosity [16].

   As the energy density decreases, quark matter undergoes a 1st order or cross-over phase transition to hadronic matter. In case of 1st order transition, there shall be a mixed phase where both QGP and hadronic phase co-exist at the transition temperature T_c. During the mixed phase the temperature remains constant and the difference of energy of the two phases is utilized in the expansion of matter.

4. The partons start getting confined into hadrons at energy density ~0.7-1 GeV/fm^3. The matter is now considered as strongly interacting hot hadronic gas (mostly consisting of pions). If we assume that the local thermal equilibrium is still maintained, the evolution is described by relativistic hydrodynamics. However non-equilibrium transport equations have also been used to describe this phase [17]. The matter

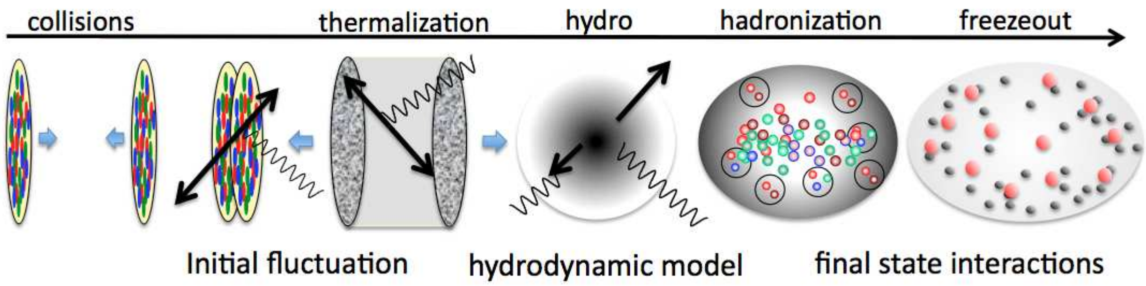

Figure 1.5: Pictorial representation of different stages of heavy ion collision. The wavy line denote the photons and the arrow denotes the hard jets. Art courtesy of C. Nonaka and M. Asakawa [15].

subsequently expands until the mean collision rate becomes smaller than the local expansion rate. At this point the hydrodynamic description breaks down and we get a freely streaming gas of hadrons using Copper-Frye hypothesis [18]. This is known as the *kinetic freeze-out* of the system. The condition of decoupling from hydrodynamics is specified by quoting a kinetic freeze-out temperature or an energy density in the simulation.

A good agreement between the particle ratios observed at RHIC and the statistical thermal models suggests that there is a chemical freezout of the system where the number density of each hadrons becomes fixed. Recent analyses has shown the chemical freeze-out temperature is very close to T_c [19]. The inelastic collisions between the constituents have stopped at this point. However, elastic scatterings continue till the kinetic freeze-out. The momentum distribution of final state hadrons solely depends on the kinetic freeze-out criterion.

1.3 Evidences of formation of QGP

The information of produced particle's momentum, rapidity etc. reaching at the detector, is integrated over space and time. Thus it is very difficult in experiment to disentangle the contribution of a particular phase. However theoretical models are constructed under certain assumptions and controlled by a number of parameters. Therefore direct mapping between experiment and theory enables us to characterize a particular phase. There are ample signatures proposed in favour of existence of QGP phase from theory side. Notable achievements come from the observation of; (i) Collective flow of hadrons (and thus photons) (ii) Jet-quenching (iii) Electromagnetic radiation (iv) Constituent quark number scaling of flow (v) Strangeness enhancement (iv) Suppression of J/Ψ and Υ states. Jet-quenching and Electromagnetic radiation are elaborately discussed in the later part of the thesis. We briefly discuss rest of them at present.

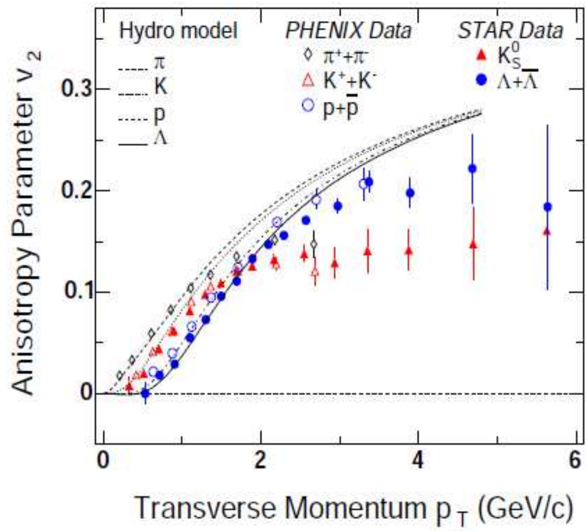

Figure 1.6: The elliptic flow coefficient v_2 for various mesons and baryons measured at RHIC for Au+Au collisions at 200A GeV along with predictions from ideal hydrodynamic simulation [20].

■ **Collective Flow**: The evidence for creation of "bulk matter "at RHIC comes through the collective flow of final state hadrons. The study of collective flow gives key information about early thermalization and equation of state of the plasma. It is measured in experiment through different Fourier coefficients of azimuthal (ϕ) distribution of hadrons with respect to one of the collision symmetry plane.

$$\frac{dN}{d\phi} \propto (1 + 2v_1 \cos\phi + 2v_2 \cos 2\phi + 2v_3 \cos 3\phi + 2v_4 \cos 4\phi + ...), \tag{1.1}$$

where v_1, called the directed flow, describes the side-ward motion of the particles. It is believed that v_1 is generated during nuclear passage time thus sensitive to the properties of matter created at initial stages of collision [21]. v_2, known as the elliptic flow, measures the momentum anisotropy of produced hadrons at low transverse momentum (p_T) [22]. It has been shown by hydrodynamic simulations that the collective flow of bulk matter

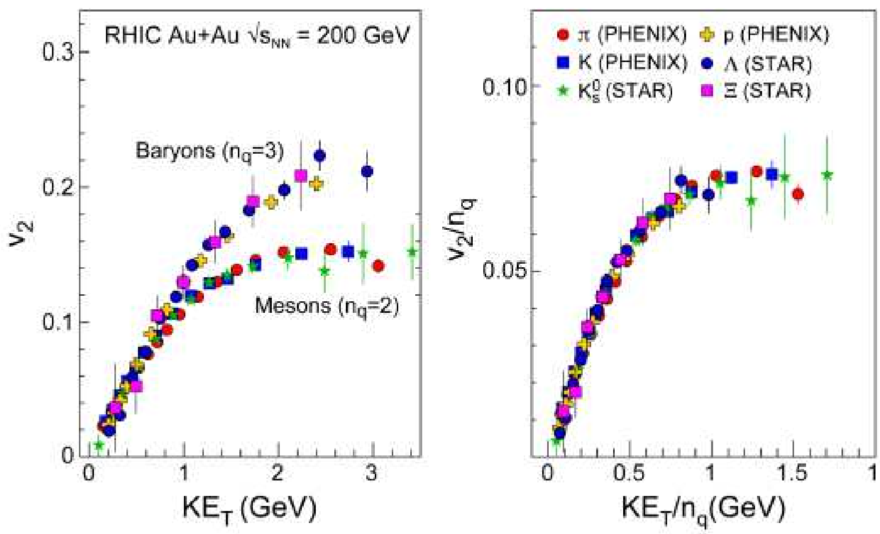

Figure 1.7: (Left)The differential elliptic flow v_2 vs. transverse kinetic energy for different hadrons for Au+Au collisions at 200A GeV. (Right) The same when scaled with number of valance quarks follow an universal line irrespective of hadron type [27].

converts the initial spatial anisotropy to the momentum anisotropy of final state particles in non-central collisions [23]. RHIC experiment has first shown the remarkable agreement of v_2 for π, K, p, Λ hadrons and ideal hydrodynamic calculations for $p_T \leq 2$ GeV/c (see Fig. 1.6) which validates the formation of a thermalised dense matter in ultra-relativistic nuclear collisions. Similar agreement at the recent LHC energy has been found by a Hydro+Transport approach [24]. The elliptic flow of direct photons has been proposed a powerful signature of early time dynamics complementary to the hadronic flow [25]. Direct photon elliptic flow reflects the momentum anisotropy of thermalised quarks from which they are emitted, thus contains valuable information about the spatial deformation of initial state. However the disagreement between theoretical prediction and the recent measurement of direct photon v_2 at RHIC [26] pose a serious question to the community.

■ **Quark number scaling of flow**: The plot of elliptic flow parameter v_2 of identified hadrons vs. the transverse kinetic energy (KE_T) at RHIC exhibits interesting behaviour (Fig. 1.7). At low KE_T regime, all curves follow a single line which is well predicted by hydrodynamics. For higher KE_T ($\geq$1 GeV), a clear discrimination between baryons and mesons is seen which breaks the hydrodynamic expectation. An explanation of this phenomena comes from the coalescence [28] or recombination [29] of valance quarks which is considered as an alternative to fragmentation mechanism of hadron production at intermediate p_T. Both models are assuming the existence of a thermalised partonic matter. Also the models predict a scaling of v_2 with the number of valance quarks (n_q) inside the hadron [30]. This indeed beautifully confirmed by experimental data when (v_2/n_q) is plotted against (KE_T/n_q). This observation confirms that the flow anisotropy is developed in early partonic phase.

■ **Strangeness enhancement**: The increased production of strange particles in relativistic heavy ion collisions compared to proton-proton (pp) collisions has been proposed a signature of QGP formation by Rafelski and Müller [31]. They showed that the dominant channel of strangeness production is through gluon fusion; $gg \rightarrow s\bar{s}$. It was motivated by the fact that K^+/π^+ ratio is seen little higher than the strangeness content ($s\bar{s}/u\bar{u}d\bar{d}$) of a thermally and chemically equilibrated hadron gas [32]. Now one hopes to produce a baryon rich quark-gluon plasma at low collision energies (e.g. SPS experiment) in which chemical potential of u and d quarks are non-zero. But the s quark has zero chemical potential as the colliding nuclei initially contain no strangeness. Thus it is easier to produce $s\bar{s}$ pair in the medium compared to $u\bar{u}$ or $d\bar{d}$ pair. The anti-strange quark ($\bar{s}$) either combined with valance u, d quarks give rise to K^+, K^0 or with $\bar{u}$, $\bar{d}$ sea anti-quarks yield K^-, $\bar{K^0}$ mesons respectively. The contribution of sea u, d quarks to the strange meson production is assumed small for the collision energies available at SPS or RHIC. As the quarks and anti-quarks are produced by differing amount, the K^+/π^+ and K^-/π^- ratio measured in experiments [33] are found to be dissimilar. The strangeness enhancement can also be understood from statistical mechanical consideration. The high multiplicity events for heavy ion reactions are usually explained by grand canonical ensemble. However the small systems produced in $p+p$ collisions are described by canonical ensemble. Thus the process which is enhanced in heavy ion reactions, is actually suppressed in $p+p$ reactions due to reduced phase-space.

■ **Suppression of J/Ψ and Υ states**: J/Ψ and Υ are the bound states of $c\bar{c}$ and $b\bar{b}$ respectively. The heavy quark pair $Q\bar{Q}$ is believed to be produced in the initial hard collisions and their bound state can be described by the non-relativistic potential $\mathrm{V(r)} = \sigma \mathrm{r} - \alpha/\mathrm{r}$ at zero temperature. Now the binding potential between Q and $\bar{Q}$ inside QGP medium is modified by a factor $\exp(-\mathrm{r}/\mathrm{r_D})$ (where $\mathrm{r_D}$ is the Debye screening radius); due to presence of deconfined color charges. The heavy quark pair will form a bound state in QGP when the Debye screening radius is much larger than the ground state radius of quarkonium otherwise they dissociate. Now the level of screening increases with rise in energy density (or temperature) of the system. Considering the fact that quarkonium states have certain binding energies, they will dissociate in QGP at certain energy density thresholds. Thus the suppressed production of quarkonium states in high energy nuclear collisions is considered an important signature of deconfinement, was first suggested by Matsui and Satz [34]. The PHENIX collaboration at RHIC has performed several measurements on J/Ψ suppression at different collision centralities and energies [35]. Due to small production cross-section at earlier collider energies, the Υ states have been recently measured in Pb+Pb collisions at LHC by the ALICE collaboration [36].

1.4 Organization of the thesis

The present thesis goes as following. In chapter 2 we have discussed ideal relativistic hydrodynamic equations, formalism of equation of state (EOS) of the strongly interacting matter, thermal particle and photon production at RHIC and LHC energies, and spacetime evolution of thermal photon emitting source. Chapter 3 contains the description of first order and second interference in optics and then it's application to heavy ion collision, parameterization of two photon correlation function and the results for heavy ion collisions at RHIC and LHC energies. Chapter 4 is devoted to jet quenching studies which gives an introduction and then discusses the formalism of parton energy loss, nuclear modification of neutral pion and charged hadron production for different centralities of collision at RHIC and LHC, and suppressed production and azimuthal anisotropy of prompt photons at RHIC. In chapter 5 we have reviewed different sources of direct photons in heavy ion collisions, then outline the calculation of rate of production of jet-medium back-scattered photons in QGP. We have described our strategy of separating jet-medium photons from other sources using trigger jets. We have computed examples for kinematic situations at RHIC and LHC and discussed the effect of parton energy loss as well as trigger jet energy loss on back-scattering photon production. Finally in chapter 6, all research works presented in the thesis have been summarized. In the appendices we have outlined the calculation of finite volume correction for hadrons and invariant momentum spectra of hadrons at the kinetic freeze-out surface.

Chapter 2

Construction of EOS and Hydrodynamic Evolution

2.1 Introduction to Relativistic Hydrodynamics

The laws of ideal hydrodynamics can be used for evaluation of a strongly interacting system, produced after high energy hadronic collision was first proposed by Landau [37]. The thumb-rule for applicability of hydrodynamics is that the mean free path (λ) of the constituent particles should be much much less than typical length of the system (λ << L). This essentially means the constituent particles of the system scatter very frequently. The system eventually achieves *local thermal equilibrium* if the microscopic collision time scale becomes very short compared to the macroscopic time scales related to the response of the system under small changes in density, pressure, or temperature. We write the local conservation equations of energy-momentum and conserved charges for a thermalized fluid cell:

$$\partial_\mu T^{\mu\nu} = 0, \tag{2.1}$$

$$\partial_\mu {J_i}^\mu = 0, \;\; i = 1, ..., n. \tag{2.2}$$

In addition, the second law of thermodynamics provides:

$$\partial_\mu S^\mu \geq 0, \tag{2.3}$$

where $T^{\mu\nu}$ is the energy-momentum tensor, ${J_i}^\mu$ is conserved current of i'th type, S^μ is the entropy current. At present, we take i=1 (say, J^μ= net baryon current) for simplicity.

The ideal fluid dynamic decompositions of the above quantities are given by:

$$T^{\mu\nu}_{ideal} = (e + P)u^\mu u^\nu - g^{\mu\nu}P, \tag{2.4}$$

$$J^\mu_{ideal} = n_B u^\mu, \tag{2.5}$$

$$S^\mu_{ideal} = s u^\mu \tag{2.6}$$

u^μ is the four-velocity of the fluid cell and $g^{\mu\nu}$=diag(+1,-1,-1,-1) is the metric tensor. The local charge (baryon) density n_B, energy density e, pressure P and entropy density s are defined in the local rest frame of the fluid. These quantities are related by the thermodynamic relation

$$Ts = e + P - \mu_B n_B, \tag{2.7}$$

where μ_B is the chemical potential associated with the conserved baryon number. The *local rest frame* of a fluid cell is the Galilean frame in which all momentum components vanish. The fluid has isotropic properties in the rest frame due to local thermodynamic equilibrium. In the rest frame of fluid; u^μ= (1,0,0,0). In a global frame where the fluid rest frame moves with a velocity $\vec{v}$, u^μ is given by:

$$u^\mu = (u^0, \vec{u}) = \gamma(1, \vec{v}), \tag{2.8}$$

where $\gamma = 1/\sqrt{1 - \vec{v}^2}$ is the Lorentz boost. u^μ acts like a four vector under Lorentz transformations.

$$u^\mu = \Lambda^\mu_\nu u^\nu \tag{2.9}$$

also reduces to a scalar upon contraction,

$$u^\mu u_\mu = (u^0)^2 - (\vec{u}^2) = 1. \tag{2.10}$$

The zeroth component of the Lorentz transformation matrix (Λ^μ_ν)

$$u^\mu = \Lambda^\mu_0 \cdot 1 = \Lambda^\mu_0, \tag{2.11}$$

where $\gamma \approx 1$ in the first order of velocity $\vec{v}$. The other components can be obtained as;

$$\begin{aligned} g^{\rho\sigma} &= g^{\mu\nu}\Lambda^\rho_\mu \Lambda^\sigma_\nu \\ &= g^{00}\Lambda^\rho_0 \Lambda^\sigma_0 + g^{ii}\Lambda^\rho_i \Lambda^\sigma_i \end{aligned}$$

$$\Lambda_i^\rho \Lambda_i^\sigma = \Lambda_0^\rho \Lambda_0^\sigma - g^{\rho\sigma} = u^\rho u^\sigma - g^{\rho\sigma} \tag{2.12}$$

Thus in the first order of $\vec{v}$, Λ_ν^μ writes as:

$$\begin{pmatrix} 1 & v_x & v_y & v_z \\ v_x & 1 & 0 & 0 \\ v_y & 0 & 1 & 0 \\ v_z & 0 & 0 & 1 \end{pmatrix} \tag{2.13}$$

The energy-momentum tensor of a fluid element in rest frame:

$$T_{rest}^{\mu\nu} = \begin{pmatrix} \epsilon & 0 & 0 & 0 \\ 0 & P & 0 & 0 \\ 0 & 0 & P & 0 \\ 0 & 0 & 0 & P \end{pmatrix} \tag{2.14}$$

Now the energy-momentum tensor of a fluid element moving with arbitrary velocity $\vec{v}$ is obtained due to Lorentz transformation

$$\begin{aligned} T_{global}^{\rho\sigma} &= \Lambda_\mu^\rho \Lambda_\nu^\sigma T_{rest}^{\mu\nu} \\ &= \Lambda_0^\rho \Lambda_0^\sigma T_{rest}^{00} + \Lambda_i^\rho \Lambda_i^\sigma T_{rest}^{ii} \\ &= \epsilon u^\rho u^\sigma + (u^\rho u^\sigma - g^{\rho\sigma})P \end{aligned}$$

$$\begin{aligned} T_{global}^{\rho\sigma} &= (\epsilon + P)u^\rho u^\sigma - P g^{\rho\sigma} \\ &= \begin{pmatrix} \epsilon & (\epsilon+P)v_x & (\epsilon+P)v_y & (\epsilon+P)v_z \\ (\epsilon+P)v_x & P & 0 & 0 \\ (\epsilon+P)v_y & 0 & P & 0 \\ (\epsilon+P)v_z & 0 & 0 & P \end{pmatrix} \end{aligned} \tag{2.15}$$

The energy-momentum tensor $T^{\mu\nu}$ is a symmetric (4×4) tensor of rank 2. This has 10 independent components. Now we discuss the significance of it's different components,

- T^{00} represents the energy density.
- T^{k0} represents the energy flux along the direction k.
- T^{0l} represents the momentum density along the direction l.
- T^{kl} represents the flux of l^{th} component of momentum density along direction k.
- T^{kk} represents the pressure.

The momentum density for non-relativistic fluid is $\rho\vec{v}$, where ρ is the mass density. For a relativistic fluid, mass density is replaced by (ϵ + P), rather than energy density (ϵ). The pressure also contributes to the inertia of the fluid. The quantity (ϵ + P) is called the heat function per unit volume of the fluid.

2.1.1 Ideal Hydrodynamic equations

Now we derive the equations of motion for a perfect fluid moving with four-velocity u^μ [38]. We start with the equations of local energy-momentum conservation and local baryon number conservation,

$$\partial_\mu T^{\mu\nu} = 0, \tag{2.16}$$

$$\partial_\mu {J_B}^\mu = 0. \tag{2.17}$$

Projecting $T^{\mu\nu}$ parallel to u_ν:

$$\begin{aligned} & u_\nu \partial_\mu T^{\mu\nu} = 0 \\ \Rightarrow \quad & u_\nu \partial_\mu [(\epsilon + P) u^\mu u^\nu - g^{\mu\nu} P] = 0 \\ \Rightarrow \quad & u^\mu \partial_\mu (\epsilon + P) + (\epsilon + P)\partial_\mu u^\mu + (\epsilon + P) u^\mu u_\nu \partial_\mu u^\nu - u_\nu \partial^\nu P = 0 \end{aligned}$$

Using $u^\nu u_\nu = 1$, we get $u_\nu \partial_\mu u^\nu = 0$

$$\begin{aligned} & u^\mu \partial_\mu \epsilon + u^\mu \partial_\mu P + (\epsilon + P)\partial_\mu u^\mu - u_\nu \partial^\nu P = 0 \\ \Rightarrow \quad & u^\mu \partial_\mu \epsilon + (\epsilon + P)\partial_\mu u^\mu = 0 \\ \Rightarrow \quad & \dot{\epsilon} + (\epsilon + P)\theta = 0 \end{aligned} \tag{2.18}$$

where we have used the notation $u\cdot \partial a \equiv \dot{a}$ is the comoving time derivative and $\partial \cdot u \equiv \theta$ is known as the local expansion rate of the system.

Projecting $T^{\mu\nu}$ perpendicular to u^ν:

$$\begin{aligned} & \Delta_{\nu\lambda} \partial_\mu T^{\mu\nu} = 0 \\ \Rightarrow \quad & (g_{\nu\lambda} - u_\nu u_\lambda)\partial_\mu [(\epsilon + P) u^\mu u^\nu - g^{\mu\nu} P] = 0 \\ \Rightarrow \quad & g_{\nu\lambda} \partial_\mu (\epsilon + P) u^\mu u^\nu + (\epsilon + P) g_{\nu\lambda} u^\mu \partial_\mu u^\nu \\ + \quad & (\epsilon + P) g_{\nu\lambda} u^\nu \partial_\mu u^\mu - g_{\nu\lambda} g^{\mu\nu} \partial_\mu P - u_\nu u_\lambda (u^\mu u^\nu)\partial_\mu (\epsilon + P) \\ - \quad & (\epsilon + P)[u_\nu u_\lambda u^\nu \partial_\mu u^\mu + u_\nu u_\lambda u^\mu \partial_\mu u^\nu] + u_\nu u_\lambda g^{\mu\nu} \partial_\mu P = 0 \end{aligned}$$

$$
\begin{aligned}
\Rightarrow \quad & u^\mu u_\lambda \partial_\mu(\epsilon+P) + (\epsilon+P)[u^\mu \partial_\mu u_\lambda + u_\lambda \partial_\mu u^\mu] - \partial_\lambda P \\
- \quad & u_\lambda u^\mu \partial_\mu(\epsilon+P) - (\epsilon+P)[u_\lambda \partial_\mu u^\mu + u_\lambda u^\mu u_\nu \partial_\mu u^\nu] \\
+ \quad & u^\mu u_\lambda \partial_\mu P = 0
\end{aligned}
$$

Using $u_\nu \partial_\mu u^\nu = 0$, we get

$$
\begin{aligned}
& (\epsilon+P) u^\mu \partial_\mu u_\lambda - \partial_\lambda P + u_\lambda u^\mu \partial_\mu P = 0 \\
\Rightarrow \quad & (\epsilon+P)\dot{u} - \nabla_\mu P = 0 \qquad (2.19)
\end{aligned}
$$

Where $\nabla_\mu = \Delta_{\mu\nu}\partial^\nu P = (g_{\mu\nu} - u_\mu u_\nu)\partial^\nu P = \partial_\mu P - u_\mu u^\nu \partial_\nu P$

Conservation of net Baryon number

$$
\begin{aligned}
& \partial_\mu {J_B}^\mu = 0 \\
& \partial_\mu (n_B u^\mu) = 0 \\
& u^\mu \partial_\mu n_B + n_B \partial_\mu u^\mu = 0 \\
& \dot{n_B} + n_B \theta = 0 \qquad (2.20)
\end{aligned}
$$

The eq. (2.18) and (2.20) describe the variation of local energy density and baryon density due to expansion of the system, while the eq. (2.19) describes the acceleration of the system driven by the local pressure gradient with $(\epsilon + P)$ acts as inertia of the fluid. These are the most general equations of ideal relativistic hydrodynamics. They can be solved using a particular velocity profile and coordinate system. It turns out that the equations are much more easily solvable if we change the space-time coordinates (t, z) to the light cone variables (τ, η).

$$\tau = \sqrt{t^2 - z^2} \qquad (2.21)$$

is the longitudinal proper time and

$$\eta = \frac{1}{2} ln \frac{(t+z)}{(t-z)} \qquad (2.22)$$

is called the space-time rapidity.

Going from center of mass frame to Lab frame (i.e., applying a Lorentz boost along the z axis), τ remains invariant while the rapidity changes by a constant amount. Thus one solves the hydrodynamic solutions at certain rapidity, then applying a boost to get solutions at other rapidities. The transformation of coordinates is done by using:

$$t = \tau \ \cosh\eta \tag{2.23}$$

$$z = \tau \ \sinh\eta \tag{2.24}$$

Also the derivatives are transformed as

$$\frac{\partial}{\partial t} = \cosh\eta\frac{\partial}{\partial\tau} - \frac{\sinh\eta}{\tau}\frac{\partial}{\partial\eta} \tag{2.25}$$

$$\frac{\partial}{\partial z} = -\sinh\eta\frac{\partial}{\partial\tau} + \frac{\cosh\eta}{\tau}\frac{\partial}{\partial\eta} \tag{2.26}$$

2.2 Construction of Equation of State

2.2.1 The Hadron Resonance Gas Model

In the preceding section, Eq.(2.18– 2.20) consists of 5 equations and there are 6 unknowns; n_B, e, P and 3 components of local fluid velocity $\vec{v}$. To close the set of equations, we invoke a relation between the local pressure and energy density known as the *Equation of State* (EOS), $P = P(e, n_B)$.

In the present work, we have constructed a hadron resonance gas (HRG) model which includes all baryons of mass (m) $\leq$ 2 GeV and all mesons of m $\leq$1.5 GeV and their corresponding anti-particles. The discrete part of the hadron mass spectrum is given by:

$$\rho_{\text{dis.}} = \sum_{i}^{m_i \leq M} g_i \ \delta(m - m_i) \ , \tag{2.27}$$

where the sum runs over all known hadronic states with their respective spin degeneracies (g_i) up to mass M < 2 GeV. In the higher mass range, we include Hagedorn states with continuous, exponentially growing mass spectrum. This is followed by the hypothesis of Hagedorn, which explains the particle production rate quite successfully in high energy proton-proton collisions [39]. A recent study of HRG model which includes an exponential mass spectrum has shown remarkable good agreement with lattice for T< 155 MeV [40], thus supports the existence of such hadronic states. The density of Hagedorn states is taken as:

$$\rho_{\text{cont.}}(m) = A\,\frac{\exp(m/T_H)}{(m^2 + m_0^2)^{5/4}} \ , \tag{2.28}$$

where $A = 0.5$ GeV$^{3/2}$, $m_0 = 0.5$ GeV and m varies from 2 GeV to 12 GeV. $T_H =$ is known as the Hagedorn temperature, equals to 196 MeV. The parameters are adopted from [41], which discusses the importance of Hagedorn states for the rapid chemical equilibration of hadrons near the critical temperature T_c.

The underlying assumption of the HRG model is the equivalence of thermodynamic properties of an interacting gas of hadrons and a free gas of hadrons and it's resonances. This has been proven explicitly in [42], where the temperature variation of square of speed of sound (C_s^2) of an interacting gas of pions (π) is found to be very similar to a non-interacting gas of pion (π), kaon (K), eta (η), rho (ρ) and omega (ω) mesons.

Assuming all the species are in thermal and chemical equilibrium, the grand canonical partition function of a HRG can be written as a product of partition functions of all hadrons and the resonances.

$$\ln Z_{\text{HRG}}(\mu, V, T) = \sum_i \ln z_i(\mu_i, V, T) + \ln Z_{\text{HS}} \ , \tag{2.29}$$

where z_i is the partition function and μ_i is the chemical potential of the i^{th} hadron. The partition function of the discrete hadronic states;

$$\ln z_i(\mu_i, V, T) = \pm \frac{V g_i}{(2\pi)^3(\hbar)^3} \int dp 4\pi p^2 \ln[1 \pm \lambda_i exp(-\beta \epsilon_i)], \tag{2.30}$$

with (+) sign for fermions and (-) sign for bosons. The parameter $\lambda_i = exp(\mu_i/T)$ is called the fugacity and $\epsilon_i = \sqrt{p^2 + m_i^2}$ is the energy of the i^{th} hadron. $\beta = 1/T$ in the natural units.

For the continuous Hagedorn mass spectrum, the partition function is defined as;

$$\ln Z_{\text{HS}} = \int dm \rho_{cont.}(m) \ln z_{MS}(V, T, m) \ , \tag{2.31}$$

where z_{MS} stands for the grand canonical partition function of an ideal gas of mesons. Note that, we have assumed only mesonic Hagedorn states are produced with zero net strangeness.

Various thermodynamic quantities like; Pressure, Energy density, Number density are calculated from each partition function and add them to get the total Pressure, total Energy density and total number density of the system. Here we have listed the formulae for a particular hadronic species;

$$\text{Pressure :} \qquad P_i = \frac{g_i}{3(2\pi)^3(\hbar)^3} \int dp \frac{4\pi p^2 (\frac{p\partial\epsilon_i}{\partial p})}{exp[\beta(\epsilon_i - \mu_i)] \pm 1} \tag{2.32}$$

$$\text{Energy density}: \qquad e_i = \frac{g_i}{(2\pi)^3(\hbar)^3}\int dp \frac{4\pi p^2(\epsilon_i)}{exp[\beta(\epsilon_i-\mu_i)]\pm 1} \tag{2.33}$$

$$\text{Number density}: \qquad n_i = \frac{g_i}{(2\pi)^3(\hbar)^3}\int dp \frac{4\pi p^2}{exp[\beta(\epsilon_i-\mu_i)]\pm 1} \tag{2.34}$$

The entropy density(s) is calculated using the fundamental thermodynamic relation:

$$Ts_i = (e_i + P_i) - \mu n_i. \tag{2.35}$$

All the above mentioned quantities are derived for zero hadronic chemical potential in the present work.

Till now, we have assumed the hadrons are constituting an ensemble of ideal point-like particles. According to the MIT Bag model, each hadron occupies a finite volume which is proportional to their mass; $m/4B$ [43], where B is called the Bag constant. Thus the hadrons are impenetrable to each other and the repulsive interaction among the hadrons is implemented through the excluded volume correction of the above thermodynamic quantities. Several approaches are available in the literature to account for the effect [44, 45]. We have adopted the thermodynamically consistent formalism of Kapusta and Olive [46] in the present study. The excluded volume corrected (xv) quantities are related to same calculated for the point-particle (pt) as[1];

$$P_{\rm xv} = \frac{P_{\rm pt}(T^*)}{1-\frac{P_{\rm pt}(T^*)}{4B}}\ , \tag{2.36}$$

$$e_{\rm xv} = \frac{e_{\rm pt}(T^*)}{1+\frac{e_{\rm pt}(T^*)}{4B}}\ , \tag{2.37}$$

$$T_{\rm xv} = \frac{T^*}{1-\frac{P_{\rm pt}(T^*)}{4B}}\ , \tag{2.38}$$

$$s_{\rm xv} = \frac{s_{\rm pt}(T^*)}{1+\frac{e_{\rm pt}(T^*)}{4B}}\ , \tag{2.39}$$

where T^* is an arbitrary temperature for a system of point-like hadrons.The Bag constant is taken as $B^{1/4}$ =0.340 GeV [41]. We restrict the hadron resonance gas description up to $T \leq T_H$. For $T > T_H$, the system is more likely to be in deconfined state of quarks and gluons. Now, the four possible outcomes of the hadronic matter part of the EOS are listed below with increasing richness of description;

[1]See Appendix A

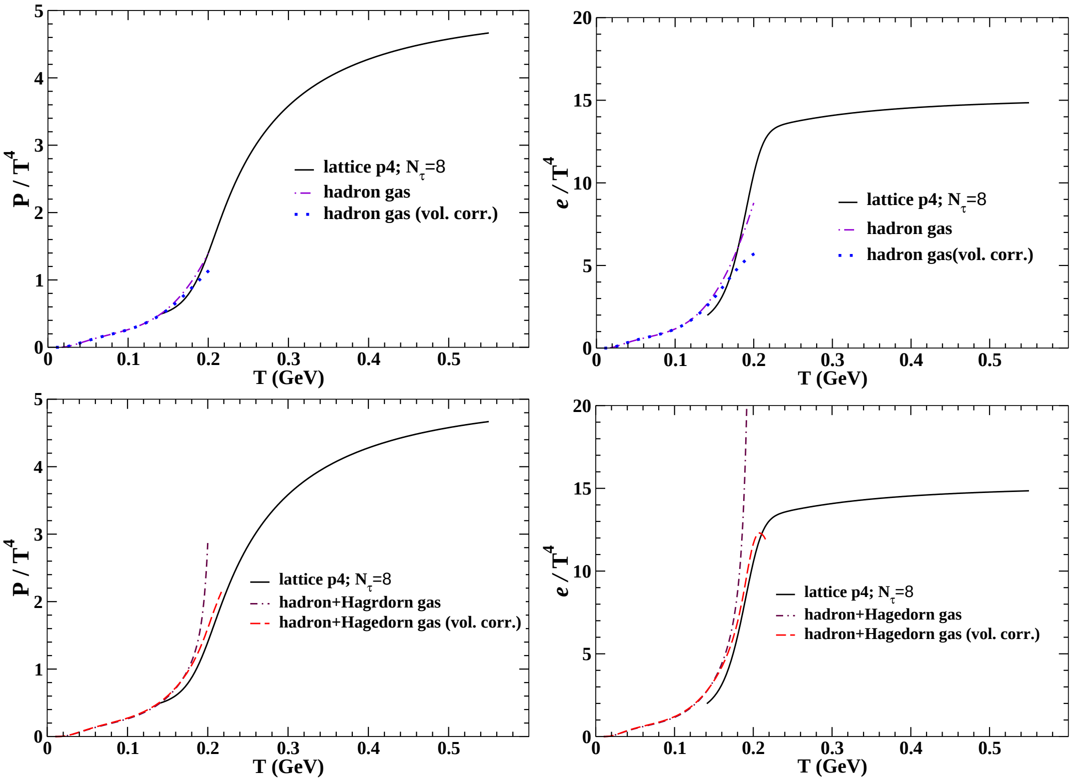

Figure 2.1: (Top) P/T^4, e/T^4 for hadron gas and volume corrected hadron gas; (Bottom) for hadron + Hagedorn gas and volume corrected hadron + Hagedorn gas, in comparison with the lattice QCD result.

- Hadron Gas.
- Vol. Corrected Hadron Gas.
- Hadron and Hagedorn Gas.
- Vol. Corrected Hadron and Hagedorn Gas.

We have calculated temperature weighted energy density (e/T^4), pressure (P/T^4) and entropy density (s/T^3) for each of the four scenarios.

2.2.2 Comparison with lattice QCD

Several QCD thermodynamic properties are derived through the lattice simulations, which is believed the first principle theory of QCD. The most convenient quantity calculable on lattice is the trace anomaly in the fourth power of temperature; $\Theta^{\mu\mu}(T)/T^4$.

This can also be expressed as temperature derivative of pressure,

$$\frac{\Theta^{\mu\mu}(T)}{T^4} \equiv \frac{e-3P}{T^4} = T\,\frac{\partial}{\partial T}(P/T^4). \tag{2.40}$$

The parameterized form of trace anomaly is taken from a recent lattice study [47] in 2+1 flavor QCD with almost physical quark masses (p4 action; N_τ=8). The parameterization is given up to T =539 MeV and it is arbitrarily extrapolated to higher temperatures for our calculation at the LHC energy. The pressure is obtained from Eq. 2.40 as:

$$\frac{P(T)}{T^4} - \frac{P(T_0)}{T_0^4} = \int_{T_0}^{T} dT' \frac{1}{T'^5}\Theta^{\mu\mu}(T'), \tag{2.41}$$

where T_0 is an arbitrary temperature, usually chosen low enough such that the pressure and other thermodynamic quantities have dominant contribution from pions. It has been found that the pressures for the four descriptions of the hadronic matter discussed above, are nearly identical at a temperature $\sim$140 MeV. Thus, for lattice calculations final values for the pressure are obtained by taking T_0 as 140 MeV, and adding the corresponding pressure from the hadronic matter. The energy density (e) and entropy density ($s = (e+P)/T$) are obtained by combining the result of P/T^4 and $(e-3P)/T^4$.

In Fig. 2.1, we have displayed the results of pressure and energy density for the four scenarios of the hadronic matter and compared with the similar quantities obtained from the lattice calculations in the temperature range; $T < 200$ MeV.

We find the pressure or energy density rises rapidly for ordinary hadron gas as temperature increases. Adding finite volume corrections arrests the rapid rise of the thermodynamic quantities. It is seen that the volume correction plays an important role beyond temperature 140 MeV (see Fig. 2.2). Inclusion of Hagedorn resonances predicts the shape similar to lattice results over a few bins of temperature but the energy density (or pressure) shoots up. This is because of higher mass hadronic states are more populated as the temperature approaches to the Hagedorn temperature, T_H. Finally switching on volume corrections for hadron + Hagedorn resonance gas brings in proximity with the lattice, both in shape and magnitude.

We have also calculated the square of speed of sound C_s^2 ($= \partial P/\partial e$) and the temperature variation of C_s^2 for the four scenarios are shown in Fig. 2.3 along with the lattice result. It is seen that the four descriptions exhibit identical variation of C_s^2 for $T <$140

MeV. Adding volume correction to the hadron gas causes sharp rise in C_s^2. The contribution of Hagedorn states are found to reduce the speed of sound. The possible reason is the following: as the temperature approaches closer to T_H, higher mass Hagedorn states are populated. The increase in energy density is expensed to form the higher mass resonances, thus reduces the pressure. Finally, the volume corrected hadron + Hagedorn gas has been found in good agreement with the lattice result over several bins of temperature.

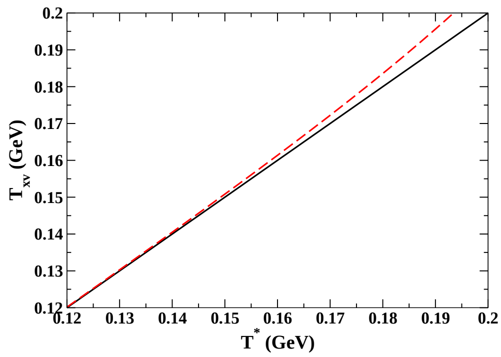

Figure 2.2: Variation of volume corrected temperature T_{xv} with true temperature T^*.

2.2.3 The HHB and HHL EOS

The above analyses conclude that the volume corrected hadron + Hagedorn gas is the best choice for the hadronic matter part of the EOS. Now for the quark matter part of the EOS, we have chosen either the Bag model equation of state [43] or the lattice equation of state [47]. In both cases, the transition temperature from hadronic matter to quark matter is chosen as 165 MeV. This is guided by the thermal model prediction of the chemical freeze out temperature at top RHIC energies [48] and similar temperature is expected at the top LHC energy [49].

The Bag model EOS consists of an ideal massless gas of u,d, s quarks and gluons. The pressure, energy density for an ideal gas of quarks and gluons at zero baryonic chemical potential are given by [32]:

$$P_{QGP} = gtot\frac{\pi^2}{90}T^4 - B$$
$$e_{QGP} = g_{tot}\frac{\pi^2}{90}T^4 + B, \tag{2.42}$$

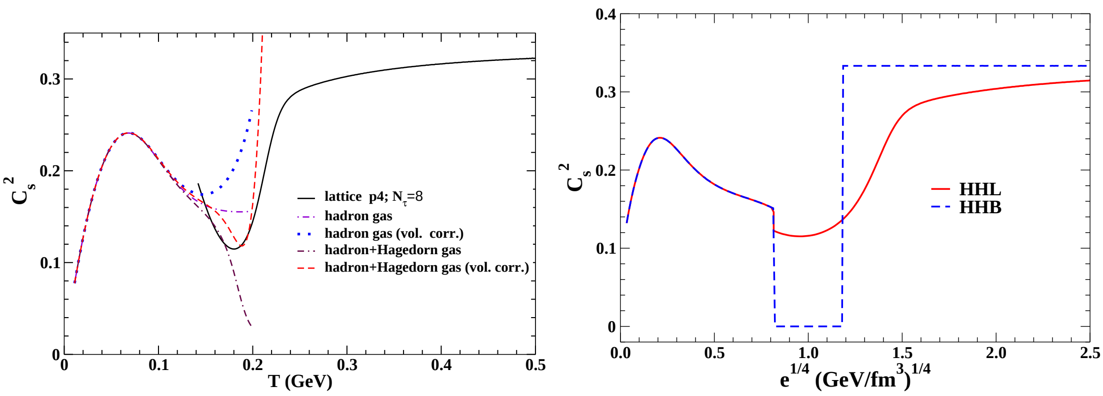

Figure 2.3: (Left) Square of speed of sound vs Temperature for the four scenarios of hadronic matter. (Right) Square of speed of sound for the HHB and HHL EOS, as a function of $e^{1/4}$

where $g_{tot} = [g_g + 7/8(g_q + g_{\bar{q}})]$ is the total degeneracy factor. The factor (7/8) appears due to the difference in the Bose and Fermi statistics in the Boltzmann factor. g_q, $g_{\bar{q}}$ and g_g are the respective degeneracies for quarks, anti-quarks and gluons.

$$g_q = g_{\bar{q}} = N_c N_s N_f, \tag{2.43}$$

with $N_c = 3$ (color), $N_f = 3$ (flavor) and $N_s = 2$ (spin).

Now there are 8 gluons with 2 degrees of polarisation; $g_g = 8 \times 2 = 16$. Thus the total degeneracy factor; $g_{tot} = 16 + 7/8(18 + 18) = 47.5$.

The appearance of negative Bag constant (B) in Eq. 2.42 signifies that the QGP formed in the laboratory is a finite system with boundary. We have varied the Bag constant B to match the pressure of both phases such that the constructed EOS admits a first order phase transition at critical temperature T_c= 165 MeV. This is called as the HHB (Hadron Hagedorn Bag) EOS of the strongly interacting matter.

Next we consider the realistic EOS which emulates the QCD interaction among the quarks and gluons on a lattice. We have followed the lattice result of 2+1 flavor QCD with almost physical quark masses [47] at zero baryonic chemical potential. The hadronic matter description is matched with the lattice EOS at a temperature 165 MeV. While the pressure, energy density varies smoothly near the point of transition, a little discontinuity($\sim$ 3%) has been found for the speed of sound. We believe the effect would be negligible on any physical observable. This is called the HHL (Hadron Hagedorn Lattice) EOS which includes a cross-over from quark matter to hadronic matter around the temperature 185 MeV.

The speed of sound (C_s^2), describes the rate of expansion at different phases of the system, for the two EOS is plotted against $e^{1/4}$ in Fig. 2.3. We find in the hadronic phase, both EOS shows similar variation in speed of sound. In the mixed phase region (0.4$\leq e \leq$ 2) GeV/fm^3; the speed of sound is zero for the HHB EOS whereas it never becomes zero for HHL EOS. Finally in the QGP phase ($e >$ 2 GeV/fm^3), the speed of sound approaches to a constant value (1/3) for the HHB EOS and remains larger than the HHL EOS. The differences in the speed of sound may lead to interesting effects in the final state which we will see in subsequent studies.

2.3 Hydrodynamic Evolution:

In order to distinguish between the two EOS, we considered the central collisions of gold (Au) nuclei at the top RHIC energy ($\sqrt{s_{\rm NN}}$ = 200 GeV) and lead (Pb) nuclei at the top LHC energy ($\sqrt{s_{\rm NN}}$ = 5.5 TeV).

We have assumed a cylindrical symmetry of the system and boost invariance in the longitudinal direction. Thus the fluid four-velocity (u^μ) has the form

$$\begin{aligned} u^\mu &= \gamma_r(\tau,r)(\frac{t}{\tau}, v_r, 0, \frac{z}{\tau}) \\ &= \gamma_r(\tau,r)(\cosh\eta, v_r, 0, \sinh\eta) \end{aligned} \qquad (2.44)$$

with $\gamma_r = 1/\sqrt{(1-v_r^2)}$ is the boost factor and r is the transverse distance from the collision axis. Since τ and r do not change under Lorentz boost; scalar quantities like energy density, temperature are function of τ and r and independent of η.

The hydrodynamic equations of motion (Eqs. 2.18, 2.19) are given by [50, 51]

$$\partial_\tau T^{00} + \frac{1}{r}\partial_r(rT^{01}) + \frac{1}{\tau}(T^{00}+P) = 0 \qquad (2.45)$$

and

$$\partial_\tau T^{01} + \frac{1}{r}\partial_r\left[r(T^{00}+P)v_r^2\right] + \frac{1}{\tau}T^{01} + \partial_r P = 0, \qquad (2.46)$$

where $T^{00} = (\epsilon+P)u^0u^0 - P$ and $T^{01} = (\epsilon+P)u^0u^1$.

The above equations can always be reduced to the form of continuity equation:

$$\partial_t\rho + \nabla(\rho v) = 0 \qquad (2.47)$$

The numerical schemes used to solve such type of differential equations are called flux correlated transport algorithm (FCT). We have followed a special kind of FCT called '*SHASTA*' (Sharp And Smooth Transport Algorithm), is invented by Boris and Book [52]. The special merit of this algorithm is that it can handle discontinuities which appears as rarefaction shock waves at the boundary of quark phase and hadronic phase [53].

2.3.1 Initial conditions and history of evolution

The thermalized state of matter namely, the quark-gluon plasma is assumed to be formed at some initial proper time τ_0 after the collision. Therefore to describe the time evolution of the matter, we need a value of initial energy density ($\epsilon(\tau_0)$) and radial velocity ($v_r(\tau_0)$). The initial transverse velocity is taken to be zero, $v_r(\tau_0) = 0$ [51, 54]. The energy density is contributed from both soft and hard processes in the collision. While the soft processes scales with density of wounded nucleons ($n_{wn}(r)$), the hard processes scales with number of binary collisions ($n_{BC}(r)$). $n_{wn}(r)$ and $n_{BC}(r)$ are obtained from the optical Glauber model [13, 32]. Thus the energy density at any point (r, τ) is given by:

$$\epsilon(r,\tau) = \langle \epsilon_0(0,\tau_0) \rangle \left[\alpha n_{wn}(r,\tau) + (1-\alpha) n_{BC}(r,\tau) \right], \tag{2.48}$$

where the α is the fraction of the soft processes. We find that α =0.75 gives reasonable description of the particle spectra at the RHIC energy [55], while at the LHC energy we expect soft fraction increases following the study of Kharzeev *et al.* [56] and mini-jet picture of parton production [57].

The average initial energy density and the initial proper time for hydrodynamic simulation are following:

$$\langle \epsilon_0(0,\tau_0) \rangle = \begin{cases} 80.8 \text{ GeV/fm}^3 & \tau_0 \ = \ 0.2\,\text{fm/c} \quad \text{RHIC}, \\ 718.3 \text{ GeV/fm}^3 & \tau_0 \ = \ 0.1\,\text{fm/c} \quad \text{LHC}. \end{cases} \tag{2.49}$$

Our choice of initial time (τ_0) is followed from the EKRT model [58] which combines perturbative QCD mini-jet production with gluon saturation to compute initial condition of hydrodynamics. Within the framework of EKRT, the initial time is inversely proportional to saturation momentum scale ($p_{sat.}$); $\tau_0 \sim 1/p_{sat.}$. The value of $p_{sat.}$ at

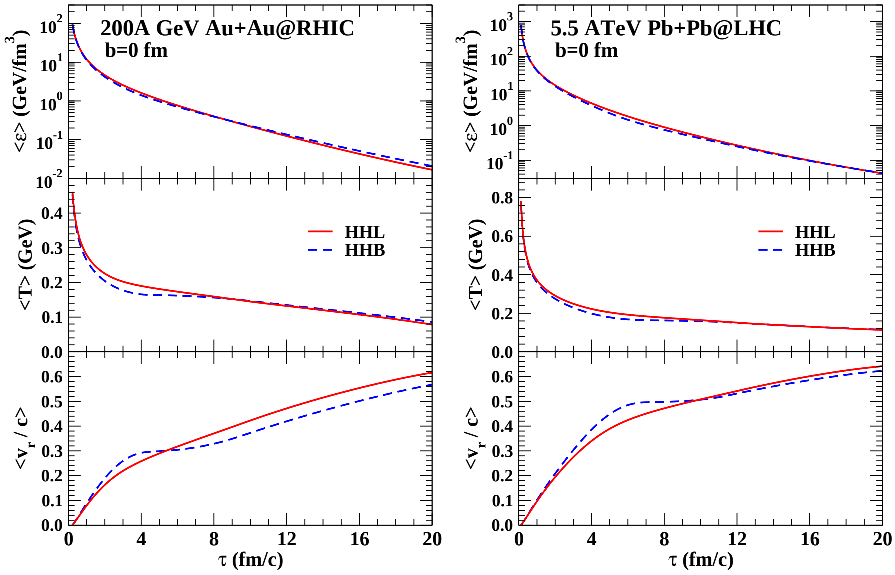

Figure 2.4: Time evolution of average energy density, Temperature and Radial velocity at the RHIC (left panel) and LHC (right panel) energy for the two EOS.

RHIC and LHC is taken as 1.16 and 2.03 GeV respectively [59]. It has been found that the set of initial parameters produces rapidity density of charged particles $dN_{\rm ch}/dy \approx$ 680 at RHIC and $dN_{\rm ch}/dy \approx 2040$ at LHC [60]. Our choice of initial time is little smaller than other works [55, 61] however if we consider larger formation time, the corresponding energy density would be reduced. The choice of small τ_0 facilitates us to derive a fraction of pre-equilibrium photons in the thermal photon spectrum.

For the HHB EOS, we approached the Maxwell construction of mixed phase as done in earlier works [50, 51]. Let us assume the energy density of the QGP phase at the critical temperature (T_c) is $\epsilon_q(T_c)$ and that for the hadronic phase is $\epsilon_h(T_c)$. Then the fraction β of the energy density contributed by QGP phase in mixed phase is give by:

$$\epsilon(\beta, T_c) = \beta\epsilon_q(T_c) + (1-\beta)\epsilon_h(T_c)\ . \tag{2.50}$$

In case of HHL EOS, we assume the quark-gluon plasma exists for $T \geq 185$ MeV [47] and below that the matter is in hadronic phase.

Next we calculate the time evolution of the internal variables of the system e.g, Energy density, Temperature, Radial velocity (v_r) for the two EOS at the RHIC and LHC energy. The quantities are averaged as;

$$\langle f \rangle = \frac{\int 2\pi\, r\, dr\, f(r,\tau)\, \epsilon(r,\tau)}{\int 2\pi\, r\, dr\, \epsilon(r,\tau)}\ . \tag{2.51}$$

The results are shown in Fig. 2.4. We see the variation of $\langle\epsilon\rangle$ with time (τ) is quite similar for the two equations of state at RHIC and LHC both. The time variation of $\langle T\rangle$ shows difference. There is a plateau like region for $4 < \tau < 8$ fm/c in case of HHB EOS, as bulk of the system resides in mixed phase. However for HHL EOS the temperature is continuously decreasing. The plateau region is little larger at LHC as the system life time is longer.

The more interesting result awaits in the temporal evolution of average radial velocity $\langle v_r\rangle$ for the two EOS. Initially the radial velocity grows faster for the HHB EOS because of large speed of sound in the QGP phase (see Fig. 2.3). Once the system enters into the mixed phase, the radial velocity becomes constant. It rises again after elapsing the phase. The radial velocity for HHL EOS is continuously growing, initially smaller but overshoots the former during the mixed phase. This will give rise to larger radial velocity at the final hadronic phase. We shall see the effect in the momentum spectrum of particles.

2.3.2 Kinetic freeze out and particle production

As discussed earlier, the kinetic freeze out takes place at the end of the hydrodynamic evolution when the microscopic collision rate becomes smaller than the expansion rate of the system. The transition from the fluid dynamical description to freely streaming particle description is achieved by Cooper-Frye formula [18]. According to this formula, one runs the hydrodynamic simulation up to large time and determine the four dimensional freeze out hyper-surface (Σ^μ) of constant temperature. The fluid cells along this hyper-surface should pass the prerequisite freeze out criterion. We consider the kinetic freeze out takes place at $T = 100$ MeV both at RHIC and LHC. This is inspired from various thermal model predictions at low μ_B of the phase diagram [62].

The invariant momentum distribution of i'th type of particles are given by[2]:

$$\begin{aligned} E\frac{dN_i}{d^3p} = \frac{dN}{2\pi p_T dp_T dy d\phi} &= \int_\Sigma f(x,p,t)p_\mu d\sigma^\mu \\ &= \frac{g_i}{(2\pi)^3}\int_\Sigma \frac{p_\mu d\sigma^\mu}{\exp[(E^* - \mu(x))/T_f(x)] \pm 1}, \end{aligned} \tag{2.52}$$

where $E^* = p_\mu u^\mu$ is the energy of the particle in a global frame. $\mu(x)$ and $T_f(x)$ are

[2]See Appendix B for details

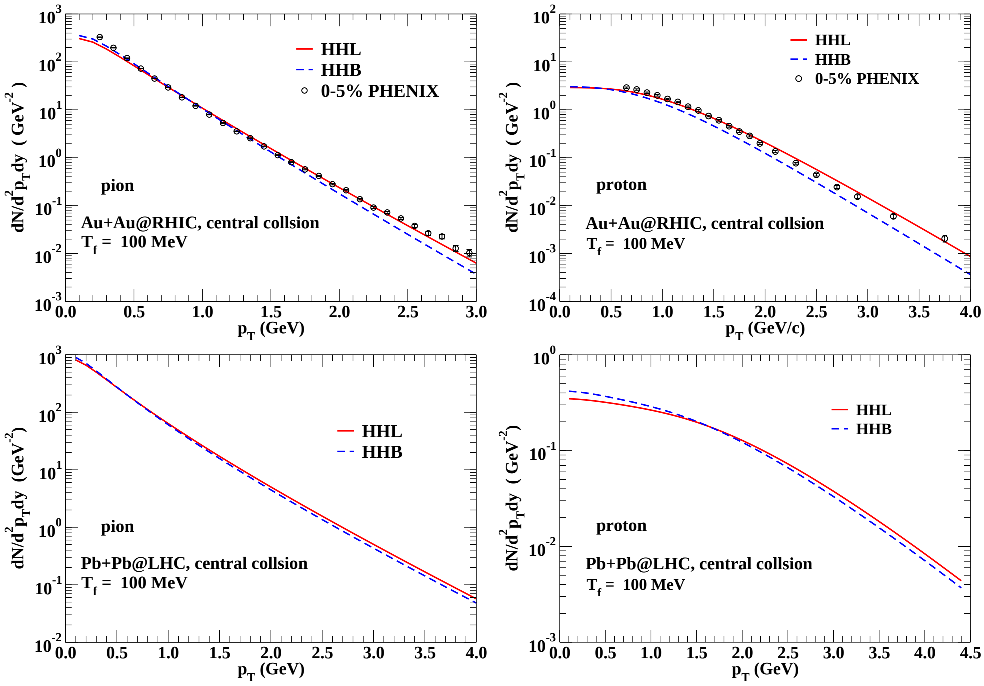

Figure 2.5: (Upper panel) The thermal pion and proton transverse momentum spectra at the RHIC energy for HHB and HHL EOS. The data points are taken from PHENIX collaboration [63]. (Lower panel) The same at the top LHC energy.

the local chemical potential and temperature along the freeze out surface Σ^μ. They are computed from the hydrodynamic output, along with input from the equation of state. This formalism is used to calculate momentum distribution of all directly emitted hadrons of all masses.

In Fig. 2.5, we have shown the transverse momentum spectra of thermal pions and protons for the central collisions of Au nuclei at mid-rapidity (y =0) at RHIC energy for the two EOS. The experimental data for transverse momentum distribution of pions and protons [63] for $0-5\%$ most central collisions are also given for comparison. We note that both the EOS, HHB and HHL, gives a good description of the data up to p_T= 2 GeV. However to inspect more closely, we have shown the ratio of thermal pion yields for the two EOS in Fig. 2.6. It can be seen that the deviation of HHL from HHB is about 25% at p_T= 2 GeV. The resonance decay contribution is not considered in the present study. However it will improve the yield at lower p_T [64] where difference between the two EOS is merely seen. In addition, the inverse slope of the spectra for the HHL EOS is found to be larger than the same for the HHB EOS.

The inverse slope of the momentum spectra (Eq.2.52) can be expressed as; $T_f = T_{av} + mv_r^2$ for hadrons of mass m [55]. We feel the difference is originated due to the variation in radial velocity (Fig. 2.4). If the system follows HHB EOS, the acceleration of the system stops during the mixed phase gives rise to smaller radial velocity at the time of freeze out compared to the lattice EOS.

The corresponding results for the central collision of Pb nuclei at the top LHC energy are shown in Fig. 2.5 While the earlier observations remain true we find that the difference between the momentum spectra for the two EOS is further reduced. This is due to the large life time of the system produced at LHC.

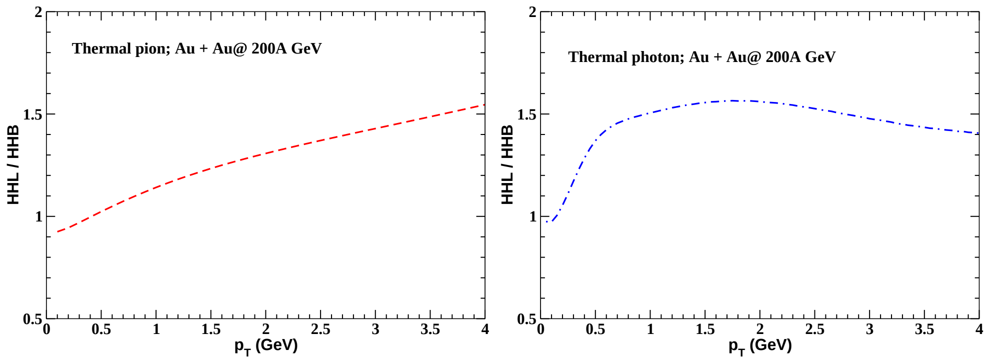

Figure 2.6: Ratio of thermal pion (Left) and thermal photon (Right) production for the two EOS, HHL and HHB, for Au+Au collisions at the RHIC energy is plotted against the transverse momentum of pion and photon.

2.3.3 Thermal photon production

The invariant yield of thermal photons is obtained by integrating the emission rate of photons from QGP and hadronic phase over the space-time volume of the system. The main channels of photon production in an equilibrated quark matter up to leading-order of strong coupling (α_s) are i) quark-gluon Compton scattering and ii) quark-anti-quark annihilation. Also there are inelastic processes of photon production like Bremsstrahlung radiation and pair annihilation. They contribute to the same $2 \rightarrow 2$ order because of the presence of near-collinear singularity [65]. We have used the thermal photon emission rate in QGP by Arnold *et al.* [65] which includes all the above processes at zero μ_B and taking into account the Landau-Pomeranchuk-Midgal (LPM) effect while computing inelastic processes.

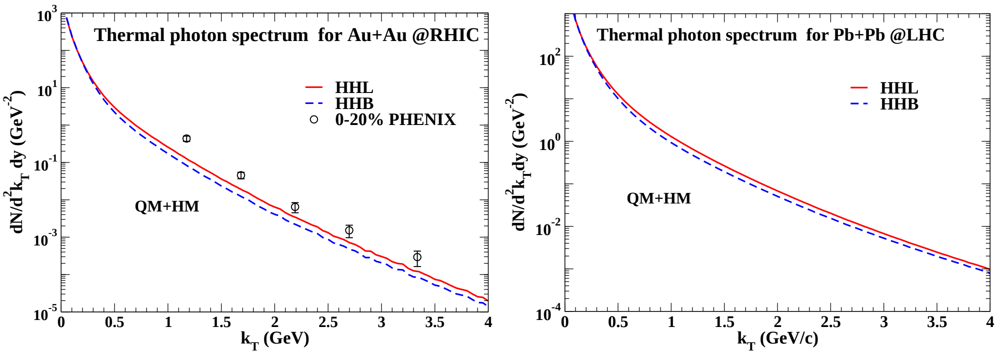

Figure 2.7: Thermal photon transverse momentum spectra at the RHIC and LHC energy for the two equations of state. The photon data at RHIC for 0-20% centrality bin are adopted from [68].

The photons emitted from strongly interacting, hot hadronic matter populate the thermal photon spectrum at lower p_T. The hadronic matter is considered as an ensemble of interacting mesons. The most important hadronic channels of photon production are i) $\pi\rho \rightarrow \pi\gamma$ ii) $\pi\pi \rightarrow \rho\gamma$. We have used the photon emission rate from Turbide *et al.* [66] which includes additional strange meson channels in the calculation e.g., $(\pi K^* \rightarrow K\gamma)$, $(KK^* \rightarrow \pi\gamma)$ and reactions with exchange of heavy mesons as ω (782 MeV). It has also taken into account Dalitz decays like; $\rho \rightarrow \pi\pi\gamma$.

Using these rates we have calculated the transverse momentum spectra of thermal photons for the central collisions of Au (Pb) nuclei at the RHIC (LHC) energy for the two EOS. We have checked the slope of the thermal photon spectrum is close to earlier work [67] at the RHIC energy. The results are shown in Fig. 2.7 along with the direct photon data of 0-20% centrality bin from the PHENIX collaboration [68]. However in order to compare with experimental data one would need to add the prompt photon contribution. Similar to hadron spectra described earlier, we find the thermal photon spectra for the two EOS are very close and the inverse slope of the spectra is found larger in case of lattice based EOS. We have also shown the ratio of thermal photon yields for the two EOS (see Fig. 2.6).

2.3.4 Spatial and temporal evolution of photon source

The observations suggest that the thermal particle and photon momentum spectra are not able to distinguish between the two EOS, one admitting a first order phase transition, and the other admitting a sharp cross-over as suggested by lattice QCD calculations.

This raises the question, is there any possible way to distinguish between the two scenarios? We are curious in the study because it encloses the two widest possibilities of EOS of the matter created in relativistic heavy ion collisions. We recall that the history of evolution of average energy density and radial velocity have shown some noticeable differences. This fact instigates us to calculate two photon intensity interferometry which provides "live coverage"of the space-time development of source [69].

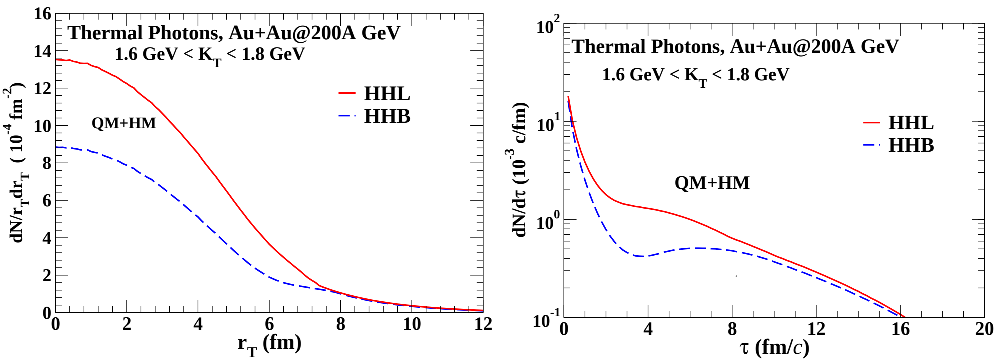

Figure 2.8: The radial and temporal dependence of the photon emitting source at the RHIC energy for the HHB and HHL EOS.

Therefore we have plotted the spatial and temporal distribution of the photon emitting source for a typical photon momentum ≈ 1.7 GeV for the two equations of state at RHIC (Fig. 2.8). We find the production of photons is larger for the HHL EOS at small radial distances as well as intermediate time (during the mixed phase). Now photons originated from quark matter at earlier times and from hadronic matter at later times and the interference depends on the relative contribution of both [70]. As the space-time structure of the two sources are quite distinct, we hope that the interferometry of thermal photons may resolve the issue. The next section discusses the two photon intensity interferometry (or the momentum correlation) in great details.

Chapter 3

Intensity interferometry for the two EOS

3.1 The formalism of interferometry

The idea of two-particle intensity interferometry was first proposed by the British scientists Hanbury Brown and Twiss in 1950s [73], to measure the angular size of the astronomical objects. A similar treatment applied independently by Goldhaber *et al.* [74] in 1960, to measure the spatial size of the interaction zone in proton-antiproton annihilation, exploiting the Bose-Einstein correlation of two pions. This sometimes called as second order interference because it compares intensities at the point of superposition rather than amplitudes as it was in case of first order interference. In the next two subsections, we have discussed the salient features of first order and second order interference following the literature reported in Ref. [75].

3.1.1 First order interference

We consider a general Young slit experiment where we have N-slits on a screen (D_1) at $r_1, r_2, ..., r_N$, is illuminated by a point source S. The detector is placed on a second screen (D_2) at R to observe the interference pattern due to the superposition of waves coming from N-slits. As the waves are coming from a single source, there is a constant phase relation between them. The distance between the slits is considered to be much smaller than the distance between the screens; $|r_i - r_j| \ll d$ [75].

The resultant wave function Φ measured at R arises from the coherent superposition

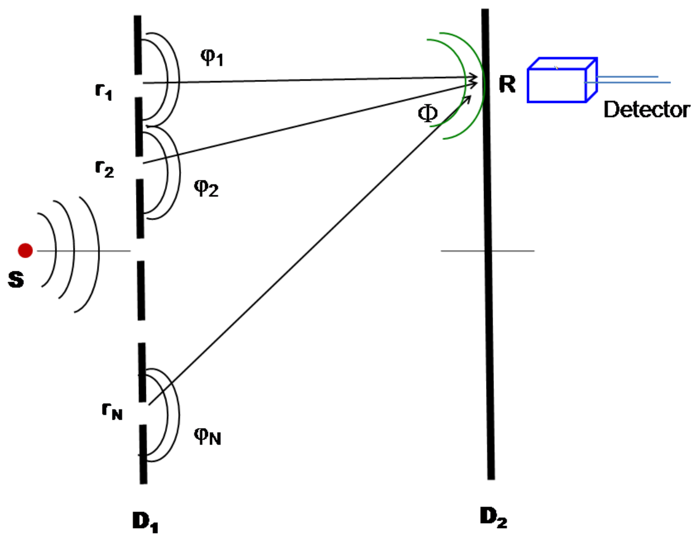

Figure 3.1: A schematic arrangement of first-order interference in optics.

of N wave functions ϕ_i emitted from r_i:

$$\phi_i = exp\{-ik \cdot (r_i - R)\} \quad \text{and} \quad \Phi = \sum_{i=1}^{N} \phi_i \chi_i, \tag{3.1}$$

where χ_i represents the phase at each point. We define the first order correlation function $C_1(R)$ as the ratio of total measured intensity at R ($I_1(R)$) and the product of partial intensities ($I_i(R)$) at R.

$$C_1(R) = \frac{I(R)}{[\prod_{i=1}^{N} I_1(R) I_2(R) \ldots . I_N(R)]} \tag{3.2}$$

This can also be written in terms of the amplitude of the wave functions and averaged over the measurement time,

$$C_1(R) = \frac{\langle |\Phi|^2 \rangle}{(\prod_{i=1}^{N} \langle |\phi_i \chi_i|^2 \rangle \ldots . \langle |\phi_N \chi_N|^2 \rangle)^{1/N}} = \langle |\Phi|^2 \rangle \tag{3.3}$$

where each factor in the denominator time averages to one. Thus the first order correlation function is directly proportional to $|\Phi|^2$.

$$\begin{aligned} |\Phi|^2 &= \left\{ \sum_{i=1}^{N} \phi_i \chi_i \right\} \left\{ \sum_{j=1}^{N} \phi_j^* \chi_j^* \right\} \\ &= N + \left\{ \sum_{i,j=1,\, j>i}^{N} l_{ij} + \sum_{i,j=1,\, j>i}^{N} l_{ij}^* \right\} \end{aligned} \tag{3.4}$$

$l_{ij} = \phi_i \phi_j^* \chi_i \chi_j^*$ is the complex amplitude. As the phase difference between the waves will be constant in time; $\langle|\chi_i \chi_j^*|\rangle$=1 for all i, j. The time average of the square amplitude becomes

$$\langle|\Phi|^2\rangle = N + \sum_{i,j=1,\, j\neq i} (\phi_i \phi_j^*) = N + \sum_{i,j=1,\, j\neq i} exp\{-ik \cdot (r_i - r_j)\} \tag{3.5}$$

Collecting the exponential terms pair-wise, we write the first order correlation function:

$$C_1(R) = N + 2 \sum_{i,j=1,\, j>i}^{N} cos\{k \cdot (r_i - r_j)\} \tag{3.6}$$

The R dependence of the correlation function $C_1(R)$ comes through the angle between k and the distance $(r_i - r_j)$ of two slits. It is also related to the Fourier transform of the slit distribution on D_1. Thus one can get information about the spatial distribution of the secondary sources from the first order correlation function.

Now the argument of the cosine term in Eq. (3.6) can be expressed in terms of path difference between each slit and the detector:

$$k(y_i - y_j). \tag{3.7}$$

This also further can be reduced in terms of angular radius of the slits (θ_{ij}) viewed from the screen (D_2) and the distance of the detector (L) from the center of D_2,

$$k\theta_{ij} L. \tag{3.8}$$

Thus, for a given momentum k, the angular size of the light emitting source can be obtained from the shape of the correlation function. This is the basic principle of Michelson-type interferometer, used for astronomical purposes. The resolution of such apparatus is $\sim \lambda/L$, where λ is the wavelength. Now in order to improve the resolution either λ has to be decreased or L has to be increased. But the intensity of the distant objects decrease with increasing λ. Then remaining possibility is to increase the base line L of the interferometer. *The challenge is to keep the phase difference constant over long distances.* This severely limits the applicability of first order interferometry to determine the size of distant stars.

3.1.2 Second order interference

In order to circumvent this problem, Hanbury Brown and Twiss proposes a new technique which is based on the principle of intensity interference. Here the superposition of waves is considered to be *incoherent* which distinguishes it from the first order interference [75]. Some times this also referred as HBT interferometry; named after the scientists.

This is achieved in the previous Young's slit experiment if we replace the single point source S by N-independent point sources. Thus there will be no constant phase relation between the superposing waves. The relative phases ($|\chi_i\chi_j^*|$) at the point of superposition (R) fluctuates randomly much faster than the measurement time, so time average gives this zero: $\langle|\chi_i\chi_j^*|\rangle = 0$. Therefore, the second term of Eq. 3.4 contributes zero and the first order correlation function becomes constant.

$$\begin{aligned} |\Phi|^2 &= N \\ \Rightarrow C_1(R) &= N = \text{Constant} \end{aligned} \tag{3.9}$$

We find an uniform illumination of the screen (D_2). Now we add another detector at R' in coincidence with the first one at R. The second order correlation function is defined as the measured intensity at (R, R') in coincidence divided by the intensity measured at each detector individually:

$$C_{12}(R, R') = \frac{I(R, R')}{I(R)I(R')}. \tag{3.10}$$

In terms of amplitude of resultant wave functions at R and R':

$$C_{12}(R, R') = \frac{\langle|\Phi|^2|\Phi'|^2\rangle}{\langle|\Phi|^2\rangle\langle|\Phi'|^2\rangle}, \tag{3.11}$$

where $|\Phi|^2$ and $|\Phi'|^2$ are the intensities detected at R and R'. Since there are two detectors, we have two wave functions $\phi_i = exp\{-ik_1 \cdot (r_i - R)\}$ and $\phi_i' = exp\{-ik_2 \cdot (r_i - R')\}$ associated with each slit with momentum k_1 and k_2.

$$\Phi = \sum_{i=1}^{N} \phi_i\chi_i \quad \text{and} \quad \Phi' = \sum_{k=1}^{N} \phi_k'\chi_k' \tag{3.12}$$

As the superposition of waves is incoherent, from Eq. 3.9 we get $|\Phi|^2 = |\Phi'|^2 = N$. Thus the second order correlation function follows from Eq. 3.11:

$$C_{12}(R, R') = \frac{\langle|\Phi|^2|\Phi'|^2\rangle}{N^2}. \tag{3.13}$$

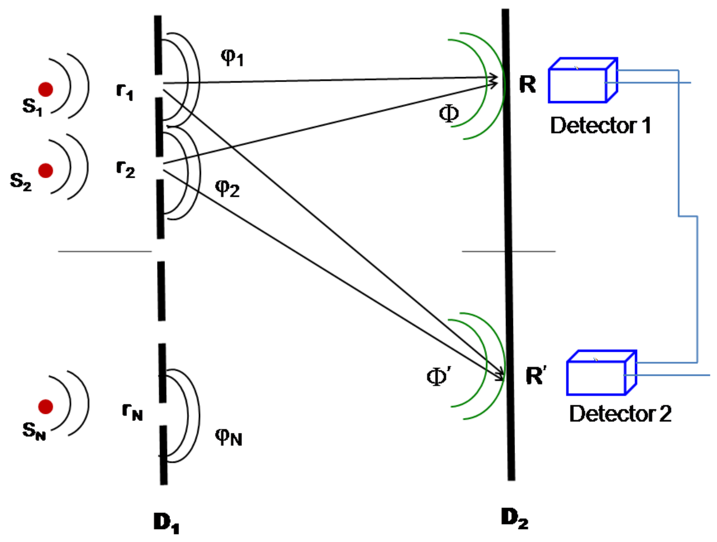

Figure 3.2: A schematic arrangement of second order interference in optics.

Using Eq. 3.4, we write the correlated amplitude as:

$$
\begin{aligned}
|\Phi|^2|\Phi'|^2 &= \left[N + \left(\sum_{i,j=1,\, j>i}^{N} l_{ij} + \sum_{i,j=1,\, j>i}^{N} l_{ij}^*\right)\right] \\
&\times \left[N + \left(\sum_{k,m=1,\, m>k}^{N} l_{km} + \sum_{k,m=1,\, m>k}^{N} l_{km}^*\right)\right] \qquad (3.14)
\end{aligned}
$$

We only write those terms for which relative phases cancel. The rest terms are time averaged to zero.

$$
\begin{aligned}
|\Phi|^2|\Phi'|^2 &= N^2 + \left(\sum_{i,j=1,\, j>i}^{N} l_{ij} \sum_{k,m=1,\, m>k}^{N} l_{km}^*\right) \\
&+ \left(\sum_{i,j=1,\, j>i}^{N} l_{ij}^* \sum_{k,m=1,\, m>k}^{N} l_{km}\right) \qquad (3.15)
\end{aligned}
$$

Thus we get,

$$
\begin{aligned}
\langle|\Phi|^2|\Phi'|^2\rangle &= N^2 + \left\{\sum_{i,j=1,\, j>i}^{N} (\phi_i\phi_j^*\phi_i^{*\prime}\phi_j') + \sum_{i,j=1,\, j>i}^{N} (\phi_i^*\phi_j\phi_i'\phi_j^{*\prime})\right\} \\
&= N^2 + \sum_{i,j=1,\, i\neq j}^{N} (\phi_i\phi_j^*\phi_i^{*\prime}\phi_j') \\
&= N^2 + \sum_{i,j=1,\, i\neq j}^{N} exp\{iq.(r_i - r_j)\}, \qquad (3.16)
\end{aligned}
$$

where q is the relative momentum difference $k_1 - k_2$. Grouping the exponential terms pair-wise, finally we get the second order correlation function from Eq. 3.13:

$$C_{12}(q) = 1 + \frac{2}{N^2} \sum_{i,j=1,\, j>i} cos\{q \cdot (r_i - r_j)\}. \tag{3.17}$$

The dependence of R, R' in the correlation function comes through the relative angle between k_1 and k_2. Now if we consider $k_1 \approx k_2 = k$, the argument of the cosine function in Eq. 3.17 becomes

$$k\theta_{ij}L. \tag{3.18}$$

and the second order correlation function writes as:

$$C_{12}(L) = 1 + \frac{2}{N^2} \sum_{i,j=1,\, j>i} cos\{k\theta_{ij}L\}. \tag{3.19}$$

Like the first order correlation function, angular size of an distant object for a given momentum k can be determined from the shape of the second order correlation function. The resolution of the interferometer based on the above principle is still given by λ/L. *But the condition of keeping constant phase is now relaxed.* So the base length L of the interferometer could be extended arbitrarily large values for small wavelength measurement [73].

▲Quantum stastistical interpretation

An alternative description of the second order correlation function can be arrived from the quantum statistics. Since the detected particles are indistinguishable, one should symmetrize (bosons) or anti-symmetrize (fermions) the two-particle wave function. For bosons, we find an enhancement for small momentum difference (i.e. the particles are produced close in phase space).

Let us consider f_{ij} is the production amplitude of a particle produced at r_i with momentum k_j. Now the joint probability of detecting two particles of momentum k_1 and k_2 in coincidence, is given by

$$P(k_1, k_2) = \left\langle | \sum_{i,j=1,\, j>i} (f_{1i}f_{2j} \pm f_{1j}f_{2i})|^2 \right\rangle, \tag{3.20}$$

where the first part represents contribution of particles with momentum k_1 produced r_i and momentum k_2 produced at r_j. The second part arises due to symmetrization

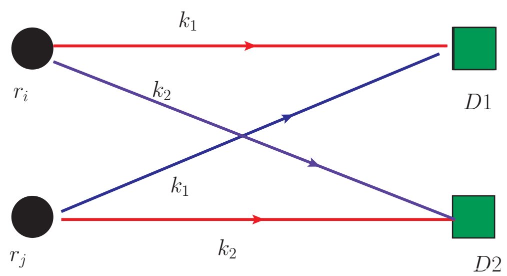

Figure 3.3: Schematic view of second order interference.

(+) or anti-symmetrization (−) of the wave function. Here we neglects all point-like contributions where both particles are produced at the same point.

Thus we write the second order correlation function as the ratio of joint probability of detecting two particles with momenta k_1, k_2 and the product of individual probabilities of detection:

$$\begin{aligned} C_{12}(k_1, k_2) &= \frac{P(k_1, k_2)}{P(k_1)P(k_2)} \\ &= \frac{\left\langle | \sum_{i,j=1\, j>i}^{N} (f_{1i} f_{2j} \pm f_{1j} f_{2i})|^2 \right\rangle}{\langle | \sum_i^N f_{1i}|^2 \rangle \langle | \sum_j^N f_{2j}|^2 \rangle} \end{aligned} \tag{3.21}$$

3.2 Intensity interferometry in heavy ion collisions

As discussed in the previous chapter, the matter created in relativistic heavy ion collisions is continuously evolving in space-time. The method of HBT interferometry has been extensively used during the past decades to extract the dynamical information about the system. Now we shall discuss the fundamental differences in the methodology of HBT interferometry, used for astronomy and nuclear physics:

- In astronomical purposes, the emission points of a stellar object are far apart ($\sim$ thousands of kilometer) compared to the distance between the detectors on the earth surface ($\sim$ hundreds of meter). The size to distance ratio is about 10^4. In nuclear physics, the emission points are much closely spaced ($\sim$ few Fermi) than the separation between the detectors ($\sim$ few centimeter) at the laboratory. Here the size to distance ratio is about 10^{-14}.

- The emission points on a star are considered to be static which is not valid in case of dynamical system produced in heavy ion collisions. Therefore we need to include explicit time dependence in the formalism. Thus the vectors $(\mathbf{k_i}, \mathbf{r_i})$ are replaced by the four-vectors $r_i = (t_i, \mathbf{r_i})$ and $k_i = (E_i, \mathbf{k_i})$. The N static emission points are now replaced by N particle production currents; $j(r_i)$. The production amplitude of one particle at r_i with four-momentum k_j is given by; $f_{ij} = j(k_j)exp(ik_j \cdot r_i)$, where $j(k_j)$ is the Fourier transform of $j(r_i)$.

The definition of two-particle correlation function in heavy ion collisions is followed from Eq. 3.21, where the numerator is given by the Lorentz invariant two particle coincidence momentum spectrum and the denominator is given by the product of single particle momentum distributions:

$$C(\mathbf{k_1}, \mathbf{k_2}) = \left[E_1 E_2 \frac{dN}{d^3\mathbf{k_1} d^3\mathbf{k_2}}\right] / \left[E_1 \frac{dN}{d^3\mathbf{k_1}}\, E_2 \frac{dN}{d^3\mathbf{k_2}}\right] , \tag{3.22}$$

There are several ways discussed in the literature to build a connection between the particle distribution in momentum space and source distribution in coordinate space. We follow the treatment of Ref. [76] in which the source is considered as an ensemble of elementary classical currents $J_\mu(r)$. Thus for incoherent emission of particles, the above equation can be written as,

$$C(\mathbf{q}, \mathbf{K}) = 1 \pm \frac{\left|\int d^4x\, S(x, \mathbf{K}) e^{ix\cdot q}\right|^2}{\int d^4x\, S(x, \mathbf{k_1}) \int d^4x\, S(x, \mathbf{k_2})} , \tag{3.23}$$

where the $(+)$ for bosons and $(-)$ for fermions. $\mathbf{K} = (\mathbf{k_1} + \mathbf{k_2})/2$ is the average momentum vector and $\mathbf{q} = \mathbf{k_1} - \mathbf{k_2}$ is the difference in momentum between the two particles. The space-time emission function $S(x, \mathbf{k})$ is approximated as the rate of particle production per unit four volume, $EdN/d^3\mathbf{k}d^4x$.

3.2.1 Parameterization of the correlation function

The two particle intensity correlation function is often approximated as a gaussian in terms of suitable momentum coordinates. The average transverse momentum of the pair is defined; $\mathbf{K_T} = (\mathbf{k_{1T}} + \mathbf{k_{2T}})/2$ and the difference in the transverse momentum of the pair is given by $\mathbf{q_T} = (\mathbf{k_{1T}} - \mathbf{k_{2T}})$. We have followed the '$\boldsymbol{osl}$'system of coordinates [71, 72], where 'l'stands for the longitudinal direction along the beam axis, 'o'stands for the outward direction parallel to $\mathbf{K_T}$ and the remaining Cartesian direction referred as sideward direction denoted by 's'. This is also referred as, Pratt-Bertsch parameterization of the correlation function.

We can write the four-momentum (k_i^μ) of the ith particle;

$$k_i^\mu = (k_{iT} \cosh\, y_i, k_{iT} \cos\psi_i, k_{iT}\sin\psi_i, k_{iT} \sinh\, y_i), \tag{3.24}$$

where k_T is the transverse momentum, y is the rapidity and ψ is the azimuthal angle of the particle.

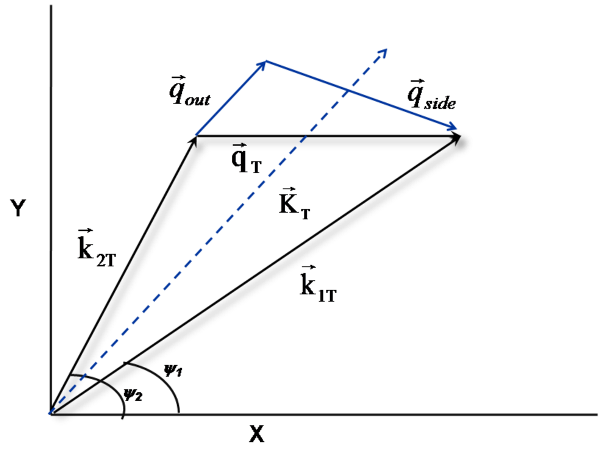

Figure 3.4: Geometrical interpretation of outward (q_o) and side-ward (q_s) momentum differences.

In terms of these variables, the longitudinal (q_l), outward (q_o), and side-ward momentum (q_s) differences are obtained as [77]:

$$\begin{aligned} q_l &= k_{1z} - k_{2z} \\ &= k_{1T}\sinh y_1 - k_{2T}\sinh y_2\ , \end{aligned} \tag{3.25}$$

$$\begin{aligned} q_o &= \frac{\mathbf{q_T}\cdot\mathbf{K_T}}{K_T} \\ &= \frac{(k_{1T}^2 - k_{2T}^2)}{\sqrt{k_{1T}^2 + k_{2T}^2 + 2k_{1T}k_{2T}\cos(\psi_1 - \psi_2)}}\ , \end{aligned} \tag{3.26}$$

$$\begin{aligned} q_s &= \left|\mathbf{q_T} - q_o\frac{\mathbf{K_T}}{K_T}\right| \\ &= \frac{2k_{1T}k_{2T}\sqrt{1-\cos^2(\psi_1 - \psi_2)}}{\sqrt{k_{1T}^2 + k_{2T}^2 + 2k_{1T}k_{2T}\cos(\psi_1 - \psi_2)}}\ . \end{aligned} \tag{3.27}$$

The correlation function $C(\mathbf{q},\mathbf{K})$ is often parameterized in terms of the outward, side-ward and longitudinal momentum differences:

$$C(\mathbf{q},\mathbf{K}) = 1 \pm exp\left(-\sum_{i,j=o,s,l} R_{ij}^2(\mathbf{K})q_iq_j\right)\ . \tag{3.28}$$

This can be understood from the fact that the correlation function is the Fourier transform of the source distribution. If the source distribution has Gaussian shape in coordinate space, the correlation function would also be Gaussian in the momentum space.

♠Interpretation of HBT radius parameters

The width of the correlation function $R_{ij}(\mathbf{K})$ is called the HBT radius parameter, characterizes the space-time dimension of the source [78, 79] along different directions.

$$R_{ij}^2(\mathbf{K}) = \langle (x_i' - \beta_i t')(x_j' - \beta_i t')\rangle \tag{3.29}$$

x', t' are the rms variances of the source in space and time. β_i is the projection of pair velocity $\beta(= \mathbf{K}/E)$ along the direction i. Only six R^2 parameters can be measured from the correlation function.

Now for an azimuthally symmetric system, the source has reflection symmetry $x_s \rightarrow -x_s$. The correlation function is symmetric under the transformation $q_s \rightarrow -q_s$; which yields $R_{os}^2 = R_{sl}^2 = 0$ [80]. The Eq. 3.28 becomes:

$$C(\mathbf{q}, \mathbf{K}) = 1 \pm exp\{-q_o^2 R_o^2 - q_s^2 R_s^2 - q_l^2 R_l^2 - 2q_o q_l R_{ol}^2\}, \tag{3.30}$$

where the R_o,R_s and R_l are the Fourier transformed radii corresponding to momentum differences q_o, q_s and q_l respectively. The cross-term R_{ol} was first proposed in Ref. [78]. This term vanishes if the source possesses longitudinal symmetry under $x_l \rightarrow -x_l$. Under the Gaussian approximation, the radii are given by:

$$\begin{aligned}
R_s^2 &= \langle x_s'^2 \rangle = \langle y^2 \rangle - (\langle y \rangle)^2, \\
R_o^2 &= \langle (x_o' - \beta_o t')^2 \rangle = \langle (x - \beta_o t')^2 \rangle - \langle x - \beta_o t' \rangle^2, \\
R_l^2 &= \langle (x_l' - \beta_l t')^2 \rangle = \langle (z - \beta_l t')^2 \rangle - \langle z - \beta_l t' \rangle^2, \\
R_{ol}^2 &= \langle (x_o' - \beta_o t')(x_l' - \beta_l t') \rangle = \langle (x - \beta_o t')(z - \beta_l t') \rangle - \langle x - \beta_o t' \rangle \langle z - \beta_l t' \rangle
\end{aligned} \tag{3.31}$$

We have chosen the longitudinal direction along $\hat{z}$, sideward direction along $\hat{y}$ and outward direction along $\hat{x}$. For a static source, the HBT radii are corresponding to the geometric size of the source along different directions. However for an expanding source, the measured HBT parameters do not reflect the actual size of the source [81, 82]. Thus R_s probes only the spatial structure whereas R_o probes both temporal and spatial structure of the source. The ratio of R_o/R_s referred as the time duration of particle

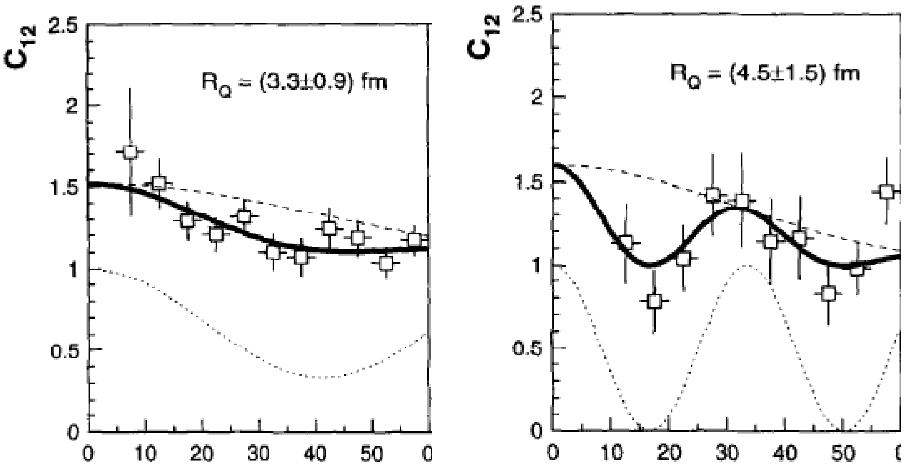

Figure 3.5: (Left) Two photon correlation function measured for the Kr+Ni system at 60A MeV, is plotted against the Lorentz invariant relative four momentum $Q_{inv} = \sqrt{q_0^2 - \mathbf{q}^2}$ (Right) The same for the Ta+Au system 39.5 MeV. The figures are adopted from Ref. [92].

emission [83]. It is also suggested that the ratio (R_o/R_s) strongly increases in the presence of a mixed phase between QGP and hadronic phase [84, 85]. However the ratio is found $\sim$ 1.0 from the RHIC experiment [86], leads to HBT-puzzle [87]. A definite conclusion of the puzzle appears in Ref. [88], where the source of discrepancy is explained as the inclusion of pre-equilibrium flow, viscosity, etc. influences the evolution dynamics.

3.2.2 Intensity interferometry of direct photons

The idea to study the interferometry of high energy photons in heavy ion collisions was first proposed by D. Neuhauser [89]. Intensity interferometry of hadrons carries information of the later dilute stages of relativistic heavy ion collision where they are created mostly. The two hadron correlation function is affected by final-state interaction among the hadrons and contribution from the resonance decay. In contrast, the direct photons have advantage of electromagnetic coupling with the medium. They are not suffering from any final-state interactions or feed down contribution, once they are created. Thus two photon intensity correlation is an efficient probe of the structure and lifetime of the central dense region created the collision. The only shortcoming in performing such measurement in experiment, is to subtract the huge background of photons coming from decay of neutral pions ($\pi^0 \rightarrow 2\gamma$).

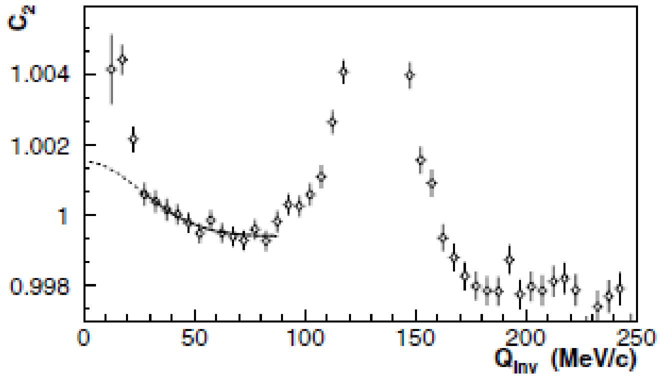

Figure 3.6: Two photon correlation function is plotted against Q_{inv} for the average transverse momentum window $200 < \mathbf{K_T} < 300$ MeV/c. The solid line shows the parameterization. The figure is adopted from Ref. [93].

Several works has been done during the past decades [69, 90] which establish the applicability of photon intensity interferometry to trace the dynamics of evolution of QGP. Some recent works have suggested an interference of photons emitted from quark matter and hadronic matter, both in central and non-central collisions of heavy nuclei [70, 91]. Similar phenomenon already observed in intermediate energy nuclear collisions, where the hard photons are emitted from two sources separated in space-time [75, 92]. The authors of Ref. [92] has observed the density oscillations in the system Kr+Ni at 60A MeV (or Ta+Au at 39.5A MeV) via hard photon intensity interferometry in the momentum range $\mathbf{K_T} \leq 20$ MeV/c (see Fig. 3.5).

For high energy nuclear collisions, WA98 collaboration of CERN has so far succeeded in measuring the two photon correlation function in central collisions of Pb nuclei at SPS energy(158A GeV) [93]. An one dimensional analysis of the correlation function is performed for the photons of average momenta $200 < \mathbf{K_T} < 300$ MeV/c (see Fig. 3.6). The correlation function is parameterized as:

$$C(Q_{inv}) = A[1 + \lambda exp(-Q_{inv}^2 R_{inv}^2)], \tag{3.32}$$

where R_{inv} is the invariant radius parameter corresponding to relative momentum $Q_{inv}(= \sqrt{q_0^2 - \mathbf{q}^2})$. A is the strength of the Gaussian, λ denotes the correlation strength. The analysis has found the invariant radius of the photon emitting source is about 6 fm, which is comparable to the radius extracted from the interferometry of pions of same momenta [93]. However the clear significance of R_{inv} is debatable so far [94].

3.3 Interferometry of thermal photons at RHIC and LHC

In this section, we study the intensity interferometry of thermal photons at the RHIC and LHC energies for the two EOS [95], HHB and HHL, discussed in the preceding chapter. We are interested of the photons having average transverse momenta $\mathbf{K_T} <$ 2 GeV. Our formalism closely follows the framework of earlier analysis [77, 70] on the same line. The spin-averaged correlation function of two photons, having momenta $\mathbf{k_1}$ and $\mathbf{k_2}$ is following from Eq. 3.23:

$$C(\mathbf{q},\mathbf{K}) = 1 + \frac{1}{2}\frac{\left|\int\, d^4x\, S(x,\mathbf{K})e^{ix\cdot q}\right|^2}{\int\, d^4x\, S(x,\mathbf{k_1})\ \int d^4x\, S(x,\mathbf{k_2})}\ , \tag{3.33}$$

where the (+) sign stands for bosons and the '1/2 'factor arises due to sum over photon polarisation in the final state. The emission function $S(x,\mathbf{K})$ or the invariant photon production rate is given by the hydrodynamic calculation. For the interference of photons emitted from the QGP phase and hadronic phase, the source term 'S'in the numerator is expressed as; $S_Q + S_H$. S_Q and S_H are the photon emission rates from QGP and hadron phases respectively. In the denominator, we put S_Q and S_H both.

In terms of different HBT radii, the two photon correlation function can be written as:

$$C(\mathbf{q},\mathbf{K}) = 1 + \frac{1}{2}exp\{-q_o^2R_o^2 - q_s^2R_s^2 - q_l^2R_l^2\}, \tag{3.34}$$

where we have considered photon pairs with vanishing rapidity in the center of momentum frame of a symmetric collision. Thus the cross-term of Eq. 3.30 vanishes.

We generate thermal photon distribution for the two EOS in the transverse momenta region $k_T \in$(0.1–4.0) GeV (as discussed in the earlier chapter) and distribute them uniformly over the rapidity (y) and azimuthal (ψ) space. Then we sample the photon pairs such that their average transverse momentum ($\mathbf{K_T}$) is less than 2 GeV. The two photon correlation function along different directions is calculated from Eq. 3.33. In order to bring out correct dependence of the correlation function on a particular momentum difference, the momenta of the interfering photons are such chosen that when $q_o \neq 0$, q_s and q_l are zero exactly. Like; for this criterion we choose $y_1 = y_2$ =0 and $\psi_1 = \psi_2$ =0.

We calculate outward, sideward and longitudinal correlation functions at the RHIC energy for a typical photon momentum $\mathbf{K_T}$ ≈1.7 GeV. The results are displayed in

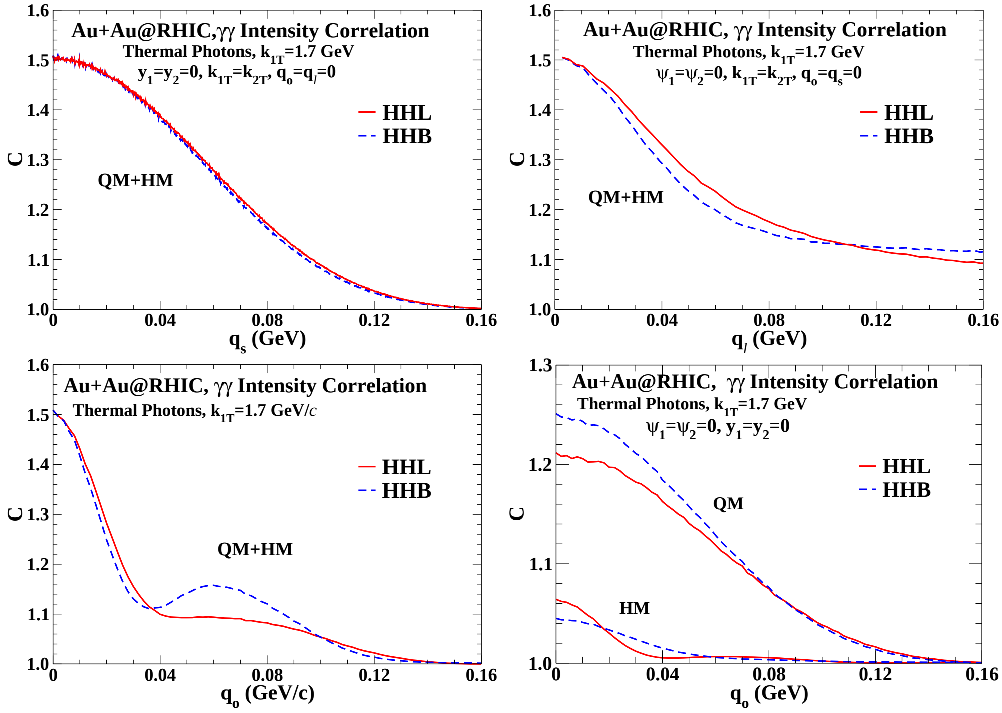

Figure 3.7: (Upper panel) Two photon correlation function at RHIC is plotted with sideward and longitudinal momentum difference; (Lower panel) the same plotted with outward momentum difference and the individual contributions from each phases.

Fig. 3.7. It is found that the sideward correlation function is identically similar for the two EOS while the longitudinal correlation function shows a slight difference. The more surprising fact awaits in case of outward correlation function, we see a clear distinction between the two equations of state. Bearing in mind that the interference pattern depends on the relative contributions from quark phase and hadronic phase, we have also plotted the relative contributions of each phase (Fig. 3.7). This can be done by retaining either S_Q or S_H in the numerator and denominator of Eq. 3.33. One may conclude from Fig. 3.7, the main source of the difference lies in the hadronic matter contribution to the total correlation function.

Next we investigate the underlying HBT radii of the photon source in QGP (Q) and hadronic (H) phase along the outward direction. The source function is parameterized as:

$$|\rho_{i,\alpha}| \;=\; I_\alpha \;\exp\left[-\;0.5\;(q_i^2 R_{i,\alpha}^2)\right], \tag{3.35}$$

where i= o, s or l in an obvious notation and I_α denotes the photon fraction coming from

QGP or hadronic phase. Thus $I_Q = dN_Q/(dN_Q + dN_H)$ and $I_H = dN_H/(dN_Q + dN_H)$. The correlation function for each phase is given by:

$$C(q_i, \alpha) = 1 \ + \ 0.5|\rho_{i,\alpha}|^2. \tag{3.36}$$

The total correlation function includes the interference between the two sources is the following [75, 70]:

$$C(q_i) \ = \ 1 \ + \ 0.5 \left[\ |\rho_{i,Q}|^2 \ + \ |\rho_{i,H}|^2 \ + \ 2 \ |\rho_{i,Q}||\rho_{i,H}| \ \cos(q_i \Delta R_i) \right], \tag{3.37}$$

where ΔR_i stands for the space-time separation between the two sources.

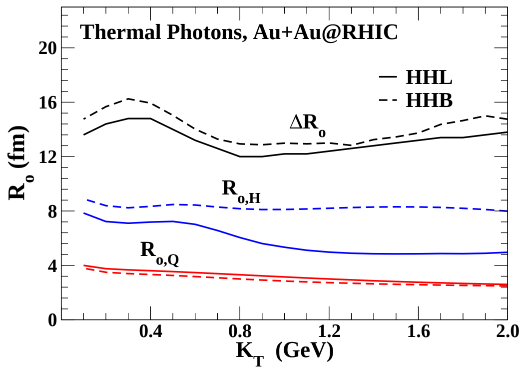

Figure 3.8: Transverse momentum dependence of outward radii of the photon emitting sources in the QGP and hadronic phase for Au+Au collisions at RHIC

From Eqs.(3.36) and (3.37) we obtain the outward HBT radii (in fm) of each source and their separation, for the thermal photons having $\mathbf{K_T}$ ≈1.7 GeV at RHIC energy for the two EOS. As the calculations are done with a smooth hydrodynamic model, the uncertainty in the parameters are assumed to be small.

$$\textbf{HHB} \quad R_{o,Q} = 2.5, \ R_{o,H} = 8.3, \ \Delta R_o = 14.9 \ . \tag{3.38}$$

$$\textbf{HHL} \quad R_{o,Q} = 2.7, \ R_{o,H} = 4.8, \ \Delta R_o = 13.4 \ . \tag{3.39}$$

We find the outward radius in the QGP phase ($R_{o,Q}$) is comparable for the two EOS. However a large difference between the radii is seen in case of hadronic phase ($R_{o,H}$), which we anticipated. We also find the separation (ΔR_o) between the two sources is little larger for the HHB EOS. These can be understood as the HHB EOS includes a mixed phase, the system lived longer (in particular the hadronic matter part).

We have also shown the transverse momentum dependence of $R_{o,Q}$, $R_{o,H}$ and ΔR_o of the thermal photons at the RHIC energy(Fig.3.8). It is seen that $R_{o,Q}$ is nearly similar for the two EOS while $R_{o,H}$ shows substantial deviation in the range of momenta; 0.1< $\mathbf{K_T}$ <2.0 GeV.

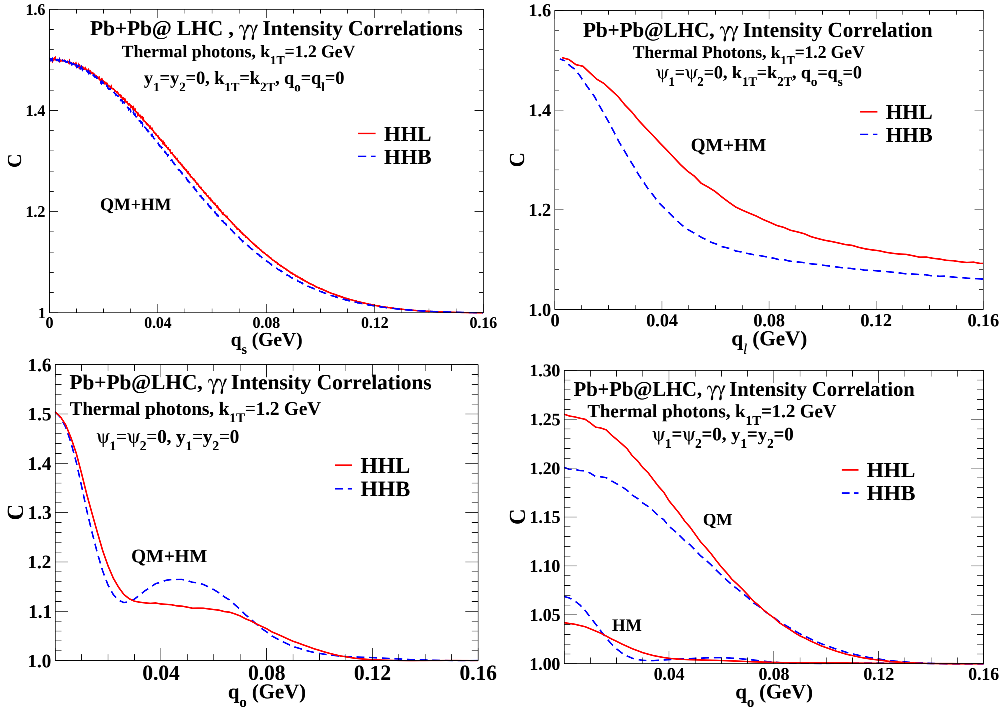

Figure 3.9: (Upper panel) Two photon correlation function at LHC is plotted with sideward and longitudinal momentum difference; (Lower panel) the same plotted with outward momentum difference and the individual contributions from each phases.

Next we investigate the intensity correlation of thermal photons for the collisions of Pb nuclei at the top LHC energy. Following the same treatment described above, we have calculated the outward, sideward and longitudinal correlation function for a typical momentum $\mathbf{K_T} \approx 1.2$ GeV. The results are depicted in Fig. 3.9. Similar to earlier study at RHIC, the sideward correlation function is found minimum sensitive to the choice of EOS. The longitudinal correlation function is now seen to distinguish between the two EOS. It would be interesting to see whether the shape remains intact at other rapidites. However this will need a 3+1D hydrodynamic simulation of the system which is beyond the scope of present study. The outward correlation function is found most sensitive to the difference between the two EOS. We have also shown the quark matter and hadronic matter contribution to the total correlation function. As seen earlier, the difference mainly arises due to the interference of photons coming from hadronic phase. We have not extracted HBT radius parameters in this case but expect to follow similar variation like the RHIC energy(Fig.3.8).

In this chapter, we have discussed the formalism of first order (namely amplitude interference) and the second order interference (namely intensity interference) in optics. Both interferometry techniques are used in astronomy for determining the size of distant celestial objects. The intensity interferometry gains advantage over the ordinary interferometry in case of smaller wavelengths. The second order interference can also be interpreted as the quantum statistical effect due to symmetrization or anti-symmetrization of the wave function of two identical particles originated close in phase space. We discussed in particular the intensity interference of direct photons in relativistic nuclear collisions as a probe of the space-time structure of the system. We have cited examples of such measurements in earlier experiments. The present work explores the intensity interferometry of thermal photons at the RHIC and LHC energies for the two equations of state constructed earlier and find exciting possibility to differentiate between them [95]. The observation could be valuable to probe the EOS of strongly interacting matter in experiment.

Chapter 4

System size dependence of nuclear modification factor

4.1 Introduction

The production of hadrons with large transverse momenta is found to be strongly suppressed in the central collisions of heavy nuclei at the energies available at the Relativistic Heavy Ion Collider experiment and the Large Hadron Collider experiment [96, 97]. This phenomenon commonly referred as '*jet quenching*' [98] originates due to interaction of hard partons with the surrounding medium created in relativistic heavy ion collisions. In the early pre-equilibrium phase of the collision, often two hard partons are created back-to back in the processes involving large momentum transfer. They traverse through the dense QGP fireball, losing energy through multiple collisions and fragment into hadrons outside the medium. The energy loss of the parton occurs from both collisional [99, 100] and radiative processes [101, 102], calculated within the framework of perturbative QCD (pQCD). However the radiative mode is found to to be dominant [103]. It is difficult to measure directly the amount of energy loss of the scattered parton, but it is imprinted through the leading hadron momentum which is recorded in experiment. The suppression in the hadronic momentum spectra is measured in terms of the nuclear modification factor ($R_{\rm AA}$) defined by:

$$R_{\rm AA}(p_T, b, \sqrt{s}) = \frac{d^2N_{\rm AA}(b)/dp_T dy}{T_{\rm AA}(b)(d^2\sigma_{\rm NN}/dp_T dy)}, \tag{4.1}$$

where the numerator gives the invariant yield of hadrons in AA collisions with impact parameter b at the center of mass energy ($\sqrt{s}$). The denominator contains the production cross-section of hadrons for pp collisions at the corresponding center of mass energy per nucleon multiplied by the nuclear overlap function ($T_{\rm AA}(b)$).

Thus if AA collision is considered as an incoherent superposition of pp collisions, $R_{\rm AA}$ would be equal to unity (neglecting the effect of nuclear parton distributions) and there will be no suppression. However the experimental data shows $R_{\rm AA} < 1$; implies the existence of a strongly interacting QCD medium.

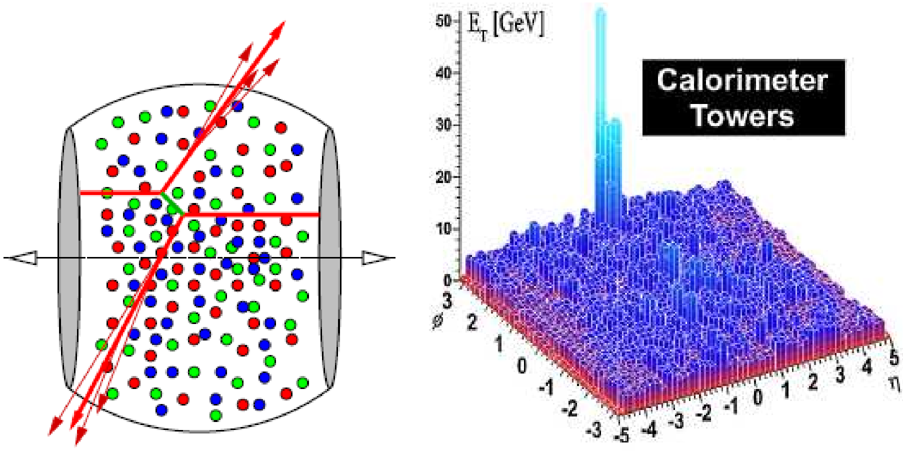

Figure 4.1: (Left) Schematic picture of two hard jets created back-to back inside the fireball. One of the jet (near-side) travels a small path before it escapes the medium, the energy of the jet remains unaltered. While the other (away-side) jet travels a long distance, suffers multiple scatterings and energy loss. (Right) The dijet asymmetry is a manifestation of the jet-quenching, observed by ATLAS collaboration [104] for Pb+Pb collisions at $\sqrt{s_{NN}}$= 2.76 TeV.

The jet-quenching has several other consequences. The jets created in a non-central collisions would transverse different distances in and out direction of the reaction plane and lose differing amount of energy. This will cause an azimuthal anisotropy in the momentum spectra of the final state hadrons of non-hydrodynamic origin [105]. Next we consider the large momentum photons coming from the fragmentation of a hard quark jet. The energy loss of the parent jets prior to fragmentation leads to nuclear suppression and azimuthal anisotropy of these hard photons at large p_T.

There exist a series of theoretical studies during the last decades on the topic; how a light parton loses energy while traversing a hot and dense QGP medium. Here we have enlisted some notable works among them.

The first ever attempt was made by Bjorken [99], considering elastic scatterings with the medium constituents. The differential energy loss per unit length (dE/dz) has been found proportional to the square of the plasma temperature. Later developments on the subject includes finite-temperature field theory approach [106], careful treatment of Debye screening mass and kinematics [107].

The first calculation of radiative energy loss in a QCD medium incorporating LPM effect was presented by Gyulassy and Wang [101] where the fast parton is assumed to move under screened Coloumb potential produced by the static scattering centers. Later Baier *et al.* (BDMPS) [102] include the re-scattering of gluons in the above model which is an important assumption for the dense medium. It has been found that the constructive or destructive interference among the emitted gluon quanta depends on the formation time of the radiated gluon. We shall discuss this feature in detail later. The differential energy loss (dE/dz) in case of coherent gluon emission is found proportional to the path length traversed by the hard parton.

The more recent and sophisticated studies on the medium evolution of light parton energy loss are the following:

- **Higher Twist (HT)** [108]: The scheme calculates all medium enhanced soft gluon contribution to the scattering cross-section, which are generally suppressed by the power of Q (the hard momentum scale) but enhanced in case of large nuclei. Thus a hard parton scatters off a soft gluon of the medium prior to emit radiation.

- **GLV**: The Gyulassy-Levai-Vitev model [109] develops on the static scattering center model of Gyulassy and Wang [101] with a color screened potential. The scattering amplitude is expanded in terms of opacity parameter (L/λ) where L is the length of the medium and λ is the mean free path. In the first order opacity expansion the gluon spectrum reduces to BDMPS result for the asymptotic parton energy limit ($E \to \infty$).

- **ASW**: The multiple scattering picture of BDMPS is first developed within a path-integral formalism by Zakharov [110]. The formalism of Armesto, Salgado, and Wiedemann [111] uses the opacity expansion of the scattering amplitude in a path integral formalism and accounts for the finite probability of scattering of both incoming and outgoing partons. Finally in the large length limit; one recovers the gluon radiation spectrum of BDMPS formalism.

- **AMY**: In the Arnold-Moore-Yaffe [112] scheme the hard parton is assumed to move in an equilibrium quark-gluon medium at very high temperature (T). Thus the parton have momentum ∼T and undergoes soft scatterings with momentum transfer $\sim g_s$T (g_s is the strong coupling). The radiated gluons further scatter in the medium with typical scale $\sim g_s^2$T. Thus the hard thermal loop (HTL) perturbation technique is used to resum all such contributions in the gluon radiation spectrum.

All the above models are equivalent in the sense that the pQCD techniques are used to estimate the in-medium energy loss of the hard jets. All the schemes calculate the change in gluon radiation spectrum of the parton due to medium effect and the leading parton always fragments outside the medium. The difference between the formalisms arise from (i) the hadron contribution coming from sub-leading gluons, (ii) including or excluding interference among the radiated gluons, (iii) considering a static or dynamic QGP medium, etc. A nice compilation of all approaches (except GLV) on a common relativistic hydrodynamic medium can be found in Ref. [113]. The study has found that the values of the transport coefficient ($\hat{q}$) for the three approaches differ significantly to describe the nuclear modification of hadron production at RHIC.

However for the current study, we have used a simple phenomenological model which demonstrates the evolution of parton energy loss mechanism with p_T of final hadrons. The model was first used at the RHIC energy [114] to explain the origin of neutral pion (π^0) suppression at large p_T and later used at the LHC energy [115]. The earlier works were done for most central collisions. The present study [116] explores the system size dependence of parton energy loss mechanisms through explaining the nuclear modification of hadron production from most central to peripheral collisions, at the RHIC and LHC energy.

4.2 Theoretical Formalism

4.2.1 Particle production in pp collisions

As a first step, we discuss the particle production in elementary pp collisions using next-to leading order pQCD. The inclusive particle yield in pp collisions is often used as a reference in heavy ion experiment. The inclusive cross-section for production of particles can be written in the *factorisation regime* of QCD which states that at large values of p_T, the short distance dynamics is perturbatively calculable in terms of partonic cross-sections, while the dominant non-perturbative phenomena can be factorised in the parton densities of the colliding hadrons and the fragmentation function of the detected particle:

$$\frac{d\sigma^{AB\to C}}{d^2p_T dy} = \sum_{a,b,c} \int dx_a \int dx_b \int \frac{dz}{z^2} F_{a/A}(x_a, Q_F^2) F_{b/B}(x_b, Q_F^2) \frac{d\sigma(Q_R^2)_{ab\to c}}{d^2 p_{cT} dy_c} D_{c/C}(z, Q_f^2), \tag{4.2}$$

where $F_{a/A}(x, Q^2)$ is the parton distribution function (PDF) for the parton a and $F_{b/B}(x, Q^2)$ is the PDF for the parton b, for the nucleon A and B respectively. $D_{c/C}$ gives the fragmentation probability of parton c into a hadron C evaluated at $z = p_C/p_c$, where z is the fraction of the parton's momentum carried by the hadron. In case of photon production, $D_{c/\gamma}$ gives the probability that a photon will be fragmented off a quark with the momentum fraction $z = p_\gamma/p_c$. In addition, we have an extra term where photon is directly produced in the hard collision ($c = \gamma$) and the fragmentation function reduces to $\delta(1-z)$. The hard parton-parton cross-section ($\sigma_{ab\to c}(x_a, x_b, Q_R^2)$) is calculated for the leading order processes $\mathcal{O}(\alpha_s^2)$ such as:

$$\begin{aligned} &q + q \to q + q, \\ &q + \bar{q} \to q + \bar{q}, \\ &q + g \to q + g, \\ &g + g \to g + g, \\ &\ldots\ldots \end{aligned} \tag{4.3}$$

At the next-to-leading order, $\mathcal{O}(\alpha_s^3)$ we include subprocesses like:

$$q + q \to q + q + g \ ,$$

$$\begin{aligned} q+\bar{q} &\rightarrow q+\bar{q}+g, \\ q+q' &\rightarrow q+q'+g, \\ q+\bar{q} &\rightarrow q'+\bar{q}'+g, \\ g+g &\rightarrow g+g+g \\ &...... \end{aligned} \tag{4.4}$$

The running coupling constant $\alpha_s(\mu^2)$, is evaluated at the next-to-leading order from the 2-loop renormalisation group equation:

$$\alpha_s(Q_R^2) = \frac{12\pi}{(33-2N_f)\ln(Q_R^2/\Lambda^2)}\left(1 - \frac{6(153-19N_f)\ln\ln(Q_R^2/\Lambda^2)}{(33-2N_f)^2\ln(Q_R^2/\Lambda^2)}\right),$$

where Q_R is the renormalization scale, N_f is the number of flavors, and Λ is the $\Lambda_{\mathbf{QCD}}$ scale. There are three arbitrary momentum scales associated with the factorization (Q_F), renormalization (Q_R), and fragmentation (Q_f) processes. We set all the three scales equal to a common scale; $Q = cp_T$ and vary the constant c in order to match the experimental data.

We have used the program INCNLO [117] to calculate the above cross-section at the RHIC and LHC energies. The initial parton densities are given by *CTEQ4M* structure function [118] and the final state hadron fragmentation is obtained from the BKK fragmentation function [119]. In Fig. 4.2, we have shown the scale dependence of π^0 production for pp collisions at 200 GeV (RHIC) and charged hadron ($h^+ + h^-$) production at 2.76 TeV (LHC). It has been found that the scale $c = 1.0$ gives reasonably good description of the data measured by the PHENIX [120] and the CMS [121] collaboration. The quantitative description of the data from pp collisions provides us with a reliable baseline to calculate nuclear modification of hadron production in nucleus-nucleus collisions.

4.2.2 Particle production in AA collisions

The same factorised approach can be used for the particle production in nucleus-nucleus collisions while taking care of (i) Energy loss of partons in the medium and (ii) Nuclear Shadowing. The code is suitably modified to account for these effects. We shall discuss first the parton energy loss formalism used in this work.

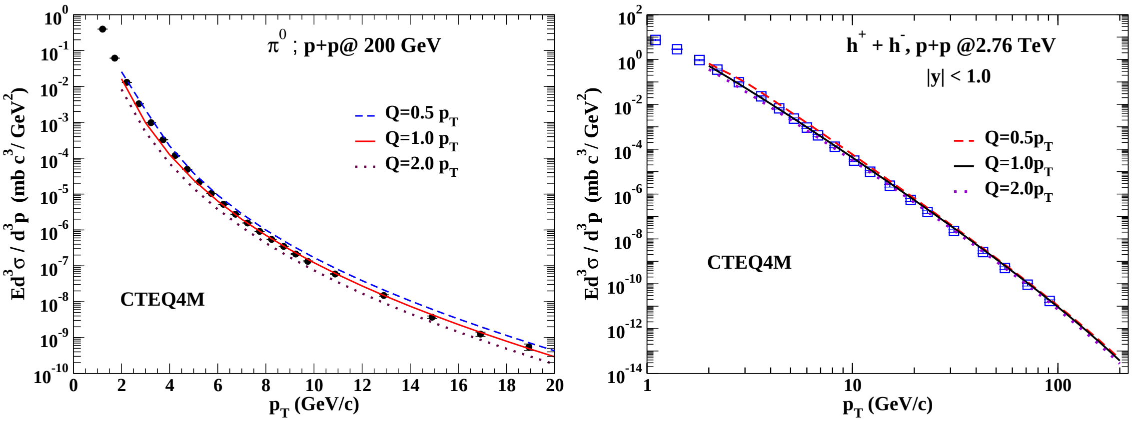

Figure 4.2: The scale dependence of neutral pion yield in p+p collision at $\sqrt{s}$= 200 GeV and charged hadron yield at $\sqrt{s}$= 2.76 TeV, compared with the data from the PHENIX and the CMS collaboration.

Model of parton energy loss

The energy loss model closely follows the treatment of Baier *et al.* [103, 122]. We have considered a static, homogeneous QCD medium of length (L), which consists of several static scattering centers in the spirit of Gyulassy-Wang model. The scattering centers are assumed to be infinitely heavy so they don't recoil after the scattering. Thus the collisional energy loss vanishes in this formalism. An energetic parton of energy E moves along z-direction through this medium, subjected to multiple scattering and energy loss in terms of induced gluon radiation. The emitted gluon of energy ω is assumed to be soft, i.e. $\omega \ll$E. The soft approximation leads to a picture of propagation of a relativistic particle on a straight trajectory with E$\gg \mu$ and receives independent momentum kicks from successive scatterings. μ is the typical momentum transfer in a single hard collision.

The key factors of our model are the average energy loss per collision (ε) by the parton, the mean free path of the parton (λ) and the average path length of the parton in the medium (L). We assume $\lambda <$ L such that several scatterings takes place in the medium. The distribution of n-scattering centers is assumed to be random and given by the probability distribution:

$$P(n, L) = \frac{(\mathrm{L}/\lambda)^{\mathrm{n}}}{n!}\, e^{-L/\lambda} \ . \tag{4.5}$$

Now the interference between the successive radiation amplitudes depends on the formation time of the emitted gluon. The formation time is defined as:

$$t_{\text{form}} \simeq \frac{\omega}{k_T^2}, \tag{4.6}$$

where ω is the energy of the radiated gluon and k_T is the transverse momentum. One would have $\omega \gg k_T$ for near-collinear emission.

The coherence length (l_{coh}) can be defined as the length in the medium over which the emitted gluon quanta interfere constructively.

$$l_{\text{coh}} \simeq \frac{\omega}{\langle k_T^2 \rangle_{\text{coh}}} \simeq \frac{\omega}{N_{\text{coh}} \langle k_T^2 \rangle}, \tag{4.7}$$

where N_{coh} is the number of coherent scattering centers. One can then write,

$$N_{\text{coh}} = \frac{l_{\text{coh}}}{\lambda} \simeq \sqrt{\frac{\omega}{\lambda \mu^2}} \equiv \sqrt{\frac{\omega}{E_{\text{LPM}}}}, \tag{4.8}$$

where $E_{\text{LPM}} = \lambda \mu^2$ is the energy parameter introduced to separate the incoherent and coherent radiation of gluons.

Depending on the formation time (or the coherence length) of the radiated gluon, we consider three different regimes of parton energy loss; **Bethe-Heitler (BH)** regime of incoherent energy loss, **LPM** regime of partial coherent and **complete coherence** regime of energy loss.

For small formation time $t_{\text{form}} \leq \lambda$ and $\omega \leq E_{\text{LPM}}$; incoherent radiation takes place over L/λ scattering centers. This is called as the BH regime of incoherent energy loss. Since successive scatterings are independent, the total gluon radiation spectrum is proportional to the single scattering spectrum. The energy loss per unit length in this regime writes as:

$$-\frac{dE}{dz} \approx \frac{\alpha_s}{\pi} N_c \frac{1}{\lambda_a} E \ , \tag{4.9}$$

where $N_c = 3$ and E is the energy of the parton. We write $\varepsilon \approx kE$ for this case and determine k from the data of nuclear modification of hadron production.

Next we discuss LPM suppression of emitted gluon radiation having formation time greater than λ but less than L and energy $\omega > E_{\text{LPM}}$. According to LPM principle, multiple scatterings do not generate multiple radiation of gluon when coherence time is large. The radiation process does not resolve between single and multiple scatterings as only the total momentum transfer matters. Thus the radiation over N_{coh} scattering centers added coherently gives rise to total energy loss. We find the gluon radiation amplitude of the LPM limit is suppressed by a factor of '$1/\sqrt{\omega}$'compared to the BH limit [122]. The energy loss per unit length written as:

$$-\frac{dE}{dz} \approx \frac{\alpha_s}{\pi}\frac{N_c}{\lambda}\sqrt{E_{\text{LPM}}E} \ . \tag{4.10}$$

Thus for LPM regime $\varepsilon \approx \sqrt{\alpha E}$ and α will be determined from the from the measurement of R_{AA}.

Finally, in the large formation time (t_{form} > L) and large energy limit ($E_{\text{LPM}} < \omega < E$) of the emitted gluon, we are in the complete coherence regime of energy loss. The radiations from all scattering centers added coherently as if one single scattering takes place for the entire medium. This is called the complete coherence regime of energy loss and the energy loss per unit length becomes constant, independent of parton energy:

$$-\frac{dE}{dz} \approx \frac{\alpha_s}{\pi}N_c\frac{\langle k_T^2\rangle}{\lambda}L \ . \tag{4.11}$$

This is denoted as constant energy loss ($\varepsilon \approx \kappa$) regime as the parton would lose constant amount of energy in each collision.

A careful calculation of the Eq. 4.11 leads to [103]:

$$-\frac{dE}{dz} = \frac{\alpha_s}{4}N_c\frac{\langle k_T^2\rangle L}{\lambda_a}\tilde{v} \ . \tag{4.12}$$

where $\tilde{v}$ is Fourier transform of the normalized differential parton scattering cross-section for the appropriate momentum transfer scale. The momentum transport coefficient $\widehat{q}$ is then defined as

$$\widehat{q} = \frac{\langle k_T^2\rangle}{\lambda_a}\tilde{v} \ , \tag{4.13}$$

so that we can write

$$-\frac{dE}{dz} = \frac{\alpha_s}{4}N_c\widehat{q}L \ . \tag{4.14}$$

The Eq. 4.14 can be used to deduce the average momentum transport coefficient for a given centrality.

Here we shall note that k is dimensionless and α, κ have the unit of GeV. The parameters k, α, κ are varied to get an accurate description of the nuclear modification factor of hadrons (R^h_{AA}) at different centralities of collisions. We have kept the mean free path (λ) as 1 fm for quarks and gluons both. The average path length $\langle L\rangle$ of the parton inside the medium for a given centrality is calculated using the optical Glauber model. The phenomena of multiple scattering and energy loss of partons enter into

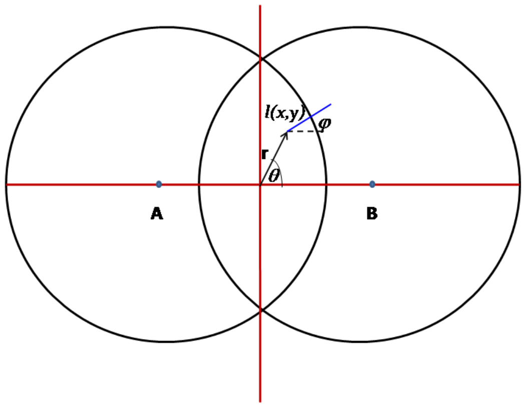

Figure 4.3: Schematic sketch of path length traversed by the parton in non-central collisions of two symmetric nuclei A and B.

the particle production description (Eq. 4.2) through the modification of vacuum fragmentation function $D^0(z, Q^2)$. We have followed the prescription of medium modified fragmentation function by Wang *et al.* [123], described as:

$$zD_{c/C}(z, L, Q^2) = \frac{1}{C_N^a} \sum_{n=0}^{N} P_a(n, L) \times \left[z_n^a \, D^0_{c/C}(z_n^a, Q^2) + \sum_{m=1}^{n} z_m^a \, D^0_{g/C}(z_m^a, Q^2) \right] \quad (4.15)$$

where $z_n = zE_T/(E_T - \sum_{i=0}^{n} \varepsilon^i)$, $z_m = zE_T/\varepsilon_m$. The first term represents the hadronic contribution of a leading parton with a reduced energy $(E_T - \sum_{i=0}^{n} \varepsilon^i)$ and the second term represents the hadronic contribution of the emitted gluons, each having energy ε_m. $C_N = \sum_{n=0}^{N} P(n, \langle L \rangle)$ and N is the maximum number of collisions suffered by the parton, equal to E_T/ε.

The azimuthal (ϕ) variation of path length with respect to reaction plane for non-central collisions is evaluated using the optical Glauber model. Assuming uniform densities for the colliding nuclei, the average path-length for an impact parameter b and azimuthal angle ϕ can be written as:

$$L(\phi; b) = \frac{\int\int \ell(x, y, \phi, b) T_{AB}(x, y; b) \, dx \, dy}{\int\int T_{AB}(x, y; b) \, dx \, dy}, \quad (4.16)$$

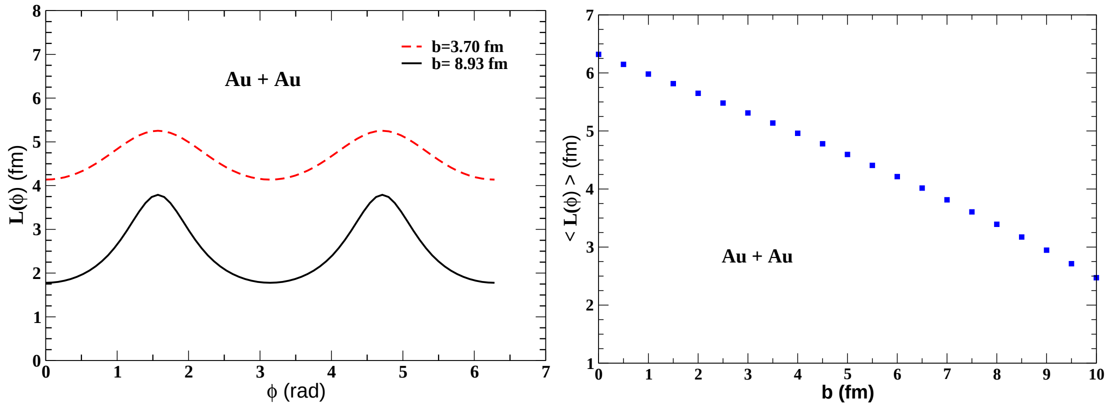

Figure 4.4: (Left panel) Azimuthal variation of the average path length traversed by a parton in collision of Au nuclei. The impact parameter for the upper curve is an average for 0-20% most central collisions and the lower one is for 40-60% centrality.(Right panel) The average path length vs. impact parameter for Au+Au system.

where x and y are the transverse co-ordinates for the point where the partons scatter to produce the jet(s) which traverses the path length $\ell(x, y, \phi, b)$ at an angle ϕ with respect to the reaction plane (Fig. 4.3). $T_{AB}(x, y; b) = t_A(x + b/2, y)t_B(x - b/2, y)$ is the nuclear overlap function and t_A and t_B are the transverse density profiles of the two nuclei. An average of $L(\phi; b)$ over ϕ (varying from zero to 2π) gives the average path length $L(b)$ (see Fig. 4.4).

Nuclear shadowing

Deep inelastic lepton-nucleus scattering experiments has revealed that the distribution of partons inside a large nucleus is considerably different than a free nucleon. The phenomenon has been first reported by the European Muon Collaboration (EMC) when measured the ratio of structure functions of iron and deuterium nucleus in the deep inelastic scattering of muons. The ratio, plotted against the momentum fraction of nucleon carried by the bound parton (Bjorken x), shows distinct behaviour at different regions of x [124]. Several theoretical models were proposed to explain the observed feature, based on application of QCD for a many-body system [125].

Now the parton distribution for flavor i inside a nucleus of mass number A consists of Z protons and (A-Z) neutrons, is defined as:

$$f_{i/A}(x, Q^2) = R_i^A(x, Q^2)[\frac{Z}{A} f_{i/p}(x, Q^2) + \frac{A - Z}{A} f_{i/n}(x, Q^2)], \tag{4.17}$$

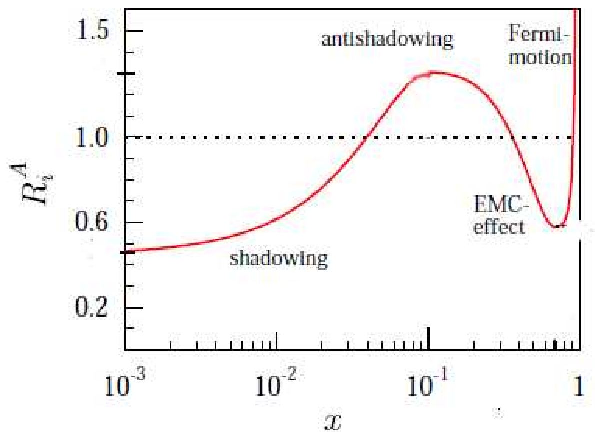

Figure 4.5: Schematic plot of nuclear modification to the free nucleon PDF at various regions of momentum fraction x (adopted from JHEP **0904** (2009) 065).

where $R_i^A(x, Q^2)$ denotes the nuclear modification to the free nucleon PDF. The parameterization of $R_i^A(x, Q^2)$ is performed at charm mass threshold $Q_0^2 = m_c^2 = 1.69GeV^2$. At higher scales $Q^2 > Q_0^2$, the nuclear parton distributions are obtained by solving the linear DGLAP evolution equation. The different kinematic region of R_i^A are schematically shown in Fig. 4.5.

1. Shadowing region ($x \lesssim 0.1$): a large suppression in the parton distributions, can be explained through gluon fusion in an infinite momentum frame [126].

2. Anti-shadowing region ($0.1 \lesssim x \lesssim 0.3$): an enhancement in the parton distributions, originates due to conservation of parton momentum.

3. EMC region ($0.3 \lesssim x \lesssim 0.7$): the original region of suppression in the cross-section observed by the EMC collaboration.

4. Fermi motion ($x > 0.7$): an enhancement in the parton distribution, attributed to the intrinsic motion of nucleons in the rest frame of nucleus.

There are several parameterizations of the factor $R_i^A(x, Q_0^2)$ available. We have used the EKS98 parameterization of nuclear parton distributions by Eskola *et al.* [127] which shows a very good agreement between leading DGLAP evolution of nuclear parton distributions and the Q^2 evolution of the NMC data. Since this work was published several somewhat improved PDF as well as shadowing functions have become available. However their use will not make any quantitative change in the results.

4.3 Nuclear modification of neutral pion production at RHIC

In the present study, we have calculated the centrality dependence of R_{AA} of neutral pions (π^0) for Au-Au and Cu-Cu collisions at $\sqrt{s_{NN}} = 200$ GeV [116] using the parton energy loss model discussed above. We have shown the results for four centrality classes viz. near central (0-10%, 10-20%) and mid central (40-50%, 50-60%). It has been found that different parton energy loss mechanisms are responsible for the suppressed production of π^0 at different regions of p_T.

4.3.1 $R_{\mathrm{AA}}^{\pi^0}$ for Au-Au collisions at RHIC

The suppressed production of neutral pions calculated with BH mechanism of energy loss are shown in Fig. 4.6 for the four centralities of collision. This mechanism is seen to provide a good description of the data for $p_T \leq 6$ GeV/c. The best fit value of the coefficient k is given by the solid line and the other two lines express the uncertainty in the value of k. The value $k = 0.10$ signifies that the parton will lose 10% of it's initial energy in the first collision, then 10% of the reduced energy in the second collision and so for. The energy loss coefficient k also decreases by 20% as we move from near central to mid-central collisions. We have noted that the slope of $R_{AA}^{\pi^0}$ changes around p_T= 5 GeV/c, indicates a possible change in the mechanism for energy loss for partons contributing to higher momenta.

This expectation becomes true, when the so-called LPM mechanism of energy loss is seen to follow the curvature of $R_{AA}^{\pi^0}$ in the p_T range of 6–10 GeV/c (see Fig. 4.7). As before, the best fit value of the coefficient α is shown by the solid red line. Thus a parton having energy 10 GeV would lose about 1 GeV in the first collision for 0-10% centrality.

The transition from BH limit to LPM limit at $p_T \approx 5$ GeV/c should not be treated as coincidence. We recall the parameter $E_{\mathrm{LPM}} = \lambda\mu^2$, which separates the BH and LPM regime of energy loss. If we take $\lambda \sim 1\ fm$ and average momentum transfer per collision

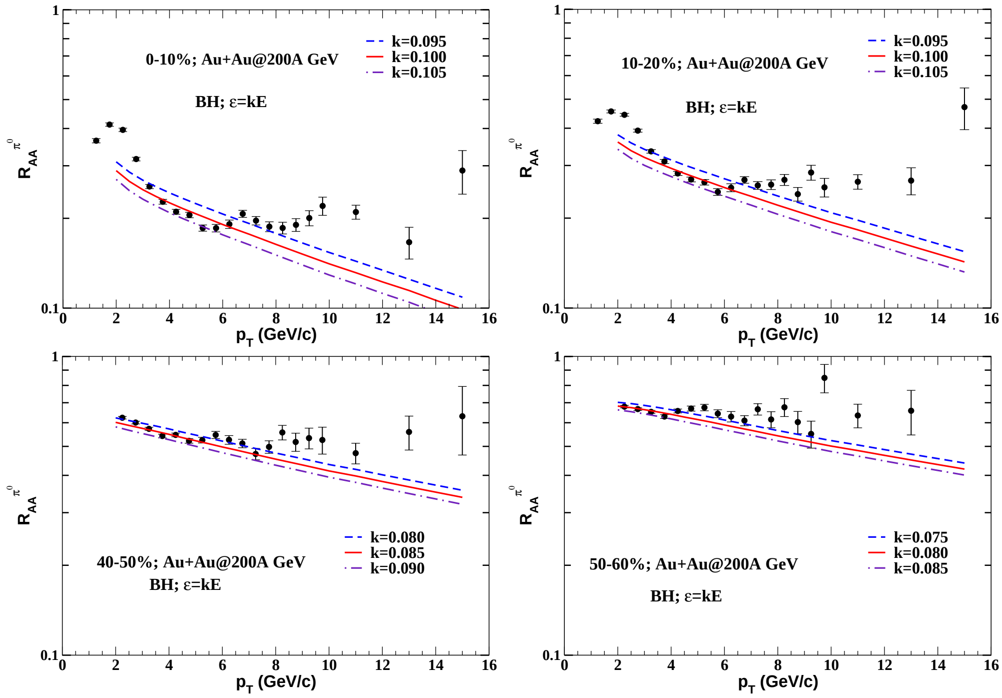

Figure 4.6: Nuclear modification of π^0 production for Au+Au collisions at $\sqrt{s_{\mathrm{NN}}}$=200 GeV, using BH mechanism. The experimental data are taken from Ref. [128].

$\mu \approx 1$ (GeV/c)^2; E_{LPM} comes about 5 GeV/c, where the transition takes place for all centralities.

Finally we see from Fig. 4.8, the hadronic suppression at large momenta $p_T > 8$ GeV/c is best described by the complete coherence regime of energy loss. The best fit value of κ is shown by the solid line. The parton would lose 1.4 GeV energy per collision in most central 0-10% and about 1 GeV for mid central 40-50% collisions.

Here we add that a quick look at Fig. 4.7 may lead to conclude that the description using the LPM mechanism is also working reasonably well till the largest p_T considered here. However a careful look at the Figs. 4.7 and 4.8 reveal that the LPM description mostly misses the data for larger p_T values while the description using the constant energy loss per collision correctly follows the curvature of the data till the largest p_T. A more accurate data extending up to even larger p_T at the LHC energy would settle this question. This will be discussed in the next section.

We also recall that the LPM and the complete coherence regimes differ by the formation time of the emitted gluons. This is reflected in a slight change in the curvature of the nuclear modification factor, around $p_T \approx 8$–10 GeV/c.

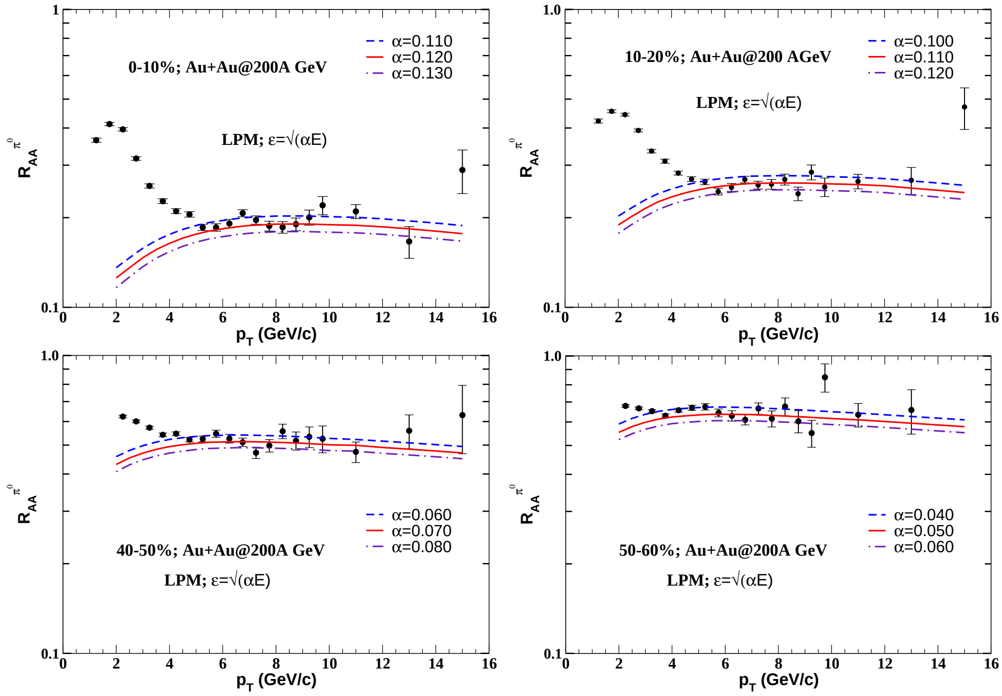

Figure 4.7: Nuclear modification of π^0 production for Au+Au collisions at $\sqrt{s_{\rm NN}}$=200 GeV using LPM mechanism. The experimental data are taken from Ref. [128].

4.3.2 $R_{\rm AA}^{\pi^0}$ for Cu-Cu collisions at RHIC

Following the success in describing the nuclear modification of hadron production in Au-Au collisions, next we analyse the data of neutral pion suppression in Cu-Cu collisions at the same center of mass energy. This is particularly interesting because central collisions of Cu nuclei have number of participants similar to mid central collisions of Au nuclei. Thus, a comparison would provide us results for two systems, one having small spatial eccentricity (most central) and the other possesses large spatial eccentricity (mid central).

Proceeding as earlier, we have shown the results for nuclear modification of π^0 production for Cu+Cu collisions at $\sqrt{s_{\rm NN}}$= 200 GeV for 0-10% most central and 30-40% mid central collisions (Fig. 4.9), using the three energy loss mechanisms and compared with the measurements by the PHENIX collaboration [129].

The the BH regime of energy loss is seen to describe the data for $p_T < 6$ GeV/c for all centralities and the coefficient k decreases about 30% from central to mid central event. The best fit value of all coefficients are shown by the solid line, as before.

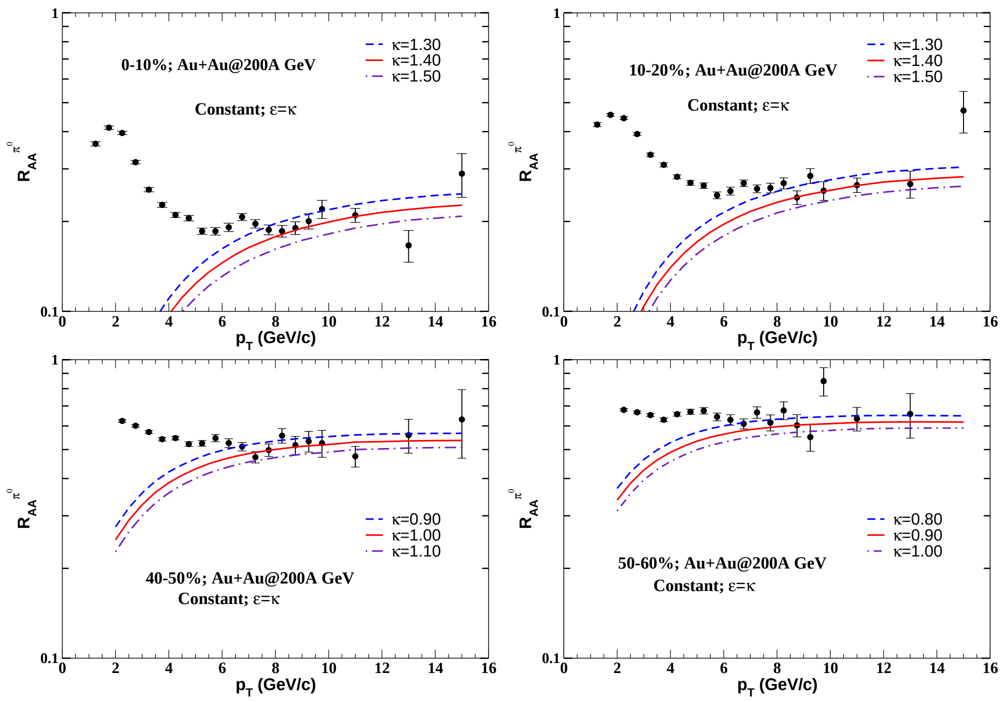

Figure 4.8: Nuclear modification of π^0 production for Au+Au collisions at $\sqrt{s_{\rm NN}}$=200 GeV in the complete coherence regime of energy loss. The experimental data are taken from Ref. [128]

The LPM regime of energy loss is seen to follow the curvature of nuclear modification factor over the p_T range 6-10 GeV/c and even beyond for the far central collisions.

Finally, for the region of $p_T >$ 6-8 GeV/c the complete coherence regime of energy loss is seen to work well. We find the demarcation of the LPM and constant energy loss mechanisms is not as sharp as it was for Au nuclei, especially for the less central collisions. This may have its origin in the smaller path length $\langle L \rangle$ for Cu nuclei.

It shall be noted that the energy loss coefficients obtained for the most central (0-10%) collision of Cu nuclei is quite close to the same for the mid central (50-60%) collisions of Au nuclei, for all three mechanisms. This verifies our earlier presumption and confirms the applicability of the energy loss model.

4.4 Nuclear modification of charged hadron production at LHC

The nuclear modification of charged hadron production ($R^{ch}_{\rm AA}$) for Pb+Pb collisions at $\sqrt{s_{\rm NN}}$= 2.76 TeV is calculated within the same framework of parton energy loss for four

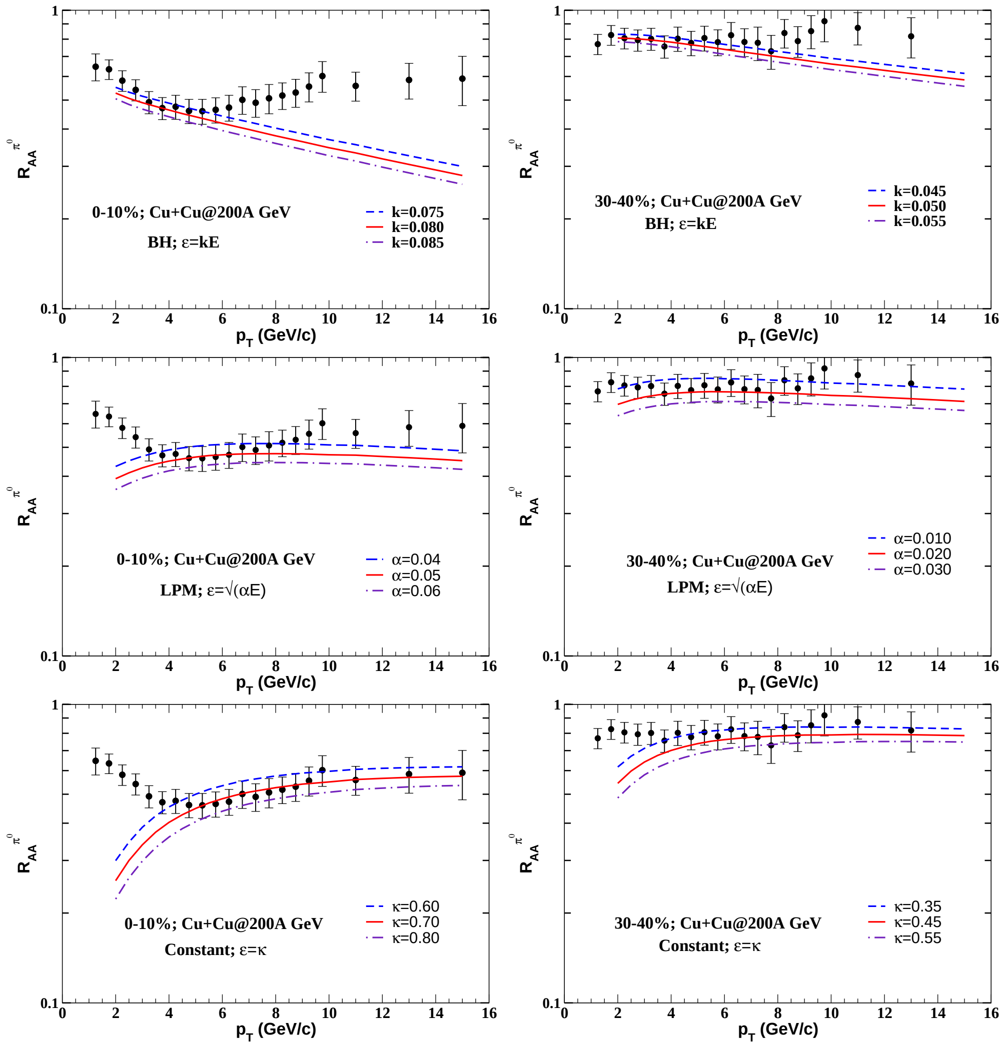

Figure 4.9: Nuclear modification of π^0 production for Cu+Cu collisions at $\sqrt{s_{\rm NN}}$=200 GeV for the BH, LPM and complete coherence regime of energy loss. The experimental data are taken from Ref. [129]

centralities of collision; 0-5%, 5-10%, 10-30%, 30-50% [130]. The parameters k, α, κ are systematically tuned to have a good agreement with the charged hadron suppression data from the CMS collaboration [131]. The results are displayed in Fig. 4.10 where we have shown the best fit value of the parameters only.

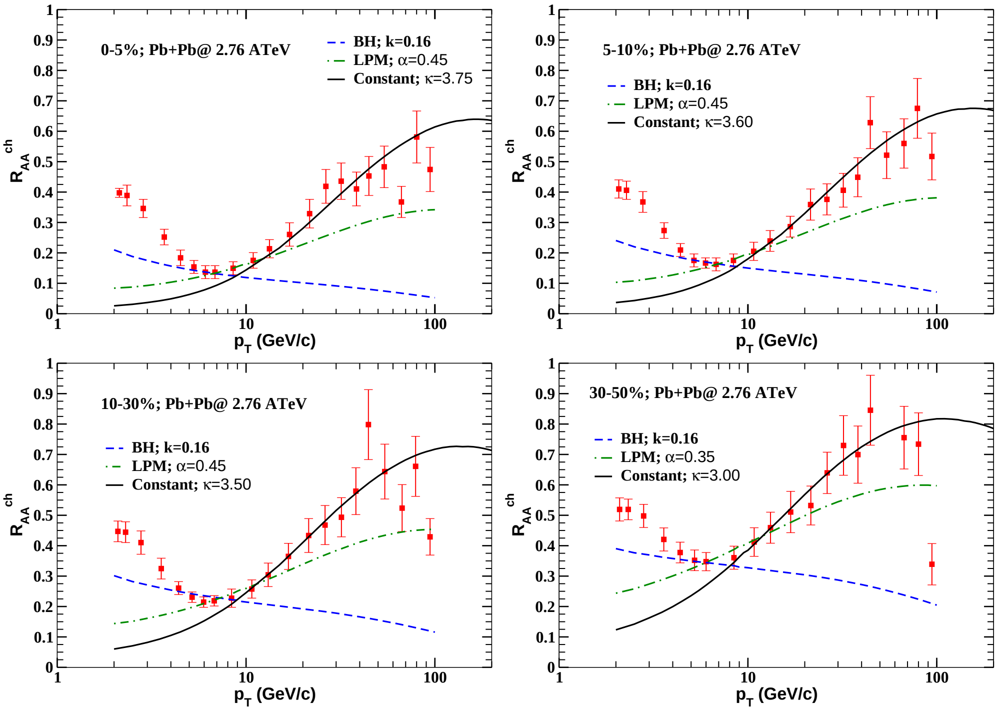

Figure 4.10: Nuclear modification factor of charged hadron production calculated for Pb+Pb collisions at $\sqrt{s_{\rm NN}}$=2.76 TeV, in the BH, LPM, and complete coherence regimes of energy loss and compared with the measurements by the CMS collaboration [131].

The BH mechanism of energy loss is seen to work nicely in the region of p_T, 5-8 GeV/c. A change in curvature of the data is noted near $p_T \approx 8$ GeV/c, where BH contribution to the nuclear modification factor drops slowly and the other energy loss mechanisms start operating. The LPM mechanism is seen to explain the data for the p_T range $\sim$ (6–15) GeV/c and even beyond for far-central collisions (30-50%). Finally, the complete coherence regime of energy loss has been found to follow curvature of the data over a broad region of p_T; 10 GeV/c $< p_T <$ 100 GeV/c. The bending of theoretical curve for $p_T >$ 100 GeV/c can be explained due to the anti-shadowing of nuclear parton distributions (see Fig. 4.5).

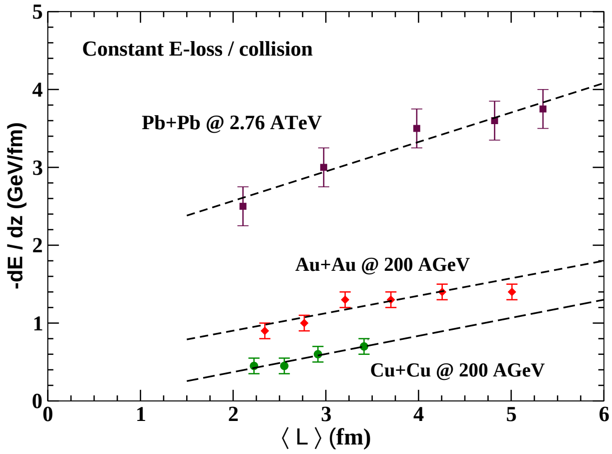

Figure 4.11: dE/dz vs average path length, $\langle L \rangle$ of the parton, for Au+Au and Cu+Cu collisions at 200 AGeV (RHIC) and for Pb+Pb collisions at 2.76 ATeV (LHC). The corresponding partons have $p_T > 8$ GeV/c for RHIC energies and > 10–12 GeV/c for LHC energies.

4.4.1 Centrality dependence of dE/dz and $\widehat{q}$

The energy loss per unit length is empirically determined as, $-dE/dz = \varepsilon/\lambda$, for the complete coherence regime of energy loss. Thus the concerned partons would have $p_T \geq 8$ GeV/c at RHIC and $p_T \geq 12$ GeV/c at the LHC center of mass energies. We have found the rate of energy loss needed to explain the nuclear modification data at large p_T, varies linearly with the average path length $\langle L \rangle$ for both at the RHIC and the LHC energies (Fig. 4.11). The error bar shown in Fig. 4.11 is related with the uncertainty of the parameter ε and dashed line describes the linear fit. Our empirical result confirms the conviction of Baier *et al.* that the total radiative energy loss suffered by the parton inside a static medium of length L, $\Delta E \propto L^2$ [103]. While the slopes of the fits for Au+Au and Cu+Cu collisions at RHIC are quite similar, it becomes more steeper for Pb+Pb collisions at LHC. This implies the parton radiative energy loss becomes more prominent at the LHC center of mass energy. Also the magnitude of energy loss rises about 2-3 times as we go from RHIC to LHC.

The average momentum transport coefficient $\widehat{q}$ for a particular centrality of collision can be obtained from Eq. 4.14. We find for Au+Au collisions at 200 AGeV, $\widehat{q}$ varies from 0.25 GeV^{2}fm^{-1} for 0-10% centrality to 0.39 GeV^{2}fm^{-1} for 50-60% collision centrality. The decrease of $\widehat{q}$ for more central collisions can be understood through the width of the transverse momentum distribution of the parton, $\langle p_{Tw}^2 \rangle = \widehat{q}L$ [122]. The width $\langle p_{Tw}^2 \rangle$ has been found about 1.25 GeV^2 for 0-10% and 0.90 GeV^2 for 50-60% collision centrality. This signifies the system produced in central collisions is much dense and hotter than in peripheral collisions. In case of Cu+Cu collisions, we get $\widehat{q} \approx 0.18$ GeV^{2}fm^{-1} for all the centralities. The near identity of $\widehat{q}$ for all the centralities is related to a smaller variation in the path length for them.

Using the same law, we have obtained $\widehat{q} \approx 0.63$ GeV^{2}fm^{-1} for 0-5% most central and 0.91 GeV^{2}fm^{-1} for 30-50% mid central collisions of Pb nuclei at 2.76 ATeV. This value is about 2 times higher than the same obtained for Au+Au collisions at RHIC energy.

It has been discussed earlier that various authors reported widely differing values of $\widehat{q}$, in order to explain the hadronic suppression data. Thus, ASW scheme has found a value of 5–10 GeV^{2}fm^{-1} and GLV scheme reported a value in the range of 0.35–0.85 GeV^{2}fm^{-1}. On the other hand HTL based AMY approach suggests $\sim$ 2 GeV^{2}fm^{-1}. It is assumed that part of the discrepancy lies due to different physical quantities of the expanding system over which the average is taken.

4.5 Azimuthal momentum anisotropy of hadrons

In the preceding sections, we have shown the success of our phenomenological model of parton energy loss in describing the nuclear modification of hadron production at the RHIC and LHC energies for different centralities of collision. In case of non-central collisions, the parton will have an azimuthal variation of path length in the transverse plane (see Fig. 4.3). This follows an azimuthal dependence of parton energy loss which causes azimuthal anisotropy in the final state hadron momentum spectra at large p_T.

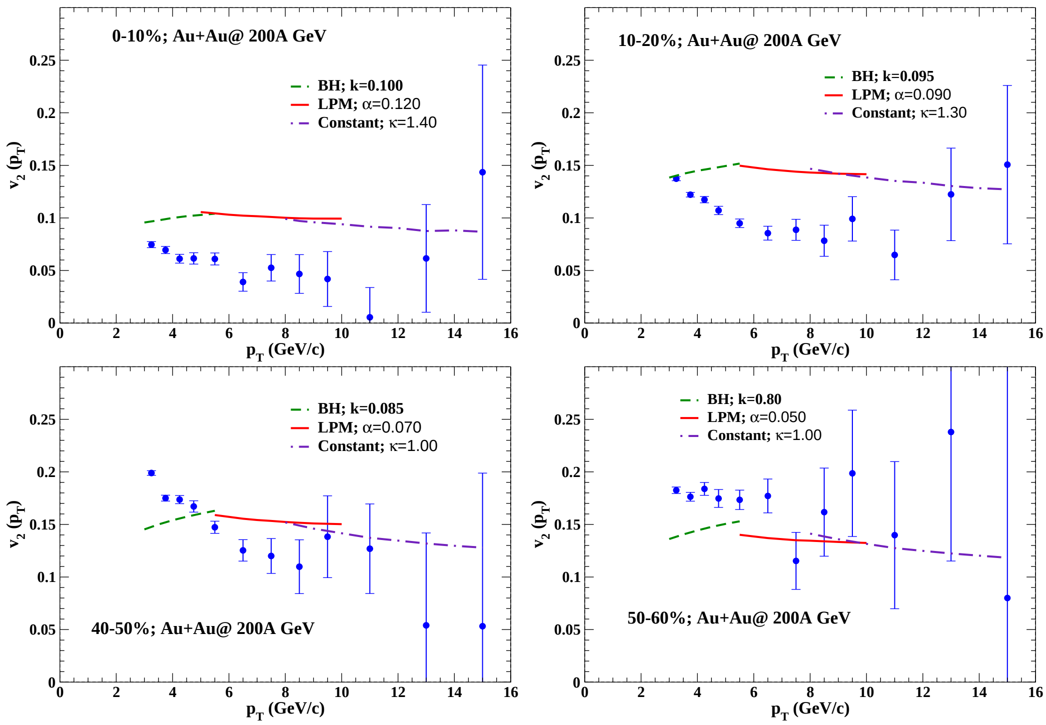

Figure 4.12: The differential azimuthal anisotropy coefficient v_2 of neutral pion calculated using the three energy loss mechanisms for Au+Au collisions at $\sqrt{s_{\rm NN}}$=200 GeV. The experimental data are from the PHENIX collaboration [132].

The differential azimuthal momentum anisotropy is measured in terms of the parameter $v_2(p_T)$, which is the second Fourier coefficient of the azimuthal distribution of hadrons in the reaction plane:

$$v_2(p_T) = \frac{\int_0^{2\pi} d\phi \, \cos(2\phi) dN/d^2p_T dy}{\int_0^{2\pi} d\phi \, dN/d^2p_T dy} \; . \tag{4.18}$$

Here we recall that the "elliptic" flow of hadrons seen at lower p_T [55], is completely different than the present scenario. The later is originated due to hydrodynamic expansion

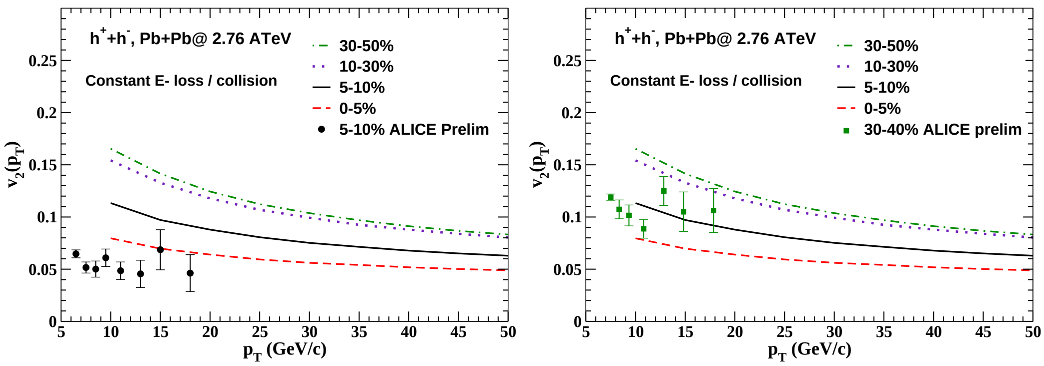

Figure 4.13: The differential azimuthal anisotropy coefficient, $v_2(p_T)$, of charged hadrons calculated in the complete coherence regime of parton energy loss for Pb+Pb collisions at $\sqrt{s_{\text{NN}}}$= 2.76 TeV. The experimental data are adopted from the ALICE Collaboration [133].

of the system which converts the initial spatial anisotropy to the momentum anisotropy of final particles. The hydrodynamic flow also affects the particle spectra up to $p_T \sim$ 4-5 GeV/c. In addition, the recombination mechanism [29] is considered an alternative of fragmentation process of hadronization in the intermediate p_T range 3-5 GeV/c. Thus, the results presented here should be taken as indicative of anisotropy which can arise due to medium modification of the fragmentation function due to energy loss of partons.

The results of $v_2(p_T)$ of neutral pions for $p_T > 2$ GeV/c for Au+Au collisions at $\sqrt{s_{\text{NN}}}$= 200 GeV are shown in Fig. 4.12 for four centralities of collision, along with the data from PHENIX collaboration [132]. We have taken the best fit value of the energy loss parameter from earlier $R_{\text{AA}}^{\pi^0}$ analysis and calculated ϕ dependent particle spectra using $L(\phi; b)$. The theoretical results are shown over the p_T region where the corresponding mechanisms are found to work well.

Thus BH mechanism should be operating for $p_T \leq 6$ GeV/c, gives $v_2(p_T)$ increasing with p_T. However the experimental data shows the contrary behaviour. The results for LPM and complete coherence regimes of energy loss exhibits similar behaviour to the experimental data for the respective p_T region. The theoretical values of azimuthal anisotropy are larger by a factor of 2 for most central collisions (0-10%) and quite reasonable for less central collisions (50-60%). It indicates the description of geometry dependent momentum anisotropy of particles at large p_T becomes more appropriate for peripheral collisions.

Next we have calculated $v_2(p_T)$ of charged hadrons in the complete coherence regime of energy loss for Pb+Pb collisions at $\sqrt{s_{\rm NN}}$= 2.76 TeV for four centralities of collision; 0-5%, 5-10%, 10-30%, 30-50%. The preliminary results from the ALICE collaboration are also given for comparison [133]. The energy loss parameter is taken from the $R^{ch}_{\rm AA}$ analysis. We have noted the theoretical results for $p_T \geq 10$ GeV/c are over predicting the data by a factor of 2 for most central collisions (5-10%) and about factor of 1.5 for mid central (30-40%) collisions (Fig. 4.13).

One immediate reason of the discrepancy between theory and experiment is the use of uniform density for the colliding nuclei. A WoodsSaxon density profile for the colliding nuclei would certainly reduce the difference in the path lengths for the partons travelling along the reaction plane and perpendicular to it, thus reduce v_2. In addition, introducing an realistic expansion of the medium would reduce the momentum anisotropy of hadrons, particularly at low p_T.

4.6 Nuclear suppression and azimuthal anisotropy of prompt photons

The high energy prompt photons created in the early stages of heavy ion collisions constitutes unique signal of the interactions between quarks and gluons at short distances. The word "prompt" is used to identify the class of photons which do not come from the decay of hadrons (e.g., π^0, η, etc.). This photon source is mostly dominating at higher momenta which roughly separates it from the thermal photon region. The basic mechanisms of prompt photon production at the Leading-order (LO) of strong coupling α_s are (i) quark–gluon Compton scattering (qg$\rightarrow$ qγ), (ii) quark–anti-quark annihilation (q$\bar{\text{q}}$$\rightarrow$ gγ) and (iii) collinear fragmentation from the final state quark (q$\rightarrow$ q+γ) [134]. Of these the third process is sensitive to the energy loss of the parent quark before it fragments [114, 135]. This will also give rise to azimuthal anisotropy of prompt photons at large p_T. However prompt photons created in the processes (i) and (ii) do not contribute to azimuthal anisotropy.

We have calculated the invariant yield of prompt photons for proton-proton collisions at $\sqrt{s}$= 200 GeV using the code INCNLO. The results are shown in Fig. 4.14 for three different scales Q= $0.5k_T$, $1.0k_T$, $2.0k_T$. We have used $CTEQ4M$ PDF and BFG-II parton to photon fragmentation function for this study. It is found that our results are consistent with the data from PHENIX [136] and also with earlier calculations (see Ref. [136]). For the rest of the calculations we have used a common scale $Q = 1.0k_T$. We have not performed calculations at the LHC energy since no baseline pp data was available at that time.

The code is suitably modified while performing calculations for Au-Au collisions at the RHIC energy. We include the energy loss suffered by the quarks and nuclear shadowing as before. The isospin of the colliding nucleons is also properly accounted in our formalism which is essential for the photon calculation.

In Fig. 4.15 , we have shown the results of nuclear modification of prompt photon production for the three energy loss mechanisms. The energy loss coefficients are obtained from the earlier analysis of neutral pion suppression for Au+Au collisions at 200A GeV. We have shown the theoretical results over the region where the respective

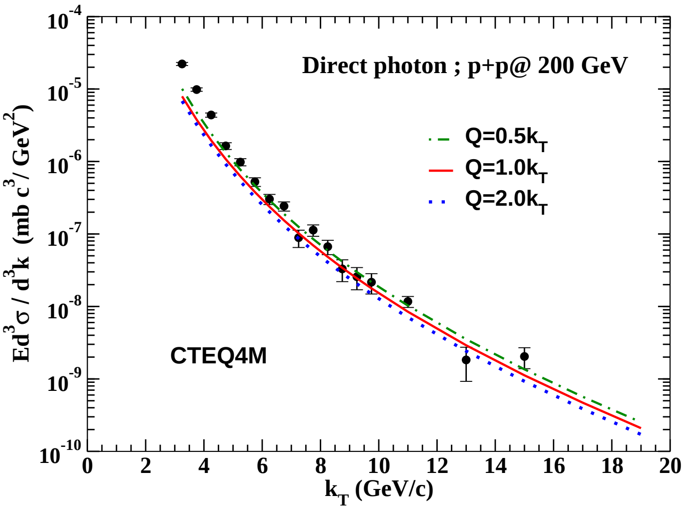

Figure 4.14: A comparison of production of prompt photons in p+p collision measured by the PHENIX collaboration [136] at $\sqrt{s_{\mathrm{NN}}}$ = 200 GeV with NLO pQCD calculations.

mechanisms are found to work. Our results are found to be in fair agreement with the preliminary data from PHENIX collaboration [137] beyond $p_T \geq 10$ GeV/c where the prompt photon source is dominant. Of course we do realize that for lower k_T, several other mechanisms like jet-conversion [138], induced bremsstrahlung [139] and thermal production [65, 66] will contribute. We find the three energy loss mechanisms behave in a similar way which is contrary to hadron suppression. We shall discuss this feature later.

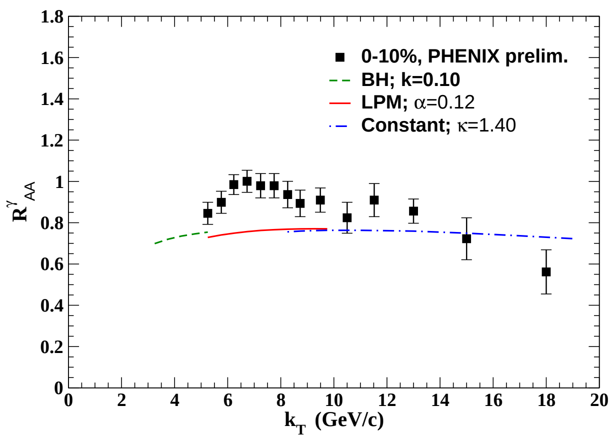

Figure 4.15: Nuclear suppression of hard photons calculated using BH, LPM, and constant energy loss per collision for Au+Au (0-10%) collisions at $\sqrt{s_{\mathrm{NN}}}$=200 GeV. The data points are taken from Ref. [137]

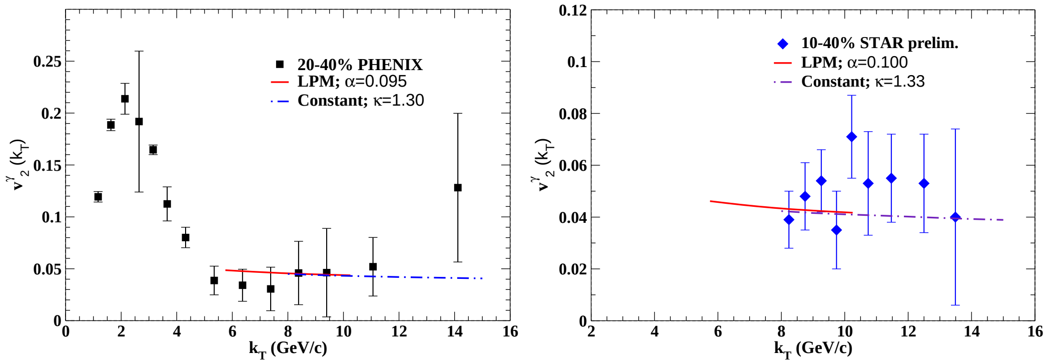

Figure 4.16: The differential azimuthal anisotropy coefficient v_2^γ of direct photons calculated with two schemes of parton energy loss for Au+Au collisions at $\sqrt{s_{\rm NN}}$= 200 GeV along with experimental data from the PHENIX [140] (left panel) and the STAR [141] (right panel) collaborations.

Next we calculate the differential azimuthal anisotropy coefficient $v_2^\gamma(k_T)$ of prompt photons originated due to azimuthal variation of path length of the parent quark. Recalling the fact that elliptic flow of direct photons for $k_T \leq 5$ GeV/c is an outcome of collective flow of thermal partons developed at early times [25]. In Fig. 4.16 the results for $v_2^\gamma(k_T)$ are shown for LPM and complete coherence regimes of parton energy loss for two centrality classes (20-40% and 10-40%) and compared them with the recent measurements from the PHENIX [140] and the STAR [141] collaborations. We make no further adjustments of the energy loss parameters obtained earlier.

We see that our theoretical curves agrees well with the experimental data for $k_T \geq$ 6 GeV/c for both cases. Next we discuss the similar pattern of three energy loss mechanisms. The energy loss parameters are extracted from the earlier study of nuclear modification of hadron production at large p_T, which is sensitive to the energy loss of quarks and gluons both. However prompt photon production is only affected due to energy loss of quarks. Thus the possible reason could be the dominant contribution of quarks to the hadron as well as the photon production at large p_T, which is then properly sampled in our calculation. One could study the flavor dependence of parton energy loss by fixing the quark energy loss from the direct photon spectra and then fix the gluon energy loss from the hadronic spectra.

Chapter 5

Jet-tagged back-scattering photons from QGP

5.1 Introduction

The measurement of direct photons and dileptons holds great promise for the characterization of matter created in high energy nuclear collisions. The large mean free path ($\sim$ 100 fm) of these electromagnetic radiations which is an order of magnitude larger than the transverse size of the colliding nuclei, enable them to carry information from the earliest stages of collision. Due to electromagnetic coupling with matter ($\alpha_{em}/\alpha_s \sim 10^{-2}$), they are least scattered in the surrounding medium and carry the information undistorted to the detectors [142]. The present discussion is mainly centered on direct photon production. Theoretical efforts over the last few decades have been spent to identify several sources of direct photon which constitute the entire spectrum observed in experiment. They include:

- Prompt photons originated from the initial hard scatterings between the beam partons and from fragmentation of large momentum jets [134, 143]. The basic mechanisms of prompt photon production at the Leading Order of strong coupling α_s are (i) quark–gluon Compton scattering (qg$\rightarrow$ qγ), (ii) quark–anti-quark annihilation (q$\bar{\text{q}}$$\rightarrow$ gγ) and (iii) bremsstrahlung radiation from the final state parton (q(g)$\rightarrow$ q(g)+γ). The photons produced through the processes (i) and (ii) are called "direct"photons whereas photons originated from the process (iii) are called "fragmentation"photons. They are found to be sensitive to the parton distribution

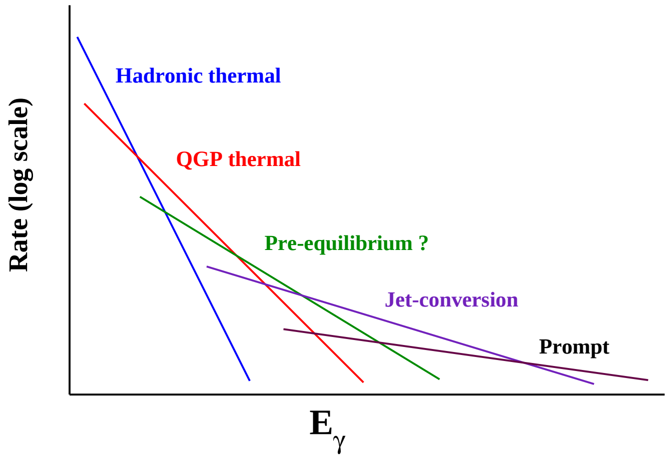

Figure 5.1: Schematic plot of production rate vs.energy for different direct photon sources.

of the colliding nucleons and the QCD scale parameter Λ_{QCD} [144, 145].

- Pre-equilibrium photons are originated in the phase when the initial state partons undergo multiple re-scatterings but have not thermalized yet. By using parton cascade model, the contribution has been evaluated and found to dominate at lower transverse momenta [146]. The photon momentum (p_T) depends on the momentum scale (Q^2) of collision not on the temperature of system, which provides valuable information about pre-equilibrium dynamics [147].

- Photons produced due to interaction of high energy jets with thermalized QGP are commonly known as Jet-medium photons. They are calculated either from elastic scattering ($2 \rightarrow 2$) of partons [138] or inelastic bremsstrahlung from a fast quark [139]. This particular source has been found to dominate intermediate p_T region; $3-5$ GeV at the RHIC and LHC energies. The photon momentum is strongly correlated with parent jet momentum and the yield is sensitive to the temperature of the plasma.

- The electromagnetic radiation emitted from an equilibrated partonic or hadronic matter are called thermal photons. The production mechanism of thermal photon has been discussed earlier in Chapter 2. It is noted that while the photon yield of other sources follows a power-law in p_T, thermal photon yield falls exponentially with p_T. Thus the inverse slope parameter of thermal photon p_T spectra is a measure of average temperature of the thermalized medium produced in the collisions. The temperature extracted from the slope of recent LHC direct photon measurement is $\sim 304 \pm 51$ MeV [148].

The photon sources discussed in the above paragraphs roughly follow a hierarchy of transverse momenta, from high to low p_T (see Fig. 5.1). However it is a formidable task in experiment to separate out each particular contribution, in fact to distinguish direct photons from the overwhelming background of low momentum photons come from the decay of π^0 and η mesons. The present study aims to identify the jet-medium photon contribution by employing the correlation with large momentum jets. It will be argued later that this effectively rids the sample of photons from thermal and pre-equilibrium sources and vastly reduces the background from fragmentation prompt photons. Further the jet-medium photons are found to offer complementary measure of parton energy loss independent of hadronic measurement.

5.2 Production rate of jet-medium photons in QGP

Jet-medium photons produced through the elastic Compton ($qg \to q\gamma$) or annihilation ($q\overline{q} \to \gamma g$) scattering was first estimated in Ref. [138]. We find the cross-section of these processes is sharply peaked at backward angles i.e., the produced photon approximately carries the same momentum of the initial quark or anti-quark. This phenomenon is called "back-scattering"of photons, quite well-known in electrodynamics The low energy photon beams (~ 1 eV) are Compton back-scattered form a high energy electron beam (~ 100 MeV) to produce high energy laser beam of few tens of MeV [149] at HIGS research facility of Duke free electron laser laboratory. The QCD analogue used here is a thermal gluon of energy ~ 200 MeV scattering off a fast quark ~ 10 GeV to produce a hard photon of few GeV. In the following subsections, we have outlined the rate of production of back-scattering photons due to Compton and annihilation processes in QGP at Leading Order of strong coupling (α_s) [32].

5.2.1 Photon production by Compton scattering

The color independent part of the cross-section for $(qg \to q\gamma)$ is related to the process $(q\gamma \to q\gamma)$ as;

$$\begin{aligned} E_\gamma \frac{d\sigma}{d\vec{p_\gamma}}(qg \to q\gamma) &= (g_s/e_q)^2 E_\gamma \frac{d\sigma}{d\vec{p_\gamma}}(q\gamma \to q\gamma) \\ &= \frac{\alpha_s}{\alpha_{em}}(\frac{e}{e_q})^2 E_\gamma \frac{d\sigma}{d\vec{p_\gamma}}(q\gamma \to q\gamma), \end{aligned} \tag{5.1}$$

where $\alpha_s = g_s^2/4\pi$ and $\alpha_{em} = e^2/4\pi$. e_q is the fractional charge of the quark. We write

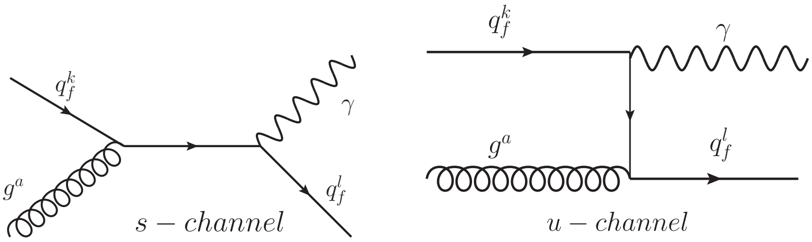

Figure 5.2: Feynman diagrams for the Compton process in QCD.

the Mandelstam variables for the process $(q + g \to q + \gamma)$,

$$\begin{aligned} s &= (p_q + p_g)^2, \\ t &= (p_g - p_\gamma)^2, \\ u &= (p_q - p_\gamma)^2. \end{aligned} \tag{5.2}$$

Using the above variables, the differential cross-section for $(q\gamma \to q\gamma)$ is given by [150]:

$$\frac{d\sigma}{dt} = (\frac{e_q}{e})^4 \frac{8\pi\alpha_{em}^2}{(s-m^2)^2}\left\{(\frac{m^2}{s-m^2} + \frac{m^2}{u-m^2})^2 + (\frac{m^2}{s-m^2} + \frac{m^2}{u-m^2}) - \frac{1}{4}(\frac{s-m^2}{u-m^2} + \frac{u-m^2}{s-m^2})\right\} \tag{5.3}$$

In the small quark mass limit $(m \to 0)$; only the last term dominates the cross-section.

Thus using Eqs. (5.1) and (5.3), the differential cross section for QCD Compton scattering in the small quark mass limit is:

$$\frac{d\sigma^{Comp.}}{dt}(qg \to q\gamma) = -(\frac{e_q}{e})^2 \frac{2\pi\alpha_s\alpha_{em}}{(s-m^2)^2}\left\{(\frac{s-m^2}{u-m^2} + \frac{u-m^2}{s-m^2})\right\}. \tag{5.4}$$

For a given center of mass energy $(\sqrt{s})$, we find the cross section becomes large for small values of $(u - m^2)$;

$$|u - m^2| = |(p_q - p_\gamma)^2 - m^2|$$

$$
\begin{aligned}
&= |m^2 + 0 - 2p_q \cdot p_\gamma| \\
&\simeq 2E_\gamma E_q - |\vec{p_\gamma}||\vec{p_q}|cos\theta_{\gamma q} \\
&\simeq 2E_\gamma(E_q - |\vec{p_q}|cos\theta_{\gamma q}) \qquad (5.5)
\end{aligned}
$$

Thus $|u - m^2|$ is minimum when $\theta_{\gamma q}$= 0 i.e., the photon momentum $\vec{p_\gamma}$ is collinear to

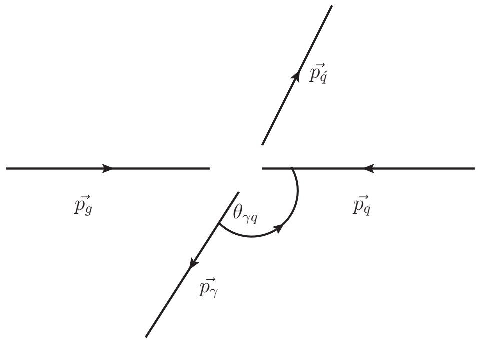

Figure 5.3: Kinematics of the Compton process in center of mass frame.

$\vec{p_q}$.

$$\vec{p_\gamma} \approx \vec{p_q} \qquad \text{Backward scattering} \qquad (5.6)$$

Similarly, it can also be shown that the 4-momentum of the photon is approximately same as the 4-momentum of the quark,

$$p_\gamma \approx p_q. \qquad (5.7)$$

They are called Compton back-scattering photons. The color independent part of the back-scattering photon cross section is approximated as

$$E_\gamma \frac{d\sigma^{Comp.}}{d\vec{p_\gamma}} \approx \sigma^C_{tot} E_\gamma \delta(\vec{p_\gamma} - \vec{p_q}), \qquad (5.8)$$

where σ^C_{tot} is the color independent part of the total Compton scattering cross section; obtained by integrating Eq. (5.4) over allowed range of t.

• ***The upper and lower limit of t:***

We define the center of mass energy for the reaction $qg \to q\gamma$

$$\sqrt{s} = E^*_q + E^*_g, \qquad (5.9)$$

with $|\vec{p^*_q}| = |\vec{p^*_g}| = E^*_g$; $|p^*_q| = \sqrt{E^*_q - m^2}$.

Thus,

$$\sqrt{s} = \sqrt{E_g^{*2} + m^2} + E_g^*$$
$$\Rightarrow E_g^* = \frac{s - m^2}{2\sqrt{s}} \tag{5.10}$$

Similarly,

$$E_\gamma^* = \frac{s - m^2}{2\sqrt{s}}. \tag{5.11}$$

$$t = (p_g - p_\gamma)^2 = -2E_g^* E_\gamma^* (1 - cos\theta_{\gamma^* g^*}), \tag{5.12}$$

where the $(*)$ corresponds to the quantities measured in center of mass frame. The upper limit of t corresponds to $\theta_{\gamma^* g^*} = 0$.

$$t_{up} = 0 \tag{5.13}$$

The lower limit corresponds to $\theta_{\gamma^* g^*} = \pi$

$$t_{low} = -4E_g^* E_\gamma^* = \frac{-4(s - m^2)^2}{4s} = \frac{-(s - m^2)^2}{s} \tag{5.14}$$

Now we briefly outline the steps of calculation of rate of production of photons in the Compton process. Let us consider a quark of flavor f with color index (k) scatters with a gluon of color a, yields a photon and a quark with color index (l) and flavor f.

$$q_f^k + g^a = \gamma + q_f^l \tag{5.15}$$

The number of photons emitted per unit time

$$\frac{dN^\gamma}{dt} = N_s N_g \sum_{f=1}^{n_f} \sum_{k=1}^{3} \sum_{l=1}^{3} \sum_{a=1}^{8} \left| \frac{\lambda_{kl}^a}{2} \right|^2 \times \frac{1}{(2\pi)^6} \int d^3x\, d^3p_g\, d^3p_q$$
$$f_g(\vec{p_g}) f_q(\vec{p_q}) [1 - f_q(\vec{p_q'})] \sigma_{tot}^C(s) v_{qg}, \tag{5.16}$$

where N_s,N_g are the quark, gluon spin degeneracies respectively. λ_{kl}^a are the standard Gell-Mann matrices. $f_q(\vec{p_q})$ and $f_g(\vec{p_g})$ are the momentum distribution function of the incoming quark and gluon. $f_q(\vec{p_q'})$ gives the probability of production of a quark with momentum $\vec{p_q'}(= \vec{p_q} + \vec{p_g} - \vec{p_\gamma})$ in the final state. Thus $[1 - f_q(\vec{p_q'})]$ is the Pauli blocking factor, reduces the probability of occupying the same state. $v_{qg} = |v_q - v_g|$ is the relative velocity of the incoming partons.

Using the properties of Gell-Mann matrices we get;

$$\sum_{k=1}^{3}\sum_{l=1}^{3}\sum_{a=1}^{8}\left|\frac{\lambda^a_{kl}}{2}\right|^2 = \frac{8\times 2}{4} = 4. \tag{5.17}$$

Thus Eq. 5.16 becomes

$$\frac{dN^\gamma}{dt} = 4N_sN_g\sum_{f=1}^{n_f}\frac{1}{(2\pi)^6}\int d^3x\, d^3p_g\, d^3p_q f_g(\vec{p_g})f_q(\vec{p_q})\,[1-f_q(\vec{p_q})]\sigma^C_{tot}(s)v_{qg}. \tag{5.18}$$

The photon cross section can be written as sum over all momentum states

$$\sigma^C_{tot}(qg\to q\gamma) = \int E_\gamma \frac{d\sigma^{Comp.}}{d\vec{p_\gamma}}(qg\to q\gamma)\frac{d\vec{p_\gamma}}{E_\gamma}. \tag{5.19}$$

Inserting the above in (Eq. 5.18), we get the rate of photon production due to Compton process

$$\begin{aligned} E_\gamma\frac{dN_\gamma}{d^4xd\vec{p_\gamma}} = 4N_sN_g\sum_{f=1}^{n_f}\frac{1}{(2\pi)^6}\int d^3p_g\, d^3p_q f_g(\vec{p_g})f_q(\vec{p_q})[1-f_q(\vec{p_q})] \\ \times E_\gamma\frac{d\sigma^{Comp.}}{d\vec{p_\gamma}}v_{qg} \end{aligned} \tag{5.20}$$

It can be shown from relativistic kinematics that in a collinear collision between A and B, the quantity $E_AE_B|V_A-V_B|$ is Lorentz invariant.

$$\begin{aligned} E_AE_B|V_A-V_B| &= [(p_A\cdot p_B)^2 - m_A^2m_B^2]^{1/2} \\ &= [(s-p_A^2-p_B^2)^2/4 - m_A^2m_B^2]^{1/2} \end{aligned} \tag{5.21}$$

Thus the relative velocity v_{qg} becomes

$$\begin{aligned} v_{qg} &= \frac{\sqrt{(s-p_q^2-p_g^2)/4 - m^2m_g^2}}{E_qE_g} \\ &= \frac{(s-m^2)}{2E_qE_g} \end{aligned} \tag{5.22}$$

Using Eqs.(5.8) and (5.22), we get

$$\begin{aligned} E_\gamma\frac{dN_\gamma}{d^4xd\vec{p_\gamma}} = 4N_sN_g\sum_{f=1}^{n_f}\frac{1}{(2\pi)^6}\int d^3p_g\, d^3p_q f_g(\vec{p_g})f_q(\vec{p_q})[1-f_q(\vec{p_q})] \\ \times E_\gamma\delta(\vec{p_\gamma}-\vec{p_q})\sigma^C_{tot}(s)\frac{(s-m^2)}{2E_qE_g} \end{aligned} \tag{5.23}$$

The integration over p_q vanishes due to delta function and $\vec{p_q} = \vec{p_g}$. Thus Eq. 5.23 becomes

$$E_\gamma \frac{dN_\gamma}{d^4x d\vec{p_\gamma}} = \frac{4N_s N_g E_\gamma}{(2\pi)^6} \sum_{f=1}^{n_f} \int_{\vec{p_\gamma}=\vec{p_q}} d^3p_g f_g(\vec{p_g}) f_q(\vec{p_\gamma})[1 - f_q(\vec{p_g})]$$
$$\times \sigma^C_{tot}(s) \frac{(s-m^2)}{2E_\gamma E_g} \quad (5.24)$$

Assuming Fermi-Dirac distribution for the quark and Bose-Einstein distribution for the gluon and integrating over the gluon phase space ($s/4E_\gamma < p_g < \infty$), we ultimately get the rate of back-scattered photons for ($qg \to q\gamma$):

$$E_\gamma \frac{dN_\gamma}{d^4x d\vec{p_\gamma}} = \frac{N_s N_g \alpha_{em} \alpha_s}{32\pi^2} f_q(\vec{p_\gamma}) T^2 \sum_{f=1}^{n_f} (\frac{e_q}{e})^2 \left\{ \ln(\frac{4E_\gamma T}{m^2}) + C_{comp} \right\}. \quad (5.25)$$

Including the process ($\overline{q}g \to q\gamma$), the total rate of Compton back-scattered photons at Leading Order strong coupling (α_s) is given by:

$$E_\gamma \frac{dN_\gamma^{Comp.}}{d^4x d\vec{p_\gamma}} = \frac{N_s N_g \alpha_{em} \alpha_s}{32\pi^2} [f_q(\vec{p_\gamma}) + f_{\overline{q}}(\vec{p_\gamma})] T^2 \sum_{f=1}^{n_f} (\frac{e_q}{e})^2 \left\{ \ln(\frac{4E_\gamma T}{m^2}) + C_{comp} \right\} \quad (5.26)$$

5.2.2 Photon production by annihilation

The color independent part of the differential cross section for ($q\overline{q} \to \gamma g$) is related to the differential cross section of the process ($q\overline{q} \to \gamma\gamma$) as,

$$\begin{aligned} E_\gamma \frac{d\sigma^{ann}}{d\vec{p_\gamma}}(q\overline{q} \to \gamma g) &= (g_s/e_q)^2 E_\gamma \frac{d\sigma}{d\vec{p_\gamma}}(q\overline{q} \to \gamma\gamma) \\ &= \frac{\alpha_s}{\alpha_{em}} (\frac{e}{e_q})^2 E_\gamma \frac{d\sigma}{d\vec{p_\gamma}}(q\overline{q} \to \gamma\gamma), \end{aligned} \quad (5.27)$$

The differential cross section of photon production for ($q\overline{q} \to \gamma\gamma$), averaged over initial state spins and summed over final state polarizations, is given by ([150]):

$$\frac{d\sigma}{dt} = (\frac{e_q}{e})^4 \frac{8\pi\alpha_{em}^2}{s(s-4m^2)} \left\{ (\frac{m^2}{t-m^2} + \frac{m^2}{u-m^2})^2 + (\frac{m^2}{t-m^2} + \frac{m^2}{u-m^2}) - \frac{1}{4}(\frac{t-m^2}{u-m^2} + \frac{u-m^2}{t-m^2}) \right\} \quad (5.28)$$

In the small quark mass limit ($m \to 0$), the last term dominates the cross section. Using Eqs. 5.27 and 5.28 the differential cross section of ($q\overline{q} \to \gamma g$) in small quark mass limit:

$$\frac{d\sigma^{ann}}{dt} = -(\frac{e_q}{e})^2) \frac{2\pi\alpha_{em}\alpha_s}{s(s-4m^2)} \left\{ (\frac{t-m^2}{u-m^2} + \frac{u-m^2}{t-m^2}) \right\}, \quad (5.29)$$

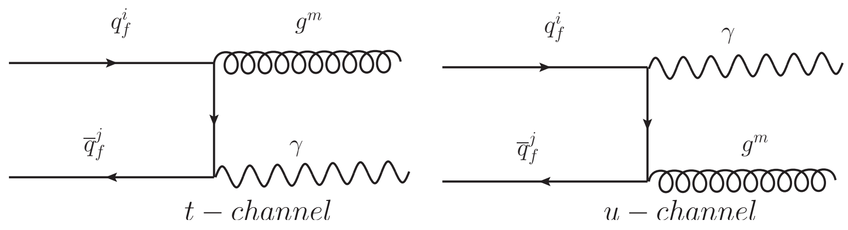

Figure 5.4: Feynman diagrams for the annihilation process in QCD.

where the Mandelstam variables for the process $(q + \overline{q} \rightarrow \gamma g)$ are:

$$\begin{aligned} s &= (p_q + p_{\overline{q}})^2, \\ t &= (p_q - p_\gamma)^2, \\ u &= (p_{\overline{q}} - p_\gamma)^2. \end{aligned} \tag{5.30}$$

For a given value of $\sqrt{s}$, we find cross section of the annihilation process becomes maximum, when $|t - m^2|$ or $|u - m^2|$ is minimum.

$$\begin{aligned} |t - m^2| &= |(p_q - p_\gamma)^2 - m^2| \\ &= |m^2 + 0 - 2p_q \cdot p_\gamma - m^2| \\ &\simeq 2E_\gamma E_q - |\vec{p_\gamma}||\vec{p_q}|cos\theta_{\gamma q} \\ &\simeq 2E_\gamma(E_q - |\vec{p_q}|cos\theta_{\gamma q}) \end{aligned} \tag{5.31}$$

$|t-m^2|$ is minimum when $\theta_{\gamma q} = 0$ i.e., photon momentum $(\vec{p_\gamma})$ aligns along the direction of quark momentum $(\vec{p_q})$.

$$\vec{p_\gamma} \approx \vec{p_q} \qquad \text{Forward scattering} \tag{5.32}$$

Similarly,

$$\begin{aligned} |u - m^2| &= |(p_{\overline{q}} - p_\gamma)^2 - m^2| \\ &\simeq 2E_\gamma(E_q - |\vec{p_{\overline{q}}}|cos\theta_{\gamma\overline{q}}). \end{aligned} \tag{5.33}$$

$|u-m^2|$ is minimum when $\theta_{\gamma\overline{q}} = 0$ i.e., photon momentum $(\vec{p_\gamma})$ aligns along the direction of anti-quark momentum $(\vec{p_{\overline{q}}})$.

$$\vec{p_\gamma} \approx \vec{p_{\overline{q}}} \qquad \text{Backward scattering} \tag{5.34}$$

We have seen $d\sigma^{ann}/dt$ has two peaks and the photon is most likely to be produced in these two directions. Thus the color independent part of the cross section can be approximated:

$$E_\gamma \frac{d\sigma^{ann}}{dp_\gamma}(q\overline{q} \to \gamma g) \approx \sigma^A_{tot}(s)\frac{1}{2}\, E_\gamma[\delta(\vec{p_\gamma} - \vec{p_q}) + \delta(\vec{p_\gamma} - \vec{p_{\overline{q}}})], \tag{5.35}$$

where $\sigma^A_{tot}(s)$ is the total annihilation cross section is obtained by integrating Eq. 5.29 over the allowed ranges of t.

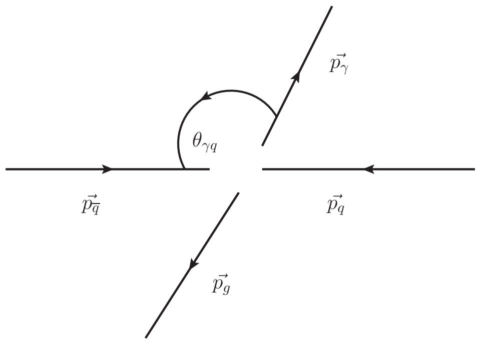

Figure 5.5: Kinematics of the annihilation process in center of mass frame.

• ***The upper and lower limit of t:***

We define the center of mass energy for the reaction $q\overline{q} \to \gamma g$

$$\sqrt{s} = E^*_q + E^*_{\overline{q}} = E^*_\gamma + E^*_g, \tag{5.36}$$

with $|\vec{p^*_q}| = |\vec{p^*_{\overline{q}}}|$ and $|\vec{p^*_\gamma}| = |\vec{p^*_g}|$. Thus,

$$E^*_q = \frac{\sqrt{s}}{2} \quad \text{and} \quad E^*_\gamma = \frac{\sqrt{s}}{2}. \tag{5.37}$$

$$t = (p_q - p_\gamma)^2 = m^2 - 2E^*_\gamma(E^*_q - |\vec{p^*_q}|cos\theta^*_{\gamma q}) \tag{5.38}$$

The upper limit of t corresponds to $\theta^*_{\gamma q}$ =0

$$\begin{aligned} t_{up} &= m^2 - 2E_\gamma\left(\frac{\sqrt{s}}{2} - \sqrt{(\frac{\sqrt{s}}{2})^2 - m^2}\right) \\ &= m^2 - E_\gamma\left(\sqrt{s} - \sqrt{(s-4m^2)}\right) \\ &= m^2 - \frac{\sqrt{s}}{2}\left(\sqrt{s} - \sqrt{(s-4m^2)}\right) \end{aligned} \tag{5.39}$$

The lower limit corresponds to $\theta^*_{\gamma q} = \pi$

$$t_{low} = m^2 - \frac{\sqrt{s}}{2}\left(\sqrt{s} + \sqrt{(s-4m^2)}\right) \tag{5.40}$$

Next we briefly describe the steps of calculation of photon production rate due to annihilation process. Let us consider an anti-quark of flavor f, color j annihilates with a quark of same flavor, color i, yields a photon and a gluon with color index m.

$$q^i_f + \overline{q}^j_f \to \gamma + g^m \tag{5.41}$$

The number of photons produced per unit time is given by;

$$\frac{dN^\gamma}{dt} = N_s^2 \sum_{f=1}^{n_f}\sum_{i=1}^{3}\sum_{j=1}^{3}\sum_{m=1}^{8}\left|\frac{\lambda^m_{ij}}{2}\right|^2 \times \frac{1}{(2\pi)^6}\int d^3x\, d^3p_q\, d^3p_{\overline{q}}$$
$$f_q(\vec{p_q})f_{\overline{q}}(\vec{p_{\overline{q}}})[1+f_g(\vec{p_g})]\,\sigma^{ann}_{tot}(s)v_{q\overline{q}},$$

where $f_q(\vec{p_q})$ and $f_{\overline{q}}(\vec{p_{\overline{q}}})$ are the momentum distribution function of the quark and anti-quark respectively. $f_g(\vec{p_g})$ is the occupation probability of the gluon having momentum $\vec{p_g} = (\vec{p_q} + \vec{p_{\overline{q}}} - \vec{p_\gamma})$ in the final state. As the gluon is produced simultaneously with the photon, we have an enhancement factor $[1+f_g(\vec{p_g})]$ due to Bose-Einstein statistics. $v_{q\overline{q}} = |\vec{v_q} - \vec{v_{\overline{q}}}|$ is the relative velocity between the incoming partons.

Summed over color matrices (Eq. 5.17), we get

$$\frac{dN^\gamma}{dt} = 4N_s^2 \sum_{f=1}^{n_f}\left|\frac{\lambda^m_{ij}}{2}\right|^2 \times \frac{1}{(2\pi)^6}\int d^3x\, d^3p_q\, d^3p_{\overline{q}}$$
$$f_q(\vec{p_q})f_{\overline{q}}(\vec{p_{\overline{q}}})[1+f_g(\vec{p_g})]\,\sigma^{A}_{tot}(s)v_{q\overline{q}},$$

The color independent annihilation cross section $\sigma^A_{tot}(s)$ can be written as sum over all photon momentum:

$$\sigma^A_{tot}(q\overline{q}\to\gamma g) = \int E_\gamma \frac{d\sigma^{ann}}{d\vec{p_\gamma}}(q\overline{q}\to\gamma g)\frac{d\vec{p_\gamma}}{E_\gamma}. \tag{5.42}$$

Inserting Eq. 5.42 in Eq. 5.42, we get the rate of production of annihilation photons,

$$E_\gamma \frac{dN}{d^4x d^3p_\gamma} = \frac{4N_s^2}{(2\pi)^6}\sum_{f=1}^{n_f}\int d^3p_q\, d^3p_{\overline{q}}\, f_q(\vec{p_q})f_{\overline{q}}(\vec{p_{\overline{q}}})[1+f_g(\vec{p_g})]\,E_\gamma\frac{d\sigma^{ann}}{d\vec{p_\gamma}}(q\overline{q}\to\gamma g)v_{q\overline{q}} \tag{5.43}$$

$v_{q\overline{q}}$ can be expressed as (see eq. 5.21):

$$\begin{aligned} v_{q\overline{q}} &= \frac{1}{E_q E_{\overline{q}}}[(p_q \cdot p_{\overline{q}})^2 - m_q^2 m_{\overline{q}}]^{\frac{1}{2}} \\ &= \frac{1}{E_q E_{\overline{q}}}[(s - p_q^2 - (p_{\overline{q}})^2/4 - (m^2)^2]^{\frac{1}{2}} \\ &= \frac{\sqrt{s(s-4m^2)}}{2E_q E_{\overline{q}}} \end{aligned} \quad (5.44)$$

Substituting Eq. (5.35) and (5.44) in Eq. 5.43, we have

$$E_\gamma \frac{dN}{d^4x d^3p_\gamma} = \frac{4N_s^2}{(2\pi)^6}\sum_{f=1}^{n_f}\int d^3p_q\, d^3p_{\overline{q}}\, f_q(\vec{p_q}) f_{\overline{q}}(\vec{p_{\overline{q}}})[1 + f_g(\vec{p_g})]$$
$$\times \sigma_{tot}^A(s)\frac{E_\gamma}{2}[\delta(\vec{p_\gamma} - \vec{p_q}) + \delta(\vec{p_\gamma} - \vec{p_{\overline{q}}})]\, \frac{\sqrt{s(s-4m^2)}}{2E_q E_{\overline{q}}} \quad (5.45)$$

The delta functions kill the integrations over p_q or $p_{\overline{q}}$ which yields

$$\begin{aligned} E_\gamma \frac{dN}{d^4x d^3p_\gamma} &= \frac{4N_s^2}{(2\pi)^6}\frac{E_\gamma}{2}\sum_{f=1}^{n_f}\int_{\vec{p_\gamma}=\vec{p_q}} d^3p_{\overline{q}}\, f_q(\vec{p_\gamma}) f_{\overline{q}}(\vec{p_{\overline{q}}})[1 + f_g(\vec{p_{\overline{q}}})]\, \sigma_{tot}^A(s)\frac{\sqrt{s(s-4m^2)}}{2E_\gamma E_{\overline{q}}} \\ &+ \int_{\vec{p_\gamma}=\vec{p_{\overline{q}}}} d^3p_q f_q(\vec{p_q})\, f_{\overline{q}}(\vec{p_\gamma})[1 + f_g(\vec{p_q})]\sigma_{tot}^A(s)\frac{\sqrt{s(s-4m^2)}}{2E_q E_\gamma} \end{aligned} \quad (5.46)$$

The above equation can also be written as;

$$\begin{aligned} E_\gamma \frac{dN}{d^4x d^3p_\gamma} &= \frac{4N_s^2}{2(2\pi)^6}\sum_{f=1}^{n_f}\int_{\vec{p_\gamma}=\vec{p_q}} d^3p_{\overline{q}}\, f_q(\vec{p_\gamma}) f_{\overline{q}}(\vec{p_{\overline{q}}})[1 + f_g(\vec{p_{\overline{q}}})]\, \sigma_{tot}^A(s)\frac{\sqrt{s(s-4m^2)}}{2E_{\overline{q}}} \\ &+ (q \leftrightarrow \overline{q}) \end{aligned} \quad (5.47)$$

Assuming Fermi-Dirac distribution for the anti-quark and Bose-Einstein distribution for the gluon, we integrate over $p_{\overline{q}}$ in the limit $(s/4E_\gamma < p_{\overline{q}} < \infty)$ and use the relativistic approximation $s \gg 4m^2$. Thus the Eq. 5.47 becomes;

$$E_\gamma \frac{dN_\gamma^{ann}}{d^4x d\vec{p_\gamma}} = \frac{4N_s^2\alpha_{em}\alpha_s}{32\pi^2} f_q(\vec{p_\gamma})T^2 \sum_{f=1}^{n_f}(\frac{e_q}{e})^2\left\{\ln(\frac{4E_\gamma T}{m^2}) + C_{ann}\right\} \quad (5.48)$$
$$+ \quad (q \leftrightarrow \overline{q}) \quad (5.49)$$

The above expression gives the rate of production due to annihilation at Leading Order of strong coupling (α_s).

5.2.3 Total photon production rate

Putting N_s=2, N_g=2 in Eqs. 5.26 and 5.49, we get the total rate of back-scattering photons in QGP through Compton and Annihilation processes:

$$\begin{aligned} E_\gamma \frac{dN_\gamma^{total}}{d^4x d\vec{p_\gamma}} &= E_\gamma \frac{dN_\gamma^{comp}}{d^4x d\vec{p_\gamma}} + E_\gamma \frac{dN_\gamma^{total}}{d^4x d\vec{p_\gamma}} \\ &= \frac{\alpha_{em}\alpha_s}{4\pi^2}[f_q(\vec{p_\gamma}) + f_{\overline{q}}(\vec{p_\gamma})]T^2 \sum_{f=1}^{n_f}(\frac{e_q}{e})^2 \left\{ \ln(\frac{4E_\gamma T}{m^2}) + \frac{C_{comp}+C_{ann}}{2} \right\} \end{aligned} \tag{5.50}$$

where the constants are given by C_{comp} =-1.916 and C_{ann}=-0.416.

We find the rate of photon production depends on the temperature (T) of the quark-gluon plasma and rest mass (m) of the quark. Following Ref. [151] we assume an effective thermal mass of the quark;

$$m_{th} = \frac{g_s T}{\sqrt{6}} \tag{5.51}$$

Another important study on thermal photon production in QGP by Kapusta *et al.* [152] includes a correction in the term $ln(4E_\gamma T/m_{th}^2)$, by replacing m_{th} to $\sqrt{2}m_{th}$. Thus Eq. 5.51 becomes,

$$E_\gamma \frac{dN_\gamma^{total}}{d^4x d\vec{p_\gamma}} = \frac{\alpha_{em}\alpha_s}{4\pi^2}[f_q(\vec{p_\gamma}) + f_{\overline{q}}(\vec{p_\gamma})]T^2 \sum_{f=1}^{n_f}(\frac{e_q}{e})^2 \left\{ \ln(\frac{3E_\gamma}{\alpha_s \pi T}) - 1.166 \right\}. \tag{5.52}$$

It is found that the total production rate of back-scattered photons is proportional to $T^2\ln(1/T)$, thus sensitive to the temperature of the plasma. It can also be noted that the phase space distribution of the fast quark ($f_q(\vec{p})$) enters linearly in the rate equation which leads to power-law behaviour of the momentum spectrum.

5.3 Inclusive yield and elliptic flow of jet-medium photons

The first calculation of jet-medium photons with an one dimensional boost invariant expansion of the system, shows significant contribution in the single inclusive photon spectra at intermediate p_T ($\sim$ 3–5GeV) at RHIC and LHC [138].The more recent calculation with two dimensional, boost-invariant ideal hydrodynamic expansion has also verified the earlier result [153]. This particular source has to compete with prompt hard photons at larger p_T and thermal photons at smaller p_T (Fig. 5.6). Hence it is almost

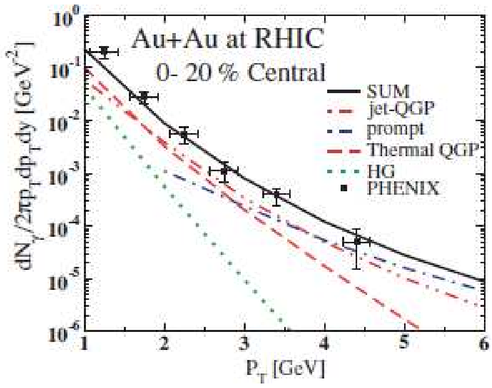

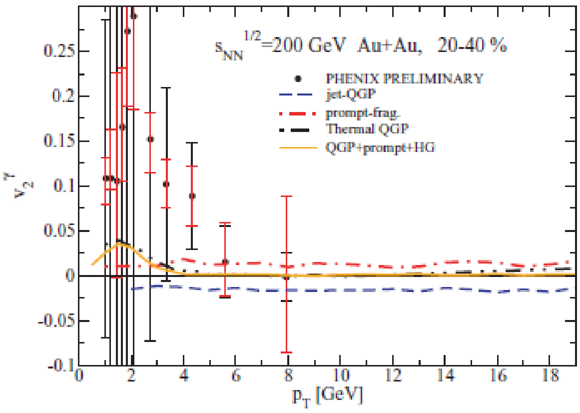

Figure 5.6: Inclusive yield and azimuthal anisotropy of direct photons for Au+Au collisions at $\sqrt{s_{\rm NN}}$= 200 GeV, calculated with ideal hydrodynamic evolution of the system [153]

.

impossible to confirm their existence from the measurement of single inclusive photon spectra alone.

The azimuthal momentum anisotropy (v_2) of jet-medium photons has been predicted to be negative [154]. This can be understood as the fast jet travels longer distance in the direction perpendicular to the reaction plane in comparison of along the reaction plane, jet-medium back-scattering would more probable to occur out-of the plane. However recent experimental measurements of direct photon v_2 at RHIC and LHC have not found any firm evidence for the existence of jet-medium photons [26, 155].

In viewing the above indeterministic situations, we propose the use of a trigger jet for an unambiguous signature of this source. It is motivated by the fact that back-scattering phenomena are induced by jets and jets are preferred to produce back-to-back in the medium. Additionally, jets are routinely measured in heavy ion experiments with good amount of precision. Thus we adopt the strategy to tag a jet of large transverse energy (E_T) and measure the direct photons on the opposite side. Only prompt direct and fragmentation photons possess such correlation with away-side jets. They will constitute the “background”of the back-scattered photon measurement. Pre-equilibrium and thermal photons do have such correlation, thus can be eliminated from the background.

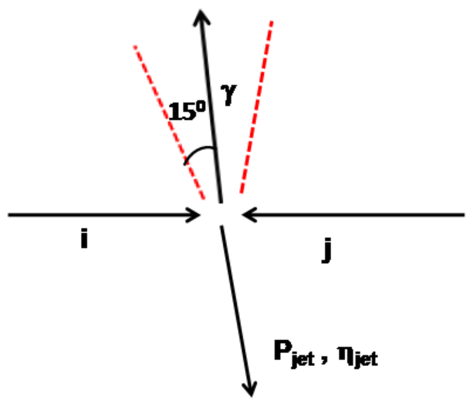

Figure 5.7: Schematic diagram of tagging a jet opposite to a prompt hard photon.

5.4 Background of jet-medium photons

For the estimation of background, we choose the trigger jet energy within a small window around E_γ and look for photons in a narrow azimuthal region ($\Delta\phi = \pm 15$ degrees) with respect to the trigger jet-axis on the opposite side. Our choice attempts to maximize the back-scattering signal and at the same time keeps jet reconstruction feasible in experiment. Ideally the jet could be represented by a Delta function peaked at E_γ. However the uncertainty in jet reconstruction in experiment limits the resolution of jet energy measurement. We have chosen trigger jet window of 5 GeV for this reason. It is expected that fragmentation photons are concentrated in the low-z region ($z = E_\gamma/E_{jet}$) [134]. Thus choosing the value of E_γ close to trigger jet energy window vastly reduces background from fragmentation and induced bremsstrahlung photons. Our calculation of background photons relies on the code JETPHOX (version:1.2.2) [156] which evaluates direct and fragmentation photon cross-section separately at Leading Order (LO) and Next-to Leading Order (NLO) accuracy for proton-proton (pp) and nucleus-nucleus (AA) collisions. The contributions are then summed to obtain the total physical cross-section. The program can implement variety of experimental cuts (kinematic, isolation) at the partonic level. JETPHOX has successfully explained the isolated prompt photon production in pp collisions at the Tevatron energy [144] and the recent LHC energy [145]. Thus it provides a safe baseline of our analysis. However we have not implemented any isolation cut in the present study for heavy ion collisions.

We have estimated the background photons in the collisions of gold nuclei at 200A

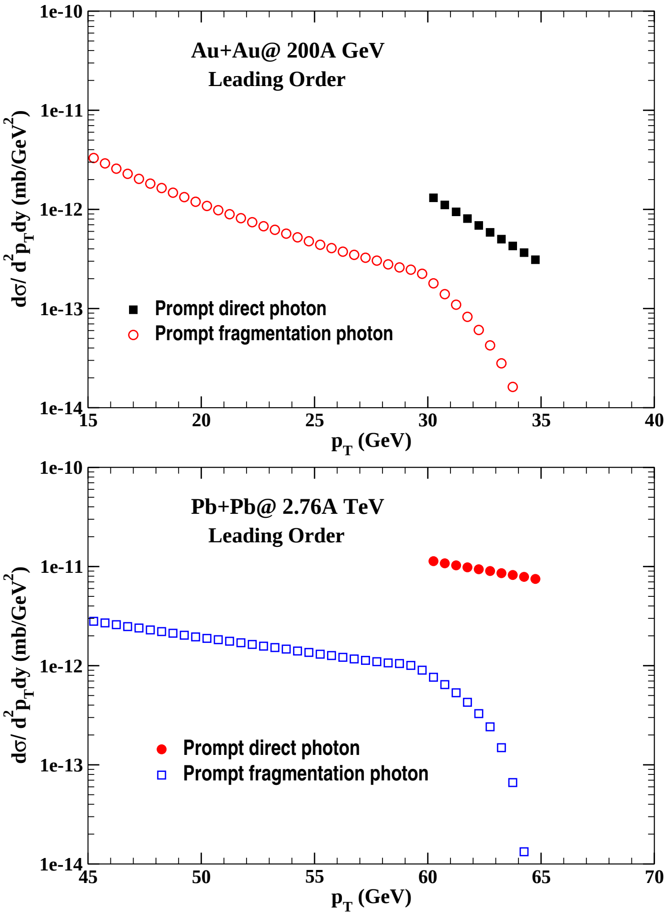

Figure 5.8: Cross-section of prompt direct and fragmentation photons for Au+Au and Pb+Pb collisions for the kinematical situations at RHIC and LHC respectively (see text for details). The result is normalized per nucelon-nucleon collision.

GeV (RHIC) and lead nuclei at 2.76A TeV (LHC) for the the typical kinematic conditions described here. The trigger jet window in rapidity-energy ($y_{jet} - E_T$) is defined as; $-1 < y_{jet} < 1$ and ($30 < E_T < 35$) GeV for RHIC and $-2 < y_{jet} < 2$ and ($60 < E_T < 65$) GeV for LHC. The hard prompt photons are measured in between the azimuthal angle 165< ϕ_j <195 degrees relative to the trigger jet and in the rapidity interval $|y_\gamma|$ <0.5 for RHIC and LHC both. We have used the CTEQ6M [157] and EPS09 [158] parameterization of parton distributions for nucleons and nuclei respectively. The parton to photon fragmentation probability is given by BFG-II fragmentation function [159]. The isospin asymmetry of the colliding nuclei has been properly accounted in JETPHOX. The results for the background prompt photons (direct and fragmentation) at LO for RHIC and LHC are displayed in Fig. 5.8. We recall that at leading order kinematics the four-momentum of the trigger jet is perfectly balanced by the parton or photon on the

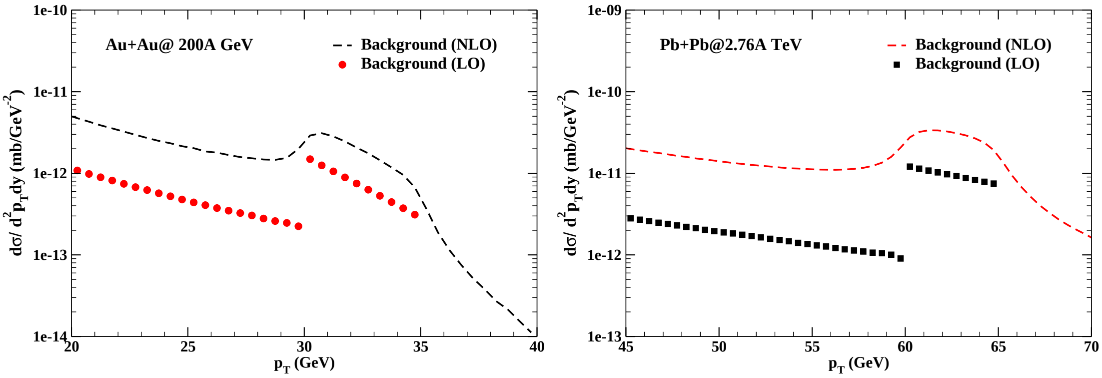

Figure 5.9: Total cross-section of background photons at LO and NLO for Au+Au and Pb+Pb collisions at RHIC and LHC respectively (see text for details). The result is normalized per nucelon-nucleon collision.

opposite side ($P_{jet} = P_{\gamma}$). This can be verified through the correlation between direct photon peak and the trigger jet window (see Fig. 5.8). The fragmentation photons are found to amass in the low p_T region as predicted. However at NLO, the Delta function like correlation between trigger jet and prompt photon is diluted because of the presence of third parton in the final state. The results for total background are shown in Fig. 5.9 where it is seen that the background develops an extended tail-like structure beyond the trigger-jet window.

5.5 Results

To identify the back-scattering photon signal, we propose to measure the nuclear modification of photon production around the trigger jet p_T window. The nuclear modification factor ($R^{\gamma}_{\rm AA}$) is defined as:

$$R^{\gamma}_{\rm AA}(p_T) = \frac{(\text{Signal+Background})_{AA}}{N_{coll} \times (\text{Background})_{pp}}, \tag{5.53}$$

where the 'Signal'refers to the jet-medium back-scattered photons and the 'Background'refers to prompt direct + fragmentation photons. N_{coll} is the total number of binary collisions for a given centrality of collision.

5.5.1 Effect of parton energy loss

For this preliminary study, we have considered central collisions of Au nuclei at RHIC (200A GeV) and Pb nuclei at LHC (2.76A TeV). We have used a longitudinally expanding, boost invariant fireball model; called PPM [160] to evaluate the back-scattering photon production (according to Eq. 5.52) and energy loss of fast quarks before re-scattering in the QGP medium. The transverse profile of entropy density depends on the number density of participant nucleons ($n_{part}(r)$), calculated from Glauber model. The normalization of the entropy density is fixed by the multiplicity data of Au+Au collisions at RHIC and scaled up to describe the data for Pb+Pb collisions at LHC. We have used the equation of state for ideal relativistic gas of 3 light quarks, to calculate the temperature of the system. PPM evaluates the differential energy loss $\Delta E = CI_\beta$

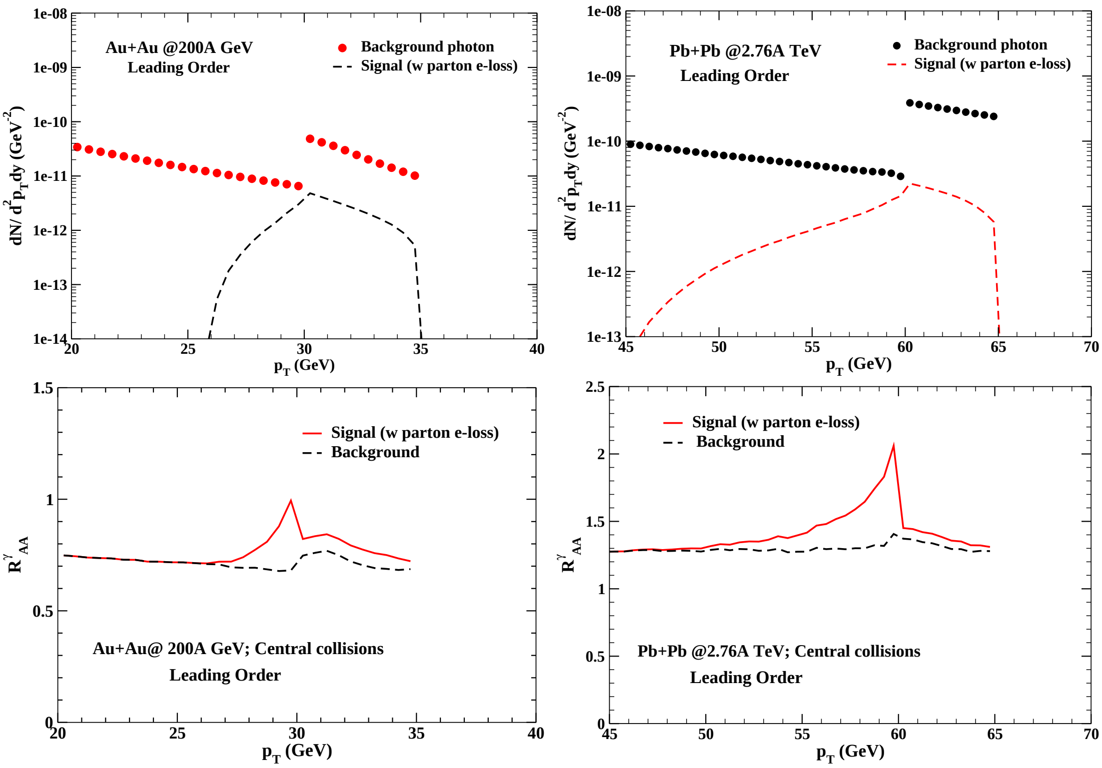

Figure 5.10: (Upper panel) Invariant yield of back-scattering photons in opposite to 30–35 GeV trigger jet at RHIC and 60–65 GeV trigger jet at LHC energy for central Au+Au and Pb+Pb collisions respectively. (Lower panel) The nuclear modification factor of back-scattering photon + background photon (solid red line) and only background photon (black dashed line) at RHIC and LHC kinematic conditions.

of a parton along the trajectory which is given by the expression:

$$I_\beta = \int d\tau \tau^\beta \rho(\mathbf{r} + \tau \hat{\mathbf{e}_\theta}), \qquad (5.54)$$

where $(\mathbf{r}, \theta)$ is the point of creation of the parton and $\hat{\mathbf{e}_\theta}$ is the unit vector along the trajectory. $\rho(\mathbf{r})$ describes the spatial distribution of the hard processes which is given by the number density of binary collisions ($n_{coll}(\mathbf{r})$). β encodes the path-length dependence of energy loss. In the present work, we adopted LPM type energy loss for which β=1. The coefficient C describes the quenching strength, is given by $C = \hat{q}(\mathbf{r})/n_{coll}(r)$. $\hat{q}(\mathbf{r})$ is proportional to the local entropy density and the normalization is determined from the inclusive hadron suppression at RHIC and LHC energies [160].

In order to calculate the 'Signal', we have extracted the fast parton (quark) invariant momentum yield from JETPHOX in the same kinematical situation. The current study includes 3 active quark flavors ($n_f = 3$). Now the phase-space distribution of the quark jets $f_q(\mathbf{p})$ is related to their invariant yield as [161]:

$$f_q(\mathbf{p}) = \frac{(2\pi)^3}{g_q \pi R^2 \tau p_T^q} \frac{dN^q}{d^2 p_T^q dy}, \tag{5.55}$$

where g_q=6 is the spin-color degeneracy of the quarks and R is the transverse dimension of the fireball. In the case of no energy loss suffered by the fast quark, back-scattering signal is lying under the prompt direct photon peak [162]. However the energy loss of fast quarks before conversion shift the back-scattering signal towards lower momentum, compared to the trigger window.

In Fig. 5.10, we have shown the results of back-scattered photon signal and nuclear modification factor for trigger jet window 30–35 GeV at RHIC and 60-65 GeV at LHC for LO kinematics. The diffusion of signal towards lower momentum is due to the energy loss of leading parton (quark). The characteristic peak in R^{γ}_{AA} just below the trigger window could be considered as a potential signature of back-scattering photons. It mostly comes from the down-shift of back-scattering photon strength under direct prompt photon peak. The nuclear modification factor of background photons (black dashed line) which could serve as baseline for this measurement, has also displayed in Fig. 5.10. We find the baseline R^{γ}_{AA} is compatible with different x regions of EPS09 parton distribution, probed by the trigger parton.

Next we show the results of nuclear modification factor with the background calculated at NLO accuracy in Fig. 5.11 The back-scattering signal is still LO because the leading parton picture, which we are using, is not quite well-defined at NLO. Therefore, the LO signal is scaled by a K-factor that we determine from the ratio (background at NLO)/ (background at LO) in the fragmentation dominated region of the background (e.g. 20 GeV at RHIC and 40 GeV at LHC) in pp collisions. We have found that

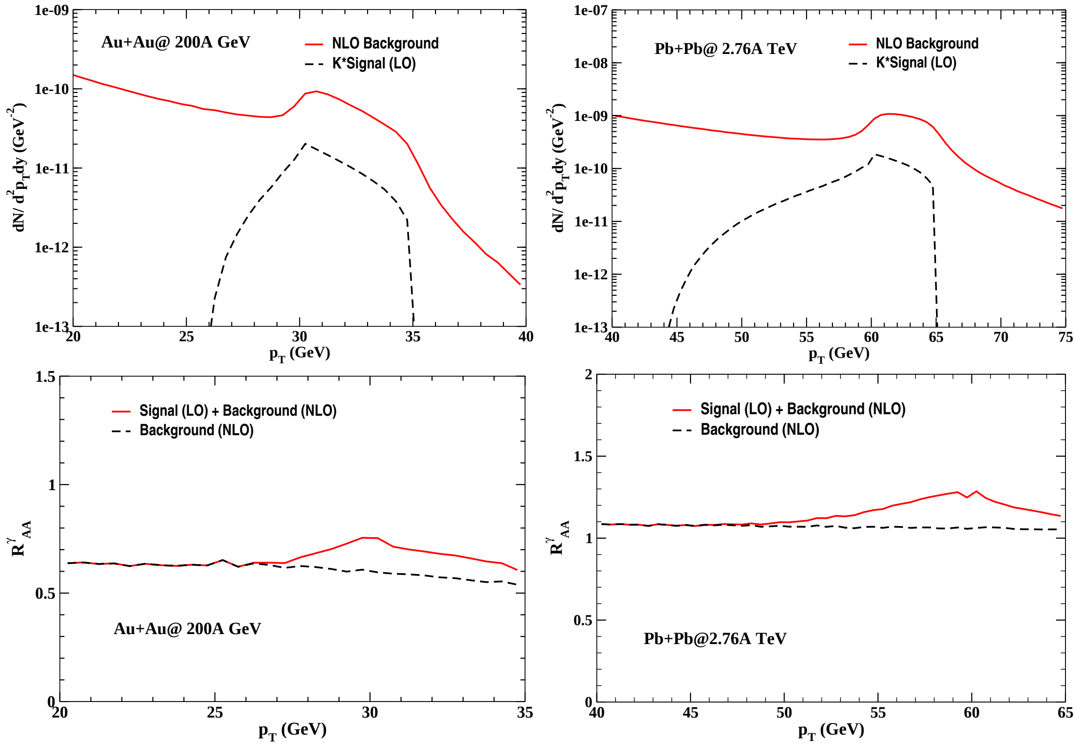

Figure 5.11: (Upper panel) Leading order back-scattering signal (multiplied by K-factor) with the NLO background prompt photons calculated for the RHIC and LHC kinematic conditions. (Lower panel) The nuclear modification factor of back-scattering signal(K-factor) + background photon (solid red line) and only background photon (black dashed line) at RHIC and LHC.

the potential signature in R^{γ}_{AA} weakens but survives at NLO. Though the radiative corrections tend to wash out the signal but can be separable from the background.

5.5.2 Effect of trigger jet energy loss

We have also studied the sensitivity of trigger jet energy loss on the back-scattering phenomenon for the LO kinematics [163]. Recent measurements at the LHC experiment [164, 165] indicate that jets are strongly suppressed in the medium. Jet energy loss is much less controlled in the present approach however an accurate analysis would require a full jet shower simulation in medium [166]. We have modelled the differential energy loss (i.e. amount of energy outside of a jet cone) is proportional to the path length and has weak logerthemic dependence on energy.

$$\frac{dE}{d\tau} = - \hat{r} \ln(\frac{E_T}{\Lambda}), \tag{5.56}$$

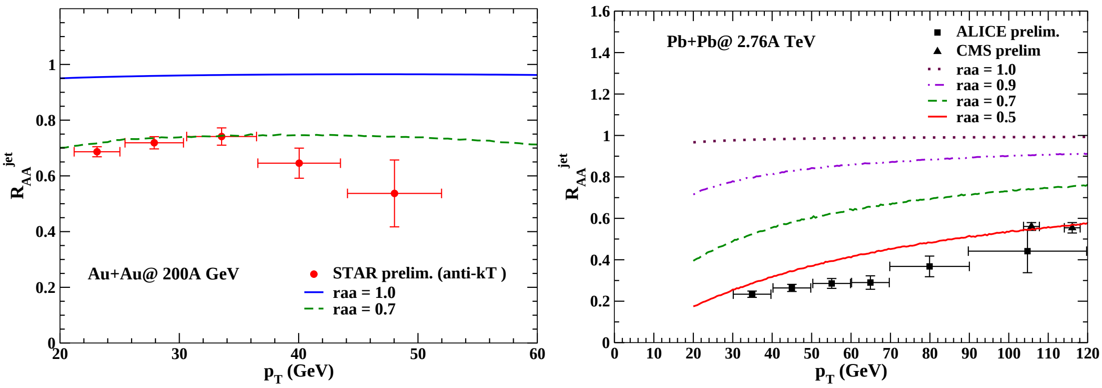

Figure 5.12: R^{jet}_{AA} of single inclusive jets calculated for (Left) central Au+Au collisions at RHIC for two values of $\hat{r}$ corresponds to "raa"values of 1.0 and 0.7 at p_T = 30 GeV (Right) central Pb+Pb collisions at LHC for four values of $\hat{r}$ corresponds to raa values of 1.0, 0.9, 0.7, 0.5 at p_T = 100 GeV. Data from STAR [167], ALICE [164] and CMS [165] collaborations are also shown for comparison.

where Λ= 0.2 GeV and $\hat{r}$ is proportional to the local entropy density as it was in case of leading parton energy loss.

In order to calibrate the jet energy loss, we have calculated the nuclear modification factor (R^{jet}_{AA}) of single inclusive jets for central Au+Au collisions at RHIC and Pb+Pb collisions at the LHC energy. We vary the normalization of $\hat{r}$ to generate a certain inclusive jet R^{jet}_{AA}. We shall refer to different values of $\hat{r}$ by quoting the approximate value of R^{jet}_{AA} at E_T= 30 GeV at RHIC and E_T= 100 GeV at LHC. The numbers are referred as "raa "in the plots. Our results of single inclusive jet suppression at RHIC and LHC are displayed in Fig. 5.12 along with the data from STAR, ALICE and CMS for the jet-cone radii 0.4, 0.2 and 0.4 respectively. In the present set-up we can not make a rigorous connection between jet cone radius and jet R_{AA}, however the lowest value of raa both at RHIC (0.7) and LHC (0.5) roughly corresponds to the suppression seen in these analyses with small cone radii.

Now we have a set of jet energy loss parameters $\hat{r}$ that contains the information of currently available jet reconstruction accuracy, but more optimistic situations would be if larger jet cones are used in experiment that contain more of the original jet energy. Next we calculate the photon spectra (both background and signal) in opposite of trigger jets for the different energy loss scenarios. For this purpose, we generalize the formula 5.52 to the rate of photons associated with a trigger jet window (Γ_j) in $E_T - y_{jet} - \phi_j$ space described earlier. We replace the single quark distribution $f_q(\mathbf{p})$ by the parton-jet pair distribution integrated over Γ_j,

$$f_q^{\Gamma_j}(\mathbf{p}_q) = \frac{(2\pi)^3}{g_q \tau p_T}\delta(y-\eta)\rho(\tau,\mathbf{r}_\perp) \times \int_{\Gamma_j} dE_T dy_{jet} d\phi_j E_q \frac{dN}{d^3p_q dE_T dy_{jet} d\phi_j}\Big|_{\substack{\mathbf{p}_q+\Delta\mathbf{p}_q \\ E_T+\Delta E_T}} \tag{5.57}$$

where $r = (\tau, \eta, \mathbf{r}_\perp)$ and $\mathbf{p_q}$ are the position and momentum of the quark at the time of back-scattering. $r^0 = (\tau_0, \eta, \mathbf{r}^\mathbf{0}_\perp)$ and $\mathbf{p}^\mathbf{0}_\mathbf{q}$ are the initial position and momentum of the quark when it was created in the hard collision. The quark is supposed to travel in straight line along the direction of $\mathbf{p}^\mathbf{0}_\mathbf{q}$, i.e. $\mathbf{r}_\perp = \mathbf{r}^\mathbf{0}_\perp + (\tau-\tau_0)\hat{\mathbf{p}}^0_q$. $\Delta\mathbf{p}_q$ and ΔE_T are energy lost by the parent quark and the trigger jet in the medium respectively. $\rho(\tau,\mathbf{r}_\perp)$ gives the density of hard collisions in the transverse plane as before.

Here PPM propagates all photon-jet pairs and parton-jet pairs emitted from the hard collisions. The energy loss of the jet in the medium is calculated according to Eq. 5.56 and all photon-jet pairs with final jet energy falls within Γ_j are counted. For parton-jet pairs the energy loss of the jet and of the parton are calculated while the back-scattering probability of the parton is also taken into account. We do not take into account energy loss for partons before fragmentation in order to get a lower estimate for the signal to background ratio. However if energy loss of fragmenting partons is taken into account it will help suppress the fragmentation background at high photon-z.

In Fig. 5.13, we have shown the background photon and the back-scattering photon spectra for the four trigger jet energy loss scenarios (raa 1.0, 0.9, 0.7, 0.5) at LHC and two scenarios (raa 1.0, 0.7) at RHIC with parton energy loss included at LO kinematics. We have checked that the scenario 'raa 1.0'reproduces our old result of only parton energy loss. The general behaviour we have found is both the signal and background diffuses and tends to be shifted towards higher p_T window. This is due to the fact that a trigger jet counted in 30–35 GeV or 60–65 window might have originated a jet of larger energy. While the diffusion of signal strength at RHIC is about 3–4 GeV above the trigger jet p_T window (raa 0.5), it becomes quite larger at LHC$\sim$ 10 GeV (raa 0.5 and 0.7).

We have found the energy loss of trigger jet leads to suppression in R^γ_{AA} in the trigger jet window due to shift of background photons towards higher p_T. On the other hand the back-scattering signal causes a local enhancement in R^γ_{AA} just below the trigger

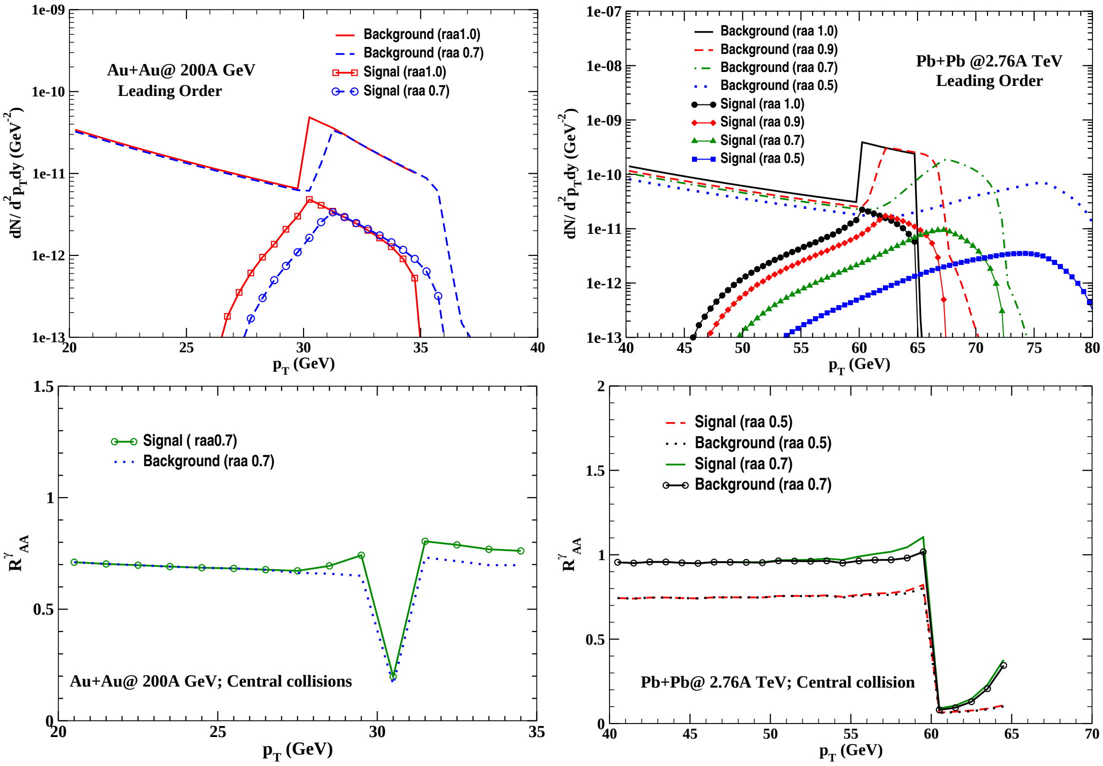

Figure 5.13: (Upper panel) Invariant yield of background photon and back-scattering photon, (Lower panel) nuclear modification factor of calculated for back-scattering photon + background photon ('Signal') and only background photon ('Background') for different trigger jet energy loss scenarios in central Au+Au collisions at RHIC and Pb+Pb collisions at the LHC energy.

jet window. However the enhancement is not visible for the current jet reconstruction scenario (raa 0.5) at the LHC. The width of the dip can be correlated with the momentum shift of the trigger jet due to energy loss.

In conclusion, We find that the separation of back-scattering photons from other photon sources using trigger jets depends crucially on our ability to reliably estimate the original trigger jet energy. With the current jet cone sizes and jet energy loss, the signal is too weak to be observed. The width of the signal carries information about jet and parton energy loss. However we have to realize that the present calculation has estimated a *lower* limit of the back-scattering photon strength. First, the use of simple equation of state underestimates the temperature and thus the back-scattering rate; second, we omitted induced photon bremsstrahlung, which will generally increase the back-scattering photon rate below the trigger window and lastly the energy loss of partons before fragmenting to photons, effectively reduces the background.

Chapter 6

Summary and Outlook

Electromagnetic and hard probes of strongly interacting matter which consists of thermal photon intensity interferometry, suppressed production of hadrons at large momenta and identification of jet-medium back-scattered photons, have been discussed in detail in this thesis. A brief summary of each of the topic is provided below.

Construction of EoS and two photon intensity interferometry

Within the framework of hadron resonance gas model, we have constructed an equation of state (EoS) of hot hadronic matter which consists of discrete hadronic states up to mass (m)$\leq$ 2 GeV and continuous Hagedorn states in the mass range 2 $<$ m $<$12 GeV. It has been found that thermodynamic quantities agree quite well with the lattice QCD simulation results for temperature (T)$\leq$ 200 MeV, on accounting for Hagedorn resonances and finite volume correction of hadrons. The hadronic matter description is switched either to Bag model equation of state or lattice equation of state at temperature 165 MeV. The EoS includes the Bag Model admits a first order phase transition whereas the lattice based EoS shows a rapid cross-over from QGP to hadron gas. Using the two EoS we have calculated thermal particle and thermal photon transverse momentum spectra for the central collisions of Au and Pb nuclei at the top RHIC (200A GeV) and LHC (5.5A TeV) energy respectively, considering ideal relativistic hydrodynamic evolution. The particle and photon spectra have shown marginal sensitivity to the difference between the two EoS. But temporal and spatial evolution of the photon emitting source has been found different for the two EoS. Motivating by this observation, we have calculated two photon intensity correlation at the RHIC and LHC energies. The two photon correlation function has been found to differentiate between first order phase transition or cross-over from partonic matter to hadronic matter. Thus the present findings could be valuable in order to probe the EoS of strongly interacting matter in experiment. Further developments in the line can be done by checking the sensitivity of initial parameters of the simulation or considering a more realistic evolution (e.g. viscous hydrodynamics) of the system.

Centrality dependence of nuclear modification of hadron production

We have investigated the system size dependence of jet-quenching by analyzing the suppressed production of hadrons in the collisions of Au and Cu nuclei at center of mass energy 200A GeV (RHIC) and Pb nuclei at 2.76A TeV (LHC). We have used a simple phenomenological model of parton energy loss in which the QGP medium is considered as an assembly of static scattering centers at some fixed temperature. Next-to leading order (NLO) perturbative QCD has been used for the initial production of partons and then they are assumed to lose energy via gluon bremsstrahlung while traversing the QGP. The energy loss per collision, ε, is taken proportional to the energy of the parton (E), $\sqrt{E}$ or constant for the incoherent, partial coherent and complete coherent regimes of gluon radiation. The energy loss formalism closely follows the model advocated by Baier, Dokshitzer, Mueller, Peigné, Schiff. The finite probability of multiple scattering of partons and nuclear modification to parton distributions are also taken into account. By calculating the path length traversed by the parton in QGP, ε remains to be only adjustable parameter in this calculation. With the model, we have reproduced the centrality dependence of nuclear modification factor (R_{AA}) of hadron production measured at RHIC and LHC energies. Thus the study has demonstrated the change in parton energy loss mechanisms which is revealed through the transverse momentum dependence of nuclear modification factor of hadron production. Additionally, we have empirically found the linear path length dependence of parton energy loss at the large transverse momentum regime at RHIC and LHC.

Jet-tagged back-scattering photons in quark-gluon plasma

The direct photons (real and virtual) are considered as an excellent messenger of QGP properties because of their large mean ree path. Several sources of direct photons has been proposed so far in theory but the separation of a single contribution is a challenging task in experiment. Photons originated due to Compton backscattering of large momentum jets in QGP, was first reported in PRL 90, 132301 (2003). The jet-medium Compton back-scattered photons are considered to contain valuable information about the temperature and parton energy loss mechanism in QGP. Attempts to identify this source in experiment through direct photon inclusive spectra or azimuthal momentum anisotropy (v_2) at RHIC energy has been inconclusive so far. In the present work, we have proposed a novel way to separate these particular photons from other direct photon sources by using the correlation with the trigger jet at large photon momentum. The hard prompt photons are only produced in coincidence with a jet, considered as 'background'for this study. We have calculated the invariant yield and nuclear modification factor of back-scattering photons in coincidence with the trigger jet at leading order of strong coupling for the central Au+Au collisions at RHIC (200A GeV) and Pb+Pb collisions at LHC (2.76A TeV). For this purpose, we have used a NLO perturbative QCD code of prompt photon production and a fireball model for the evolution of the medium. The back-scattering photons have caused a sharp peak in the nuclear modification factor around the trigger jet window which could be considered as a potential signal. The height and width of the peak is related with the temperature and energy loss of quarks in the medium. However it has been found that inclusion of higher order processes for the 'background'and account for the trigger jet energy loss tends to wash out the signal. Thus the present analysis is concluded with a comment that there exists a possibility to separate Compton back-scattered photons from other sources if the energy of the trigger jet is determined reliably in experiment.

Appendix A

Finite volume correction of thermodynamic variables

Following the pressure ensemble formalism of Hagedorn [168], the grand canonical pressure partition function is defined as:

$$\Pi(\beta, \xi, V) = \int_0^\infty dV exp(-\xi V) Z(\beta, V, \lambda), \tag{A.1}$$

where $Z(\beta, V, \lambda)$ is the grand canonical partition function. $\beta = 1/T$, $\lambda = \mu/T$. ξ is a new parameter associated with volume, in a similar way β is related to energy and μ is related to number density.

Re-writing Eq. A.1 as,

$$\Pi(\beta, \xi, V) = \int_0^\infty dV exp\left(-V[\xi - \frac{1}{V}\ln Z(\beta, V, \lambda)]\right). \tag{A.2}$$

We define $\xi_0 = \frac{1}{V}\ln Z(\beta, V, \lambda)$. Thus the integral converges for the values of $\xi > \xi_0$, provided the thermodynamic limit

$$\lim_{V\to\infty} \frac{1}{V}\ln Z(\beta, V, \lambda) \quad \text{exists.} \tag{A.3}$$

The pressure $P(\beta, \lambda)$ is given by the singularity of partition function $\Pi(\beta, \xi, V)$;

$$\xi_0(\beta, \lambda) = \lim_{V\to\infty}[\frac{1}{V}\ln Z(\beta, V, \lambda)] = \beta P(\beta, \lambda). \tag{A.4}$$

We can define a function $g(\beta, \lambda, V)$, as the difference between $\frac{1}{V}\ln Z$ and ξ_0,

$$g(\beta, V, \lambda) = \frac{1}{V}\ln Z(\beta, V, \lambda) - \xi_0. \tag{A.5}$$

If the finite volume effects are neglected in defining $Z(\beta, V, \lambda)$, then $g = 0$. The nature of the singularity ξ_0 (pole or branch cut) depends on the function $g(\beta, V, \lambda)$.

By giving a short introduction of pressure ensemble formalism, now we write the grand canonical partition function Z for a system of identical particles with finite size treated relativistically with Boltzmann statistics [46]:

$$Z(\beta, V) = \sum_{N=0}^{\infty} \frac{1}{N!} \prod_{i=1}^{N} \int \frac{d^3p}{(2\pi)^3} exp(-\beta\epsilon_i) \times (V - V_0)^N, \tag{A.6}$$

where $V_0 = \sum_{i=1}^{N} (\epsilon_i/4B)$ is the total volume occupied by the particles. ϵ_i is the energy of the i^{th} particle and B is the MIT Bag constant.

Taking Laplace's transform of partition function,

$$\widehat{\Pi}(\beta, \xi, V) = \int_{V_0}^{\infty} dV exp(-\xi V) Z(\beta, V). \tag{A.7}$$

The factor simplifies as:

$$\begin{aligned}
& \int_{V_0}^{\infty} dV (V - V_0)^N exp(-\xi V) \\
= \;& exp(-\xi V_0) \int_{V_0}^{\infty} dV (V - V_0)^N exp(-\xi(V - V_0)) \\
= \;& exp(-\xi \sum_{i=1}^{N} \frac{\epsilon_i}{4B}) \frac{N!}{\xi^{N+1}} \\
= \;& \prod_{i=1}^{N} exp(-\xi \frac{\epsilon_i}{4B}) \frac{N!}{\xi^{N+1}}.
\end{aligned} \tag{A.8}$$

Thus we get the partition function for the pressure ensemble from Eq. A.7 as:

$$\begin{aligned}
\widehat{\Pi}(\beta, \xi, V) &= \sum_{N=0}^{\infty} \frac{1}{N!} \prod_{i=1}^{N} \int \frac{d^3p}{(2\pi)^3} exp(-\beta\epsilon_i)\, exp(-\xi \frac{\epsilon_i}{4B}) \frac{N!}{\xi^{N+1}} \\
&\approx \frac{1}{\xi} \sum_{N=0}^{\infty} \left[\frac{1}{\xi} \int \frac{d^3p}{(2\pi)^3}\, exp\left(-\epsilon(\beta + \xi/4B)\right) \right]^N
\end{aligned} \tag{A.9}$$

Let us consider

$$x = \frac{1}{\xi} \int \frac{d^3p}{(2\pi)^3} exp\left(-\epsilon(\beta + \xi/4B)\right) \tag{A.10}$$

and use binomial expansion

$$\sum_{N=0}^{\infty} x^N = \frac{1}{1 - x}, \tag{A.11}$$

thus Eq. A.9 becomes:

$$\widehat{\Pi}(\beta, \xi, V) \;=\; \frac{1}{\xi} \left[\frac{1}{1 - \frac{1}{\xi} \int \frac{d^3p}{(2\pi)^3}\, exp\left(-\epsilon(\beta + \xi/4B)\right)} \right]$$

$$
\begin{aligned}
&= \frac{1}{\xi - \int \frac{d^3p}{(2\pi)^3} exp\,(-\beta^*\epsilon)} \\
&= \frac{1}{\xi - \beta^* P_{pt}(\beta^*)} \qquad \text{(A.12)}
\end{aligned}
$$

where $\beta^* = (\beta + \xi/4B)$ and $P_{pt}(\beta^*) = 1/\beta^* \int d^3p/(2\pi)^3 exp(-\beta^*\epsilon)$ is the pressure of a system of point like particles with temperature $(1/\beta^*)$.

From the general consideration of pressure ensemble, the pressure P_{xv} for a system of finite volume particles with temperature $(1/\beta)$ is obtained by locating the pole ξ_0 of the partition function $\widehat{\Pi}(\beta, \xi, V)$:

$$\xi = \beta P_{xv}(\beta) = \xi_0. \qquad \text{(A.13)}$$

Thus we get;

$$
\begin{aligned}
\xi_0 = \beta P_{xv}(\beta) &= \beta^* P_{pt}(\beta^*) \\
\beta P_{xv}(\beta) &= (\beta \ + \ \xi/4B) P_{pt}(\beta^*) \\
\beta P_{xv}(\beta) &= \beta P_{pt}(\beta^*) \ + \ \frac{\beta P_{xv}(\beta)}{4B} P_{pt}(\beta^*) \\
P_{xv}(\beta) &= P_{pt}(\beta^*) \ + \ \frac{P_{pt}(\beta^*)}{4B} P_{xv}(\beta) \\
P_{xv}(\beta) &= \frac{P_{pt}(\beta^*)}{1 - \frac{P_{pt}(\beta^*)}{4B}} \qquad \text{(A.14)}
\end{aligned}
$$

The Eq. A.14 provides the relation between pressure with finite volume correction and the pressure of point like particles.

Appendix B

The invariant momentum spectra of hadrons

The hadrons are emitted from an infinitesimal fluid element moving with four-velocity u_μ, often follows the ideal gas like distribution:

$$f(x,p) = \frac{g}{(2\pi)^3}\frac{1}{exp(p^\mu u_\mu/T) \pm 1}, \tag{B.1}$$

where g is the spin-isospin degeneracy and p^μ is the four-momentum of the hadron in a frame where u_μ is measured. The normalization of u_μ is taken as; $u^\mu u_\mu$= -1. Thus the flux of particles within momentum element d^3p through an element of surface $d\sigma_\mu$ [54],

$$dN = \int d^3p f(x,p)\frac{p^\mu}{p_0}d\sigma_\mu. \tag{B.2}$$

The invariant momentum distribution of a particular kind of hadron is given by:

$$E\frac{dN}{d^3p} = \frac{dN}{d^2p_T dy} = \frac{g}{(2\pi)^3}\int f(x,p)p^\mu d\sigma_\mu. \tag{B.3}$$

Now the four-momentum of the hadron

$$p^\mu = (m_T \cosh y, p_T cos\phi, p_T sin\phi, m_T \sinh y), \tag{B.4}$$

and the four-velocity for an azimuthally symmetric system

$$u_\mu = \gamma_r(\cosh\eta, -v_r, 0, -\sinh\eta) \tag{B.5}$$

with y is the energy-momentum rapidity, η is the space-time rapidity and $\gamma_r = 1/\sqrt{1-v_r^2}$ is the Lorentz boost. Then

$$\begin{aligned} p^\mu u_\mu &= \gamma_r m_T \cosh(y-\eta) - \gamma_r v_r p_T cos\phi \\ &= m_T \cosh y_T \cosh(y-\eta) - p_T \sinh y_T cos\phi. \end{aligned} \tag{B.6}$$

y_T is called the 'Transverse rapidity'defined as:

$$y_T = \frac{1}{2} \ln \frac{1+v_r}{1-v_r} \tag{B.7}$$

so that $\gamma_r = \cosh y_T$, $v_r = \tanh y_T$ and $\gamma_r v_r = \sinh y_T$.

From Eq. B.1, we write the phase space distribution of the hadron:

$$f(x,p) = \frac{g}{(2\pi)^3} \frac{1}{exp\left\{(m_T \cosh y_T \cosh(y-\eta) - p_T \sinh y_T cos\phi)/T\right\} \pm 1} \tag{B.8}$$

Next we discuss the freeze-out criterion. At some constant freeze-out temperature $T(r,\tau) = T_{frez}$; the numerical algorithm determines a three dimensional decoupling surface (Σ_μ) whose surface elements are given by the vector $d\sigma_\mu$.
In general, $d\sigma_\mu = (d^3\vec{x}, dtd\vec{S})$. For an azimuthally symmetric system, the decoupling surface element can be written as:

$$d\sigma^\mu = (rdrd\phi dz, \hat{e_r} rd\phi dzdt, 0, \hat{e_z} rd\phi drdt) \tag{B.9}$$

Using the relations $t = \tau \cosh\eta$, $z = \tau \sinh\eta$ and $dtdz = \tau d\tau d\eta$, we write

$$p^\mu d\sigma_\mu = rd\phi d\eta[m_T \tau \cosh(y-\eta)dr + m_T \sinh(y-\eta)d\tau - p_T \tau cos\phi d\tau]. \tag{B.10}$$

In case of boost-invariant scenario $y = \eta$, the second term of expression (B.10) has null contribution. Inserting the expressions (B.8) and (B.10) in Eq. B.3 and integrating over the phase space variables leads to

$$\frac{dN}{d^2p_T dy} = \frac{g}{(2\pi)^3} \int \tau r \int_0^{2\pi} d\phi \int d\eta \frac{m_T \cosh(y-\eta)dr - p_T cos\phi d\tau}{exp\left\{(m_T \cosh y_T \cosh(y-\eta) - p_T \sinh y_T cos\phi)/T\right\} \pm 1} \tag{B.11}$$

We find the result is independent of y for the boost-invariant case. Also we need the value of transverse flow velocity (v_r) at $z = 0$ for calculating the momentum spectra. The integration over τ and r are done along the surface defined by $T(r,\tau) = T_{frez}$.

Bibliography

[1] G. Miller *et al.* [SLAC-MIT collaboration], Phys. Rev. D **5** (1972) 528.

[2] H.J.Behrend *et al.*, Phys. Lett. **183B** (1987) 400.

[3] J. C. Collins and M. J. Perry, Phys. Rev. Lett. **34** (1975) 1353.

[4] S. Weinberg, Gravitation and Cosmology (John Wiley & Sons, 1972).

[5] E. V. Shuryak, Sov. Phys. JETP **47** (1978) 212-219.

[6] C. R. Allton *et al.* Phys. Rev. D **68** (2003) 014507.

[7] Z. Fodor, S.D. Katz, JHEP 0404 (2004) 050.

[8] M.M. Aggarwal et al (for the STAR Collaboration), arXiv:1007.2613 [nucl-ex].

[9] CERN Courier 40 (May 2000) 13.

[10] B. B. Back et al., Nucl. Phys. A **757** (2005) 28; J. J. Adams et al., Nucl. Phys. A **757** (2005) 102.

[11] ALICE Physics Summary, arXiv:1302.0763.

[12] R. J. Fries and C.Nonaka, Prog. in Part. and Nucl. Phys. **66** (2011) 607.

[13] M. L. Milller *et al.*, arXiv:nucl-ex/0701025 (2007).

[14] A. Krasnitz, Y. Nara and R. Venugopalan, Phys. Rev. Lett. **87** (2001) 192302.

[15] C. Nonaka and M. Asakawa, arXiv:1204.4795[nucl-th](2012).

[16] U. Heinz and R. Snellings, [arXiv:1301.2826 [nucl-th]].

[17] H. Song, S. A. Bass and U. Heinz, Phys. Rev. C **83** (2011) 024912.

[18] F. Cooper and G. Frye, Phys. Rev. D **10** (1974) 186.

[19] A. Andronic, P. Braun-Munzinger, J. Stachel, Nucl. Phys. A **772** (2006) 167; A. Andronic *et al.* Nucl. Phys. A **837** (2010) 65.

[20] M. Gyulassy and L. Mclerran, Nucl. Phys. A **750** (2005) 30.

[21] E. Schnedermann and U. Heinz, Phys. Rev. Lett. **69** (1992) 2908 ; D. E. Kahana, D. Keane, Y. Pang, T. Schlagel, and S. Wang, Phys. Rev. Lett. **74** (1995) 4404.

[22] H. Sorge, Phys. Rev. Lett. **78** (1997) 2309.

[23] P. F. Kolb *et al.* Nucl. Phys. A 696 (2001) 197.

[24] H.Song, S.A.Bass, and U.Heinz, arXiv:1311.0157 [nucl-th].

[25] R. Chatterjee, E. S. Frodermann, U. W. Heinz and D. K. Srivastava, Phys. Rev. Lett. **96** (2006) 202302.

[26] A. Adare *et al.* Phys. Rev. Lett. **109** (2012) 122302.

[27] U. W. Heinz, [arXiv:0901.4355 [nucl-th]].

[28] V. Greco, C. M. Ko and P. Levai, Phys. Rev. Lett. **90** (2003) 202302.

[29] R. J. Fries, B. Müller, C. Nonaka and S. A. Bass Phys. Rev. Lett. **90** (2003) 202303.

[30] D. Molnar and S. A. Voloshin, Phys. Rev. Lett. **91** (2003) 092301.

[31] J. Rafelski and B. Müller, Phys. Rev. Lett. **48** (1982) 1066 [Erratum-ibid. **56** (1986) 2334]; P. Koch, B. Müller and J. Rafelski, Phys. Rep. **142** (1986) 167.

[32] C. Y. Wong, Introduction to Heavy Ion Collisions, World-Scientific Publishing.

[33] S. V Afanasiev *et al.* NA49 Collaboration), Phys. Rev. C **66** (2002) 054902; C. Alt et al. (NA49 Collaborations), Phys. Rev. C **77** (2008) 024903; S. S. Adler *et al.* Phys. Rev. C **69** (2004) 034909.

[34] T. Matsui and H. Satz, Phys. Lett. B **178** (1986) 416.

[35] A. Lebedev *et al.* (PHENIX Collaboration) Nucl. Phys. A **854** (2011) 204; M. Wysocki it et al. (PHENIX Collaboration) Eur. Phys. J. C **62** (2009) 103.

[36] G. E. Bruno [ALICE Collaboration], arXiv:1310.5492 [nucl-ex].

[37] L.D. Landau, Izv. Akad. Nauk Ser. Fiz. **17** (1953) 51.

[38] J. Cleymans, R. V. Gavai and E. Suhonen, Physics Reports **130** (1986) 217.

[39] R. Hagedorn, Nuovo Cimento Suppl. **3**, (1965) 147.

[40] Abhijit Majumder and Berndt Müller, Phys. Rev. Lett. **105** (2010) 252002.

[41] J. Noronha-Hostler, M. Beitel, C. Greiner, and I. Shovkovy, Phys. Rev. C **81** (2010) 054909.

[42] G.M. Welke, R. Venugopalan and M. Prakash, Phys. Lett. B **245** (1990) 137.

[43] A. Chodos, R. L. Jaffe, K. Johnson, C. B. Thorn and V. F. Weisskopf, Phys. Rev. D **9** (1974) 3471.

[44] J. Cleymans, K. Redlich, H. Satz and E. Suhonen Z. Phys. C **33** (1986) 151.

[45] R. Hagedorn and J. Rafelski Phys. Lett. B **97** (1980) 136.

[46] J. I. Kapusta and K. A. Olive, Nucl. Phys. A **408** (1983) 478.

[47] A. Bazavov *et al.*, Phys. Rev. D **80** (2009) 014504.

[48] A. Andronic, P. Braun-Munzinger and J. Stachel Phys. Lett. B **673** (2009) 142; J. Cleymans, H. Oeschler, K. Redlich, and S. Wheaton Phys. Rev. C **73** (2006) 034905.

[49] I. Kraus, J. Cleymans, H. Oeschler, K. Redlich, and S. Wheaton, arXiv:0902.0873 [hep-ph].

[50] H. Von Gersdorff, L. D. McLerran, M. Kataja and P. V. Ruuskanen, Phys. Rev. D **34**, (1986) 794.

[51] J. Alam, D. K. Srivastava, B. Sinha and D. N. Basu, Phys. Rev. D **48** (1993) 1117.

[52] J. P. Boris and D. L. Book, J. Comp. Physics **11** (1973) 38.

[53] B. L. Friman, G. Baym, J. P. Blaizot, Phys. Lett. B **123** (1983) 291.

[54] P. V. Ruuskanen, Acta. Phys. Pol. B **18** (1987) 551.

[55] P. F. Kolb and U. W. Heinz (2003) arXiv:nucl-th/0305084.

[56] D. Kharzeev and M. Nardi, Phys. Lett. B **507** (2001) 121.

[57] X. N. Wang, Phys. Rep. **280** (1997) 287.

[58] K. J. Eskola, K. Kajantie, P. V. Ruuskanen, and K. Tuominen, Nucl. Phys. B **570** (2000) 379.

[59] K. J. Eskola, H. Honkanen, H. Niemi, P. V. Ruuskanen and S. S. Rasanen, Phys. Rev. C **72** (2005) 044904.

[60] E. Frodermann, R. Chatterjee and U. Heinz, J. Phys. G: Nucl. Part. Phys. **34** (2007) 2249.

[61] V. Roy and A. K. Chaudhuri, Phys. Rev. C **82** (2010) 031901.

[62] P. Braun-Munzinger, I. Heppe, and J. Stachel, Phys. Lett. B **465** (1999) 15; J. Cleymans, R. Sahoo, D. K. Srivastava and S. Wheaton, Eur. Phys. J. ST **155** (2008) 13.

[63] S. S. Adler *et al.* (PHENIX Collaboration) Phys. Rev. C **69** (2004) 034909.

[64] J. Sollfrank, P. Koch and U. W. Heinz, Phys. Lett. B **252** (1990) 256.

[65] P. B. Arnold, G. D. Moore and L. G. Yaffe, JHEP **0112** (2001) 009.

[66] S. Turbide, R. Rapp,and C. Gale, Phys. Rev. C **69** (2004) 014903.

[67] R. Chatterjee and D. K. Srivastava, Phys. Rev. C **79** (2009) 021901(R).

[68] A. Adare *et al.* (PHENIX Collaboration) Phys. Rev. Lett. **104** (2010) 132301.

[69] D. K. Srivastava and J. I. Kapusta, Phys. Rev. C **48** (1993) 1335; D. K. Srivastava and C. Gale, Phys. Lett. B **319** (1993) 407; D. K. Srivastava, Phys. Rev. D **49** (1994) 4523.

[70] D. K. Srivastava and R. Chatterjee Phys. Rev. C **80** (2009) 054914.

[71] S. Pratt, Phys. Rev. Lett. **53** (1984) 1219.

[72] G. Bertsch, M. Gong, and M. Tohyama, Phys. Rev. C **37** (1988) 1896.

[73] R. Hanbury Brown and R. Q. Twiss, Nature **178** (1956) 1046; R. Hanbury Brown and R. Q. Twiss, Proc of the Royal Society of London A **242** (1957) 300–324, **243** (1958) 291–319.

[74] G. Goldhaber, S. Goldhaber, W. Y. Lee and A. Pais, Phys. Rev. **120**(1960) 300.

[75] F. M. Marqués *et al.*, Phys. Rep. **284** (1997) 91.

[76] C. Slotta and U. Heinz, Phys. Lett. B **391** (1997) 469.

[77] D. K. Srivastava, Phys. Rev. C **71** (2005) 034905.

[78] S. Chapman, P. Scotto and U. Heinz, Phys. Rev. Lett. **74** (1995) 4400.

[79] U. Heinz and B. V. Jacak, Ann. Rev. Nucl. Part. Sci. **49** (1999) 529.

[80] S. Chapman, J. R. Nix and U. Heinz, Phys. Rev. C **52** (1995) 2694.

[81] M. A. Lisa *et al.* Phys. Rev. Lett. **71** (1993) 2863.

[82] S. Pratt *et al.* Nucl. Phys. A **566** (1994) 103c.

[83] G. F. Bertsch,Nucl. Phys. A **498** (1989) 173c; S. Pratt *et al.* Phys. Rev. C **42** (1990) 2646.

[84] D. Rischke and M. Gyulassy, Nucl. Phys. A **608**(1996) 479.

[85] S. Soff, S. A. Bass, and A. Dumitru, Phys. Rev. Lett. **86**(2001) 3981.

[86] C. Adler *et al.* [STAR Collaboration], Phys. Rev. Lett. **87** (2001) 082301; Phys. Rev. C **71** (2005) 044906.

[87] U. Heinz and P. F. Kolb, (2002) arxiv:hep-ph/0204061.

[88] S. Pratt, Nucl. Phys. A **830** (2009) 51c.

[89] D. Neuhauser, Phys. Lett. B **182** (1986) 289.

[90] J. Pisut, N. Pisutova and B. Tomasik, Phys. Lett. B **345** (1995) 553; D. Peressounko Phys. Rev. C **67** (2003) 014905; J. Alam, B. Mohanty, P. Roy, S. Sarkar and B. Sinha Phys. Rev. C **67** (2003) 054902.

[91] E. Frodermann and U. Heinz Phys. Rev. C **80** (2009) 044903;

[92] F. M. Marqués *et al.* Phys. Lett. B **349** (1995) 30.

[93] M. M. Aggarwal *et al.* Phys. Rev. Lett. **93** (2004) 022301.

[94] L. Ahle *et al.* E802 Collaboration, Nucl. Phys. A. **610** (1996) 213c.

[95] S. De, D. K. Srivastava and R. Chatterjee J. Phys. G: Nucl. Part. Phys. **37** (2010) 115004.

[96] K. Adcox *et al.* [PHENIX Collaboration], Phys. Rev. Lett. **88**, 022301 (2002); J. Adams *et al.* [STAR Collaboration], Phys. Rev. Lett. **91**, 172302 (2003).

[97] K. Aamodt *et al.* [ALICE Collaboration], Phys. Lett. B **696** (2011) 30; [ATLAS Collaboration], Phys. Lett. B **719** (2013) 220.

[98] M. Gyulassy and M. Plümer 1990 Phys. Lett. B 243 432; X. N. Wang and M. Gyulassy, Phys. Rev. Lett. **68** (1992) 1480.

[99] J. D. Bjorken, FERMILAB-PUB-82-059-THY (1982).

[100] X.-N. Wang, Phys. Rep. 280 (1997) 287.

[101] M. Gyulassy and X. N. Wang, Nucl. Phys. B **420** (1994) 583.

[102] R.Baier *et al.*, Phys. Lett. B **345** (1995) 277.

[103] R. Baier, D. Schiff and B. G. Zakharov, Ann. Rev. Nucl. Part. Sci. **50** (2000) 37.

[104] G. Aad *et al.* (ATLAS Collaboration)Phys. Rev. Lett. **105** (2010) 252303.

[105] M.Gyulassy, I.Vitev and X.N.Wang, Phys. Rev. Lett. **86** (2001) 2537. X. N. Wang, Phys. Rev. C **63** (2001) 05490.

[106] M.H. Thoma, M. Gyulassy, Nucl. Phys. B **351** (1991) 491.

[107] S. Peigne and A. Peshier, Phys. Rev. D **77** 114017 (2008).

[108] X.-F. Guo and X.-N. Wang, Phys. Rev. Lett. **85** (2000) 3591; A. Majumder, E. Wang, and X.N. Wang, Phys. Rev. Lett. **99** (2007) 152301.

[109] M. Gyulassy, P. Levai and I. Vitev, Nucl. Phys. B **571** (2000) 197; M. Gyulassy, P. Levai and I. Vitev, Phys. Rev. Lett. **85** (2000) 5535.

[110] B. G. Zakharov, JETP Lett. **63** (1996) 952; B. G. Zakharov, JETP Lett. **65** (1997) 615.

[111] U. A. Wiedemann, Nucl. Phys. B **582**, (2000) 409; C. A. Salgado and U. A.Wiedemann, Phys.Rev. Lett. **89** (2002) 092303; N. Armesto, C. A. Salgado, and U. A. Wiedemann, Phys. Rev. Lett. **94** (2005) 022002.

[112] P. Arnold, G. D. Moore, and L. G. Yaffe, J. High Energy Phys. **11** (2000) 001; S. Turbide, C. Gale, S. Jeon, and G. D. Moore, Phys. Rev. C **72** (2005) 014906.

[113] S. A. Bass *et al.*, Phys. Rev. C **79** (2009) 024901.

[114] S. Jeon, J. Jalilian-Marian and I. Sarcevic, Nucl. Phys. A **715** (2003) 795; S. Jeon, J. Jalilian-Marian and I. Sarcevic, Phys. Lett. B **562** (2003) 45.

[115] D. K. Srivastava, J. Phys. G **38**, (2011) 055003.

[116] S. De and D. K. Srivastava, J. Phys. G: Nucl. Part. Phys. **39** (2012) 015001; Corrigendum:**39** (2012) 015001.

[117] P. Aurenche, M. Fontannaz, J. P. Guillet, B. A. Kniehl, E. Pilon and M. Werlen, Eur. Phys. J. C **9**, (1999) 107; P. Aurenche, M. Fontannaz, J. P. Guillet, B. A. Kniehl and M. Werlen, Eur. Phys. J. C **13**, (2000) 347.

[118] H. L. Lai *et al.*, Phys. Rev. D **55**, (1997) 1280.

[119] J. Binnewies, B. A. Kniehl and G. Kramer, Phys. Rev. D **52** (1995) 4947.

[120] A. Adare *et al.* [PHENIX Collaboration], Phys. Rev. **D76** (2007) 051106.

[121] S. Chatrchyan *et al.*[CMS Collaboration], JHEP **1108** (2011) 086.

[122] R. Baier, Y. L. Dokshitzer, A. H. Mueller, S. Peigne and D. Schiff, Nucl. Phys. B **484** (1997) 265; R. Baier, Y. L. Dokshitzer, A. H. Mueller, S. Peigne and D. Schiff, Nucl. Phys. B **483** (1997) 291.

[123] X. N. Wang, Z. Huang and I. Sarcevic, Phys. Rev. Lett. **77** (1996) 231.

[124] J. Ashman *et al.*, [EMC Collaboration], Phys. Lett. B **202** (1988) 603.

[125] D. F. Geesaman, K. Saito, A. W Thomas, Annu. Rev. Nucl. Part. Sci. (1995) **45** 337.

[126] A.H. Müeller and J. Qiu, Nucl. Phys. B **268** (1986) 427.

[127] K. J. Eskola, V. J. Kolhinen and P. V. Ruuskanen, Nucl. Phys. B **535**, (1998) 351.

[128] A. Adare *et al.* [PHENIX Collaboration], Phys. Rev. Lett. **101**, (2008) 232301.

[129] A. Adare *et al.* [PHENIX Collaboration], Phys. Rev. Lett. **101**, (2008) 162301.

[130] S. De and D. K. Srivastava, J. Phys. G **40** (2013) 075106.

[131] Y. J. Lee, J. Phys. GG **38**, (2011) 124015 [arXiv:1107.2131 [hep-ex]], [CMS Collaboration], arXiv:1202.2554 [nucl-ex].

[132] A. Adare *et al.* [PHENIX Collaboration], Phys. Rev. Lett. **105**, (2010) 142301.

[133] A. Dorbin for the ALICE Collaboration, J. Phys. G **38** (2011) 124170.

[134] J. F. Owens, Rev. Mod. Phys. **59** (1987) 465.

[135] F. Arleo, JHEP **0609**, (2006) 015; F. Arleo, K. J. Eskola, H. Paukkunen and C. A. Salgado, JHEP **1104** (2011) 055.

[136] S. S. Adler *et al.* [PHENIX Collaboration], Phys. Rev. Lett. **98** (2007) 012002.

[137] T. Isobe [PHENIX Collaboration], J. Phys. G **34** (2007) S1015 [arXiv:nucl-ex/0701040].

[138] R. J. Fries, B. Müller and D. K. Srivastava, Phys. Rev. Lett. **90** (2003) 132301; R. J. Fries, B. Müller and D. K. Srivastava, Phys. Rev. C **72** (2005) 041902 (R).

[139] B. G. Zakharov, JETP Lett. **80** (2004) 1.

[140] A. Adare *et al.* [PHENIX Collaboration], arXiv:1105.4126 [nucl-ex].

[141] A. M. Hamed, [STAR Collaboration], J. Phys. Conf. Ser. **270** (2011) 012010 [arXiv:1008.4894 [nucl-ex]].

[142] E. L. Feinberg, Nuovo Cim. A **34** (1976) 391.

[143] P. Aurenche *et al.*, Phys. Rev. D **39** (1989) 3275.

[144] T. Aaltonen *et al.* [CDF Collaboration], Phys. Rev. D **80** (2009) 111106.

[145] G. Aad *et al.* [ATLAS Collaboration], Phys. Rev. D **83** (2011) 052005.

[146] S. A. Bass, B. Muller and D. K. Srivastava, Phys. Rev. Lett. **90** (2003) 082301.

[147] D. K. Srivastava and K. Geiger, Phys. Rev. C **58** (1998) 1734.

[148] M. Wilde [ALICE Collaboration], arXiv:1210.5958 [hep-ex].

[149] R. H. Milburn, Phys. Rev. Lett. **10** (1963) 75.

[150] V. B. Berestetskii, E. M. Lifshitz and L. I. Pitaevskii, Quantum Electrodynamics, Elsevier Press.

[151] E. Braaten and R. D. Pissarski, Nucl. Phys. B **337** (1990) 569.

[152] J. Kapusta, P. Lichard, and D. Siebert, Phys. Rev. D **44** (1991) 2774.

[153] S. Turbide, C. Gale, E. Frodermann and U. Heinz, Phys. Rev. C **77** (2008) 024909.

[154] S. Turbide, C. Gale and R. J. Fries, Phys. Rev. Lett. **96** (2006) 032303.

[155] D. Lohner [ALICE Collaboration], arXiv:1212.3995[hep-ex].

[156] P. Aurenche, J. P. Guillet, E. Pilon, M. Werlen, and M. Fontannaz, Phys. Rev. D **73** (2006) 094007; S. Catani, M. Fontannaz, J. P. Guillet, and E. Pilon, JHEP **0205** (2002) 028.

[157] J. Pumplin *et al.*, JHEP **0207** (2002) 012.

[158] K. J. Eskola, H. Paukkunen, C. A. Salgado, JHEP **0904** (2009) 065.

[159] L. Bourhis, M. Fontannaz and J. P. Guillet, Eur. Phys. J. C **2**, 529 (1998).

[160] R. Rodriguez, R. J. Fries and E. Ramirez, Phys. Lett. B **693** (2010) 108.

[161] Z. Lin and M. Gyulassy, Phys. Rev. C **51** (1995) 2177.

[162] R. J. Fries, S. De, and D. K. Srivastava, Nucl. Phys. A **910–911** (2013) 482c.

[163] S. De, R. J. Fries, and D. K. Srivastava, submitted to journal.

[164] R. Reed [ALICE Collaboration], J. Phys. Conf. Ser. **446** (2013) 012006 [arXiv:1304.5945].

[165] M. Belt Tonjes [CMS Collaboration], Nucl. Phys. A **904–905** (2013) 713c.

[166] T. Renk, Phys. Rev. C **88** (2013) 034902.

[167] M. Ploskon [STAR Collaboration], Nucl. Phys. A **830** (2009) 255c [arXiv:0908.1799].

[168] R. Hagedorn, Z. Phys. C **17** (1983) 265.

List of Publications

a. Published:

In Journals:

1. Equation of state of strongly interacting matter: spectra for thermal particles and intensity correlation of thermal photons.

S. De, D. K. Srivastava and R. Chatterjee, **J. Phys. G 37**, 115004 (2010).

2. System size dependence of nuclear modification and azimuthal anisotropy of jet quenching.

S. De and D. K. Srivastava, **J. Phys. G 39**, 015001 (2012); **Corrigendum**: **J. Phys. G 40**, 049502 (2013).

3. Nuclear modification of charged hadron production at LHC.

S. De and D. K. Srivastava, **J. Phys. G 40,** 075106 (2013).

4. Predictions for p+Pb collisions at $\sqrt{s_{NN}}$ = 5 TeV*.

J. L. Albacete et al., Review paper
6.1 Direct photon cross-section, R. J. Fries and S. De

International J. of Mod. Phys. E 22, 1330007 (2013).

In conference/ symposium proceedings:

1. Equation of state of strongly interacting matter and intensity interferometry of thermal photons.
S. De, D. K. Srivastava and R. Chatterjee, **Nucl. Phys. A 862-863 (2011) 290c-293c**.

6th International Conference on Physics and Astrophysics of Quark Gluon Plasma, 6-10 December, Goa, India.

2. Centrality dependence of jet-quenching at RHIC.
S. De and D. K. Srivastava

Proceedings of the DAE Symposium on **Nucl. Phys. 56, 906-907 (2011).**

3. Jet-Tagged Back-Scattering Photons for Quark Gluon Plasma Tomography.

R. J. Fries, S. De, D. K. Srivastava, **Nucl. Phys. A 904-905 (2013) 569c-573c**.

Quark Matter 2012 International Conference, 13-18th August, Washington DC, USA.

4. Jet-Tagged Back-Scattering photons for Quark Gluon Plasma Tomography.

R. J. Fries, S. De, D. K. Srivastava, **Nucl. Phys. A 910-911 (2013) 482c-485c**.

Hard Probes 2012, 27 May- 1 June, Cagliari, Italy.

b. Accepted:

1. Extent of sensitivity of single photon production to parton distribution functions*.

S. De, **arXiv: 1305.0624**, To appear in Pramana, Journal of Physics.

2. Centrality dependence of nuclear modification factor at RHIC and LHC.

S. De and D. K. Srivastava, To appear in the proceedings of QGP meet-2012, 3-6 July, VECC, Kolkata.

c. Communicated:

1. Jet-Triggered Back-scattering Photons for Quark Gluon Plasma Tomography.
S. De, R. J. Fries, and D. K. Srivastava, **arXiv: 1402.1568**.

(*) These works are not included in the thesis.